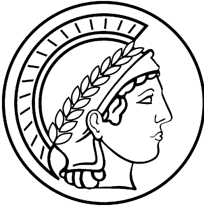

Max-Planck-Institut für Intelligente Systeme
(ehemals Max-Planck-Institut für Metallforschung)
Stuttgart

Interrelationship of interdiffusion and microstructure in thin film systems

Martin A. Noah

Dissertation
an der
Universität Stuttgart

Bericht Nr. 256
September 2016

Interrelationship of interdiffusion and microstructure in thin film systems

Von der Fakultät Chemie der Universität Stuttgart zur Erlangung der Würde eines Doktors der Naturwissenschaften (Dr. rer. nat) genehmigte Abhandlung

vorgelegt von

Martin A. Noah

aus Stuttgart

Hauptberichter:	Prof. Dr. Ir. E. J. Mittemeijer
Mitberichter:	Prof. Dr. J. Bill
Prüfungsvorsitzender:	Prof. Dr. T. Schleid

Tag der Einreichung:	01.04.2016
Tag der mündlichen Prüfung:	06.09.2016

Max-Planck-Institut für Intelligente Systeme
(ehemals Max-Planck-Institut für Metallforschung)
Institut für Materialwissenschaft der Universität Stuttgart

2016

Contents

1 Introduction **9**

1.1 Interdiffusion in thin film systems . . . 9
1.2 Focus of the thesis . . . 11
1.3 Diffusion mechanism . . . 12
1.3.1 Vacancy mechanism . . . 12
1.3.2 Divacancy mechanism . . . 13
1.3.3 Cooperative movement in amorphous solids . . . 13
1.4 Diffusion coefficients . . . 14
1.5 Continuum models for interdiffusion . . . 15
1.6 Interrelation of interdiffusion and stress . . . 16
1.7 Experimental methods . . . 17
1.7.1 Thin film deposition . . . 17
1.7.2 Microstructural characterisation . . . 19
1.7.3 Sputter-depth profiling . . . 19
1.8 Overview of the thesis . . . 24

2 Single and multiple profile fitting of AES and XPS intensity-depth profiles for analysis of interdiffusion in thin films **25**

2.1 Introduction . . . 26
2.2 Single profile fitting; original Mixing-Roughness-Information depth model . . . 26
2.3 Multiple profile fitting; intensity normalisation . . . 28
2.4 Extended MRI model . . . 30
2.4.1 Concentration dependent MRI parameters . . . 30
2.4.2 Backscatter correction . . . 32
2.4.3 Sputter-depth to sputter-time conversion . . . 33
2.4.4 Numerical calculation of diffusion profiles . . . 34
2.5 Application of the extended MRI model to interdiffusion in a-Si/pc-Ge bilayered thin films . . . 35
2.6 Conclusions . . . 38
Appendix 2.A Specimen preparation . . . 38
Appendix 2.B AES sputter-depth profiling . . . 39

3 Concentration-dependent self-diffusion coefficients in amorphous $Si_{1-x}Ge_x$ solid solutions; an interdiffusion study 41
3.1 Introduction . . . 42
3.2 Experimental procedure . . . 43
3.2.1 Specimen preparation and microstructural characterization . . . 43
3.2.2 Auger electron spectroscopy sputter-depth profiling . . . 44
3.3 Results . . . 44
3.3.1 Microstructure before and after diffusion annealing . . . 44
3.3.2 Concentration-depth profiles after diffusion annealing and determination of concentration dependent self-diffusion coefficients . . . 46
3.4 Discussion . . . 51
3.5 Conclusions . . . 54
Appendix 3.A Influence of the thermodynamic factor on the deduced self- and intrinsic diffusion coefficients and the activation enthalpy . . . 56

4 Interdiffusion in epitaxial, single-crystalline Au/Ag thin films studied by AES sputter-depth profiling and positron annihilation 59
4.1 Introduction . . . 60
4.2 Experimental procedure . . . 61
4.2.1 Specimen preparation . . . 61
4.2.2 Microstructural characterisation . . . 62
4.2.3 Auger electron spectroscopy (AES) sputter-depth profiling . . . 62
4.2.4 Positron annihilation Doppler broadening spectroscopy (DBS) . . . 63
4.3 Results and Discussion . . . 65
4.3.1 Microstructure . . . 65
4.3.2 Concentration-depth profiles . . . 67
4.3.3 Self-diffusion/impurity diffusion coefficients . . . 72
4.3.4 Comparison of the Darken-Manning and Nernst-Planck treatments . . . 77
4.3.5 Positron annihilation DBS experiments . . . 78
4.4 Conclusions . . . 81

5 Interdiffusion and stress development in single-crystalline Pd/Ag bilayers 83
5.1 Introduction . . . 84
5.2 Experimental procedure . . . 85
5.2.1 Specimen preparation . . . 85
5.2.2 Microstructural characterisation . . . 86
5.2.3 In-situ XRD stress measurements . . . 87
5.2.4 Auger electron spectroscopy (AES) sputter-depth profiling . . . 88
5.3 Results and Discussion . . . 89
5.3.1 Initial and annealed microstructure . . . 89
5.3.2 Concentration-depth profiles . . . 92
5.3.3 Chemical diffusion coefficient . . . 96
5.3.4 Fitted self-diffusion/impurity diffusion coefficients . . . 98
5.3.5 Application of the Nernst-Planck equation . . . 100
5.3.6 Stress development during interdiffusion . . . 101
5.3.7 Effect of stress on interdiffusion . . . 109
5.4 Conclusions . . . 111
Appendix 5.A Determination of the chemical diffusion coefficient 113
5.A.1 Fitting of the impurity diffusion coefficients . . . 113
5.A.2 No divacancy contribution to the diffusion mechanism of Pd in Ag . . . 115
Appendix 5.B Effect of the vacancy-wind effect . . . 116
Appendix 5.C Microstructure after prolonged diffusion annealing 117
Appendix 5.D Fitting of XRD peak evolution upon diffusion annealing . . . 119
Appendix 5.E State of planar stress in the as-prepared state . . . 122

6 Summary 123
6.1 Summary in the English language . . . 123
6.2 Zusammenfassung in deutscher Sprache . . . 127

Bibliography 133

List of Publications

Danksagung

Erklärung über die Eigenständigkeit der Dissertation

Chapter 1

Introduction

1.1 Interdiffusion in thin film systems

Thin film systems, which are widely applied in daily life applications, are often composed of layers consisting of different elements which are separated by sharp interfaces. The sharpness of the interfaces greatly influences the functional properties of the thin film system. This sharpness degrades by interdiffusion during (thermal) processing and/or during application. The degradation can be damaging to the functional properties of microelectronic devices, such as transistors [1], thin film solar cells [2] or to the read/write head of conventional hard disks employing the giant magneto resistance effect [3], but also affects structural properties as the mechanical stability of solder joints [4]. Therefore, fundamental knowledge and understanding of interdiffusion in thin film systems is crucial to predict their thermal stability and to optimize their properties.

Diffusion in thin film systems has been investigated for decades. Peculiar effects have been revealed. Often the defect concentration, especially in thin films prepared by (magnetron) sputtering, is very high resulting in a nano-crystalline thin film morphology. Interdiffusion in such highly defective thin films can be dominated entirely by fast grain boundary diffusion along these short circuit diffusion paths [5]. Effects such as diffusion induced grain boundary migration (DIGM) [6] or diffusion induced recrystallisation (DIR) [7–9] can cause considerable intermixing at relatively low temperatures [10]. Hence, in order to reduce the extent of interdiffusion in thin films a low defect density is desirable. This can be achieved by carefully adjusting the thin film preparation conditions. Interdiffusion in these often almost single-crystalline thin films is orders of magnitudes slower than in the highly defective nano-crystalline thin films [11, 12].

With a view to the above discussion, the differences in interdiffusion behaviour of thin film systems and bulk diffusion couples can be described as follows:

(i) in high-quality thin films with a small defect concentration, the distance between defects, such as dislocations or grain boundaries, can be relatively large, i.e. as compared to the diffusion length, which is smaller than the

film thickness, i.e. less than 100 nm. In bulk specimens, the diffusion length is generally larger than the distance between defects. The usual dislocation density in high quality *bulk* single crystals is $10^{-7}/\text{cm}^2$ - $10^{-8}/\text{cm}^2$ [13] resulting in an average dislocation spacing of 1 µm - 2.2 µm, whereas the usually investigated diffusion length in *bulk* specimens is several micrometres. Therefore, defects like dislocations in any case influence interdiffusion in bulk specimens, whereas no significant effect of dislocations on interdiffusion in high-quality thin films may occur.

(ii) Due to the highly non-equilibrium thin film deposition procedure, metastable phases can be formed by thin film deposition, which is usually not possible for bulk specimens. For example, semiconductors like Si or Ge form amorphous thin films upon deposition at room temperature. Despite the technological importance of these metastable amorphous systems, e.g. in thin film solar cells [14], very little is known about the diffusion mechanism and the diffusion kinetics in these covalently bonded amorphous systems. For instance, due to the absence of long range order in the amorphous phase [15–17] the diffusion mechanisms which are operative in the crystalline phase, such as the vacancy mechanism, can not operate in the amorphous state [18].

(iii) Thin films are usually deposited on a rigid substrate like silicon, which prevents the lateral expansion or contraction of the thin film. Consequently, thermal stress is induced in thin films during diffusion annealing at a temperature different from the deposition temperature, due to the generally different thermal expansions/shrinkages of the substrate and the thin film upon temperature change. In addition to the thermally induced stress due to the temperature change, the thin film can already initially be intrinsically stressed due to its preparation [19]. These thermal and growth stresses can reach values of several GPa [20, 21] and may influence (inter)diffusion [22–28].

In order to investigate the microstructural effects on interdiffusion in thin film systems, dedicated analysis techniques with a spatial resolution of the order of the diffusion lengths, which are in the nanometre range, are required. To this end, a number of techniques are available. For very small diffusion lengths, indirect methods such as X-ray [29, 30] or neutron [31, 32] diffraction are used to determine changes in the concentration-depth profile upon interdiffusion. However, with these methods the concentration dependence of the diffusion coefficients is hardly accessible. Other techniques, which are able to measure the concentration-depth profile directly, such as analytical transmission electron microscopy [33] or atom probe tomography [34] are only applicable for some material systems and are very time consuming due to the difficult specimen preparation procedure. Moreover, the preparation fo the specimens for analysis by these methods may have dramatic

effects on e.g. the local composition [35]. Sputter-depth profiling techniques are able to determine the concentration-depth profile without special specimen preparation. However, due to sputter-induced alterations the detection limit of diffusional broadening is usually of the order of several tens of nanometres [36]. Yet, by correcting for sputter-induced alterations (see section 1.7.3), the analysis of concentration-depth profiles in the nanometre range [37] gets possible and hereby microstructural effects on interdiffusion can be revealed.

1.2 Focus of the thesis

This thesis addresses the interrelationship of microstructure and interdiffusion in thin film systems. To this end, completely miscible (at least in the bulk) thin film (model) systems have been prepared, by thermal evaporation and magnetron sputtering, with carefully tailored microstructures, which have been characterised by atomic force microscopy (AFM), X-ray diffraction (XRD) and (high resolution) transmission electron microscopy ((HR)TEM).

Interdiffusion in the thin films has been investigated by Auger electron spectroscopy (AES) and X-ray photo electron spectroscopy (XPS) sputter-depth profiling. To this end the Mixing-Roughness-Information depth (MRI) model, which allows the correction of sputter-induced alterations, has been extended to increase the reliability of the determination of the genuine, true concentration-depth profile from measured sputter-depth profiles. With this procedure, very small diffusion lengths in the nanometre range can be determined and the concentration dependence of the chemical, as well as intrinsic and self-diffusion coefficient(s) can be accounted for directly (see Chapter 2). Employing this procedure, different aspects of interdiffusion in thin films could be investigated at low annealing temperatures. Firstly, due to the high sensitivity of the applied sputter-depth profiling technique, the small diffusion lengths in metastable amorphous $Si_{1-x}Ge_x$ solid solutions could be measured and thereby the concentration dependent self-diffusion coefficients of Si and Ge could be determined and analysed (see Chapter 3). Secondly, the effect of vacancy sources and sinks on interdiffusion has been investigated in epitaxial single-crystalline Au/Ag thin films (see Chapter 4). To this end, a combinatorial approach using AES sputter-depth profiling, to resolve the chemical concentration-depth profile, and positron annihilation Doppler broadening spectroscopy, to resolve the defect concentration-depth profile, was applied. Thirdly, the interplay of stress and interdiffusion has been investigated in single-crystalline Pd/Ag thin films by XRD stress measurements (see Chapter 5).

1.3 Diffusion mechanism

1.3.1 Vacancy mechanism

Substitutional volume diffusion in crystalline metallic systems, as well as crystalline semiconductors at low temperatures, is mediated by vacancies (see figure 1.1a). The concentration of these equilibrium point defects depends on the homologous temperature, T/T_m (T is the absolute temperature and T_m is the melting temperature), of the material [38, 39]. Close to the melting point the equilibrium vacancy concentration can reach a site fraction of 10^{-4}-10^{-3} [40]. The temperature dependence of the equilibrium vacancy concentration strongly influences the temperature dependence of the self-diffusion coefficient, D^*, according to [41]

$$D^* = \frac{1}{6}\nu z a^2 f \exp\left(\frac{\Delta S_f + \Delta S_m}{k}\right) \exp\left(-\frac{\Delta H_f + \Delta H_m}{kT}\right), \qquad (1.1)$$

where ν is the Debye frequency, z is the coordination number, a is the jump distance, f is the crystal structure specific correlation factor, ΔS_f is the vacancy formation entropy, ΔS_m is the vacancy migration entropy, ΔH_f is the vacancy formation enthalpy, ΔH_m is the vacancy migration enthalpy and k is the Boltzmann constant.

Due to the generally different melting temperatures of the elements (and consequently different homologous temperatures during diffusion annealing), the equilibrium vacancy concentrations in the two sublayers are generally different during diffusion annealing and consequently, the mobilities of the atoms in the two sublayers are different: generally, diffusion is faster in the sublayer composed of the element with the lower melting temperature [42]. Due to the different mobilities of the atoms in the two sublayers, the mass fluxes of the two components generally generate a net flux of vacancies toward the sublayer composed of mainly the faster diffusing component in a diffusion couple. Consequently, the vacancy concentration increases in the sublayer composed of mainly the faster diffusing component and decreases in the sublayer composed of mainly the slower diffusing component, if no mechanisms for vacancy creation and annihilation are operative. Climbing dislocations can serve as vacancy sources and sinks and can maintain the equilibrium vacancy concentration during interdiffusion [43]. If the dislocation line vector of the climbing edge dislocation is inclined with respect to the diffusion flux, a shift of the initial interface in the laboratory frame of reference occurs (Kirkendall shift). A description of this phenomenon has been given by Darken and Smigelskas [44] resulting in the well known Darken equation [45] (see section 1.5). According to this treatment the equilibrium

vacancy concentration-depth profile is maintained during the entire interdiffusion process by vacancy creation and annihilation. If the number of active vacancy sources and sinks is too small and consequently the distance between them is larger than the diffusion length, the vacancy flux can not be compensated by the available vacancy sources and sinks and a non-equilibrium vacancy concentration-depth profile develops. If no vacancy sources and sinks are active at all, the chemical diffusion coefficient can be described by the Nernst-Planck/Nazarov-Gurov equation [46–50] (see section 1.5). At large vacancy supersaturation pore formation by vacancy condensation is observed [51] which is in most applications harmful for e.g. the mechanical properties [4].

1.3.2 Divacancy mechanism

Generally a binding enthalpy exists between vacancies, due to reduced number of nearest neighbours per vacancy of vacancy clusters as compared to isolated monovacancies [52]. These vacancy clusters have a smaller activation enthalpy for migration, which accelerates diffusion [40]. A measurable effect of divacancies on diffusion can usually only be observed at annealing temperatures close to the melting point, since the number of divacancies is very small at lower temperatures. The amount of vacancy clusters consisting of more than two vacancies is usually negligible small and can be neglected [40]. As a result of the contribution of divacancies to the diffusion mechanism at higher annealing temperatures, the Arrhenius plots show an upward curvature, which is modelled by the sum of two exponential functions according to [40, 53]

$$D = D_{0,1V} \cdot \exp\left(-\frac{Q_{1V}}{kT}\right) + D_{0,2V} \cdot \exp\left(-\frac{Q_{2V}}{kT}\right), \qquad (1.2)$$

where $D_{0,1V}$, $D_{0,2V}$, Q_{1V} and Q_{2V} are the temperature independent pre-exponential factors and temperature independent activation enthalpies of the monovacancy (1V) and divacancy (2V) contribution, respectively.

1.3.3 Cooperative movement in amorphous solids

In amorphous solids, i.e. metallic glasses or amorphous semiconductors, no equilibrium point defects such as vacancies are present (but excess free volume is present). Therefore, diffusion can not occur according the vacancy mechanism. Monte Carlo simulations suggest that in metallic glasses a long range cooperative movement of atoms can occur which involves about ten atoms in one diffusion event [54–56] (see figure 1.1b); a similar mechanism

has been proposed for interphase boundary movement and grain boundary diffusion in crystalline materials [57]. The effect of possible covalent bonds between the atoms in an amorphous semiconductor solid, e.g. in amorphous $Si_{1-x}Ge_x$ solid solutions, on the diffusion mechanism is discussed in chapter 3.

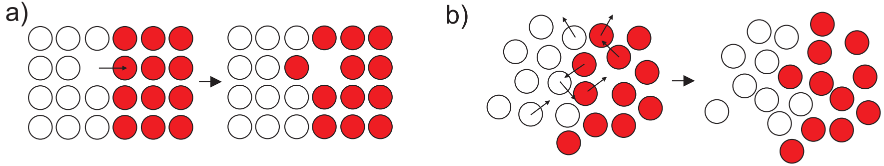

Figure 1.1: Schematic illustration of a) the vacancy mechanism and b) the cooperative movement of atoms in an amorphous material.

1.4 Diffusion coefficients

The (inter)diffusion kinetics is fully described with a (temperature and concentration dependent) (chemical) diffusion coefficient. However, there are several different diffusion coefficients, which describe different diffusion phenomena. In the following the different diffusion coefficients are defined. The connection among these diffusion coefficients is given in section 1.5.

Tracer diffusion coefficient $D^*_{A^*,AB}$ Tracer diffusion coefficients describe diffusion of a tracer atom, often a radioactive isotope, A^*, in an homogeneous alloy, $A_{1-x}B_x$, or a pure component, A or B. The concentration of tracer atoms is thereby very small and does not change the composition of the matrix. Therefore, mass transport occurs exclusively due to the statistical jumps of atoms in the absence of any chemical potential gradient.

Self-diffusion coefficient $D^*_{A,AB}$ The term self-diffusion coefficient is equivalent to the term tracer diffusion coefficient if the isotope effect (mass dependence of the atomic jump frequency) [58] is neglected. The self-diffusion coefficient does not only describe self-diffusion of A in pure A, but also the diffusion of A in $A_{1-x}B_x$ solid solutions in the absence of a concentration gradient (tracer diffusion). As a consequence, the self-diffusion coefficient is generally dependent on concentration. In many systems this concentration dependence follows an exponential function, which results directly from a linear concentration dependence of the activation enthalpy for diffusion.

Impurity diffusion coefficient $D^*_{A,B}$ The impurity diffusion coefficient describes diffusion of a very small amount of impurity atoms, A, in an otherwise pure component, B, in the absence of any chemical potential gradient. Therefore, the impurity diffusion coefficient is also a self-diffusion coefficient (of A) in the pure component B.

Intrinsic diffusion coefficient $D_{A,AB}$ The intrinsic diffusion coefficient describes diffusion of one component in a chemical potential gradient. It is composed of the self-diffusion coefficient and the thermodynamic factor.

Interdiffusion coefficient $\widetilde{D}_{AB}$ The interdiffusion coefficient describes intermixing in a chemical potential gradient. It is generally strongly concentration dependent and depends on the presence of vacancy sources and sinks (see section 1.5).

1.5 Continuum models for interdiffusion

The change of the concentration-depth profile upon diffusion annealing can be described by Fick's second law [41]

$$\frac{\partial c}{\partial t} = \frac{\partial}{\partial z}\left(\widetilde{D}\frac{\partial c}{\partial z}\right), \tag{1.3}$$

where c is the concentration, z is the depth, t the time and $\widetilde{D}$ is the chemical diffusion coefficient. Generally the chemical diffusion coefficient depends on concentration, temperature and pressure, resulting in an asymmetric concentration-depth profile upon diffusion annealing at constant temperature and pressure.

In a system with sufficient vacancy sources and sinks any vacancy flow due to different atomic mobilities can be compensated and the vacancy concentration-depth profile remains at the equilibrium vacancy concentration. The chemical diffusion coefficient is then dominated by the faster component and can be linked to the intrinsic diffusion coefficients by the Darken-Manning equation [45, 50, 59]

$$\widetilde{D} = (x_A D_B + x_B D_A,) \cdot S_{\text{wind}} \tag{1.4}$$

where D_A and D_B are the intrinsic diffusion coefficients of component A and B and S_{wind} is the vacancy wind factor, respectively. The vacancy-wind factor, S_{wind}, which describes correlation effects in a random alloy arising

by a net flux of vacancies, can be approximated according to [50, 59]

$$S_{\text{wind}} = 1 + \frac{1-f}{f} \cdot \frac{x_{\text{A}} x_{\text{B}} (D^*_{\text{A}} - D^*_{\text{B}})^2}{(x_{\text{A}} D^*_{\text{A}} + x_{\text{B}} D^*_{\text{B}}) \cdot (x_{\text{A}} D^*_{\text{B}} + x_{\text{B}} D^*_{\text{A}})}, \tag{1.5}$$

where f is the geometric correlation factor for the crystal-lattice (i.e. 0.7815 for the fcc crystal structure). The effect of the vacancy-wind effect on the chemical diffusion coefficient is usually small ($S \leq 1/f$, i.e. $S \leq 1.28$ for the fcc crystal structure), and is often neglected.

In a system with no vacancy sources and sinks at all, any vacancy flow due to different atomic mobilities leads to the establishment of a non-equilibrium vacancy concentration-depth profile upon interdiffusion. As a consequence, the chemical diffusion coefficient is then dominated by the slower component and is described according to the Nernst-Planck/Nazarov-Gurov equation [46–50]

$$\widetilde{D} = \frac{D_A D_B}{x_A D_A + x_B D_B}. \tag{1.6}$$

The intrinsic diffusion coefficients are composed of the self-diffusion coefficient, D^*_A, and the thermodynamic factor, Φ, according to

$$D_A = D^*_A \cdot \Phi. \tag{1.7}$$

Thermodynamic data is available for many systems and the thermodynamic factor can straightforwardly be calculated from this data. Then the intrinsic and the chemical diffusion coefficient are known over the whole concentration range, if the concentration dependent self-diffusion coefficients are known.

1.6 Interrelation of interdiffusion and stress

It is well known, that the interdiffusion coefficient depends on pressure. This pressure dependence is usually described according to [50]

$$\left(\frac{\partial \ln D}{\partial p}\right)_T = -\frac{\Delta V}{kT}, \tag{1.8}$$

where p is the hydrostatic pressure and ΔV is the activation volume. For diffusion according the vacancy mechanism, the diffusion coefficient generally decreases with increasing pressure.

In thin film systems the state of stress due to thermal or growth stresses is generally not of hydrostatic nature. The free surface of the thin film system allows stress relaxation in the direction parallel to the specimen surface

normal and often a biaxial state of stress is established. Consequently, the treatment according to Eq. 1.8 is not applicable in such cases. Larché and Cahn developed a theory to describe the interrelation of interdiffusion and stress in a non hydrostatic state of stress [60–62]. The model accounts for the effect of stress on the diffusion potential (which replaces the chemical potential) and thus on interdiffusion as well as the effect of compositional changes on the stress-depth profile due to interdiffusion. A compositional stress is induced by interdiffusion if the molar volumes of the interdiffusing atoms are different, or if their atomic flux across the initial interface is different. For example, due to a difference in the molar volumes of the components a compressive compositional stress can be induced in the sublayer composed of the component with the smaller molar volume and a tensile compositional stress can be induced in the sublayer composed of the component with the larger molar volume upon interdiffusion (see chapter 5).

The experimental verification of this model is difficult [22–26] since it is based on a so-called network solid concept, in which the number of lattice sites is conserved. This requirement is hardly fulfilled in real material systems. The molar volumes of the interdiffusing components are generally different. Therefore, often a semi-coherent interface with misfit dislocations at the interface between the components develops. These misfit dislocations can serve as vacancy sources and sinks and consequently the number of lattice sites might not be conserved upon interdiffusion. Furthermore, other defects like grain boundaries can change the number of lattice sites upon diffusion annealing e.g. by grain growth.

1.7 Experimental methods

1.7.1 Thin film deposition

In this study physical vapour deposition, namely thermal evaporation and magnetron sputtering, has been applied for thin film deposition. The microstructure of deposited thin films strongly depends on the deposition conditions such as deposition rate, substrate temperature, residual gas atmosphere and the substrate surface [63]. Since the parameters which determine the thin film growth, such as surface diffusivities [64] and surface and interface energies, strongly depend on the chosen material/substrate combination, the deposition parameters have to be carefully adjusted for each system. To this end, a customised ultra high vacuum (UHV) system equipped with effusion cells for thermal evaporation, a laser heater for specimen cleaning and analysis methods, such as scanning tunnelling microscopy (STM) and XPS have been used [65]. By dedicated investigations of the development of the sur-

face morphology upon thin film deposition, the deposition conditions could be adjusted to tailor the microstructure of the deposited thin films. This allowed the preparation of completely amorphous as well as single-crystalline specimens.

Amorphous Si/Ge Deposition of semiconductors such as Si and Ge at room temperature or below, results in an amorphous thin film, due to the low atomic mobility of the atoms at these temperatures [66]. Only at substrate temperatures larger than 400 °C, the atomic mobility of Si or Ge is large enough to from a crystalline film [67].

Due to the covalent bonds between Si and Ge atoms the mainly fourfold coordination, which is present in the crystalline phase, is largely maintained in the amorphous phase. However, the bond angles and bond lengths are distorted [16]. As a consequence, the density of the amorphous phase is smaller than the crystalline phase [68, 69]. The special microstructure of the thermodynamically metastable amorphous phase has interesting effects on the diffusion processes occurring in these materials (see chapter 3).

Epitaxial Au/Ag / Pd/Ag Face centred cubic metallic thin films, such as Ag, Au, Pd or Al, exhibit often a strong (1 1 1) fibre texture, which is attributed to the low surface energy of the (1 1 1) facet [70]. Due to the in-plane rotation of the grains in a fibre textured specimen, many grain boundaries, which can serve as fast diffusion paths, are present in these thin films. In order to reveal microstructural as well as stress effects on interdiffusion, the thin film deposition parameters have been carefully adjusted in this study in order to obtain single-crystalline Ag(0 0 1) layers. The large linear lattice misfit between Ag and Si (24.7 %) is thereby accommodated by domain epitaxy (linear domain misfit of 0.3 %) [71], where the Ag and Si lattice coincidence every four and three unit cells, respectively. Due to the negligible mutual solubility of Ag and Si [72], no significant interdiffusion occurs at the Ag/Si interface during diffusion annealing, which makes the Ag/Si system an ideal thin film/substrate model system for interdiffusion studies of Me/Ag systems when Me is deposited on top of Ag.

The single-crystalline Ag(0 0 1) layers served as seed layers for subsequent deposition of single-crystalline Au and Pd layers with a cube-on-cube orientation relationship to the Ag layer and the Si substrate. Due to the negligible small linear lattice misfit of Ag and Au (0.18 %) [73], theoretically no misfit dislocations are present at the Au/Ag interface, whereas on average one misfit dislocation is present every 8.5 nm along the Pd/Ag interface due to the considerable lattice misfit between Ag and Pd (4.8 %) [73]. The presence

of misfit dislocations at the bilayer interface has direct consequences on the interdiffusion behaviour due to the absence or presence of vacancy sources and sinks (see chapter 4 and chapter 5, respectively).

1.7.2 Microstructural characterisation

The microstructure of the deposited thin films has been investigated by several techniques. The surface roughness of single layers and bilayers has been determined by AFM. The surface roughness of the specimen plays an important role for the determination of the concentration-depth profile by sputter-depth profiling. A small surface roughness (i.e. root mean squared roughness < 5 nm) is mandatory to resolve very small diffusion lengths in the nanometre range by sputter-depth profiling (see section 1.7.3).

XRD and cross-sectional (HR)TEM have been applied to obtain structural information from the prepared thin films. While XRD provides averaged information over a larger mesoscopic specimen volume, local information on the atomic scale, like the arrangements of the atoms at the interface or layer thicknesses can be accessed by (HR)TEM.

The concentration of vacancies plays a crucial role for interdiffusion (see section 1.3). In order to determine the change of the vacancy concentration-depth profile upon diffusion annealing positron annihilation Doppler broadening spectroscopy (DBS) has been applied. Conventional laboratory positron sources which are based on β^+ active isotopes do provide only very small positron fluxes and consequently long measurement times are necessary. With the worlds largest flux of positrons at the positron source NEPOMUC in Garching [74] short measurement times can be realised, which allows the determination of the defect concentration *in-situ* during diffusion annealing. Furthermore, by changing the acceleration voltage of the positrons, their kinetic energy can be adjusted, which allows depth-dependent measurements. This technique has been applied in this study (see chapter 4).

1.7.3 Sputter-depth profiling

General procedure

In order to access concentration-depth profiles of thin films, sputter-depth profiling can be applied [75]. For this destructive analysis technique the chemical composition of the specimen surface is measured by a surface sensitive technique, such as XPS, AES or secondary ion mass spectroscopy (SIMS). By successive removal of the specimen surface layer(s) by the bombardment of the specimen surface with ions, such as Ar^+, Cs^+ or O_2^+, (see figure 1.2a) and measurement of the specimen surface concentration, a concentration-depth profile is obtained.

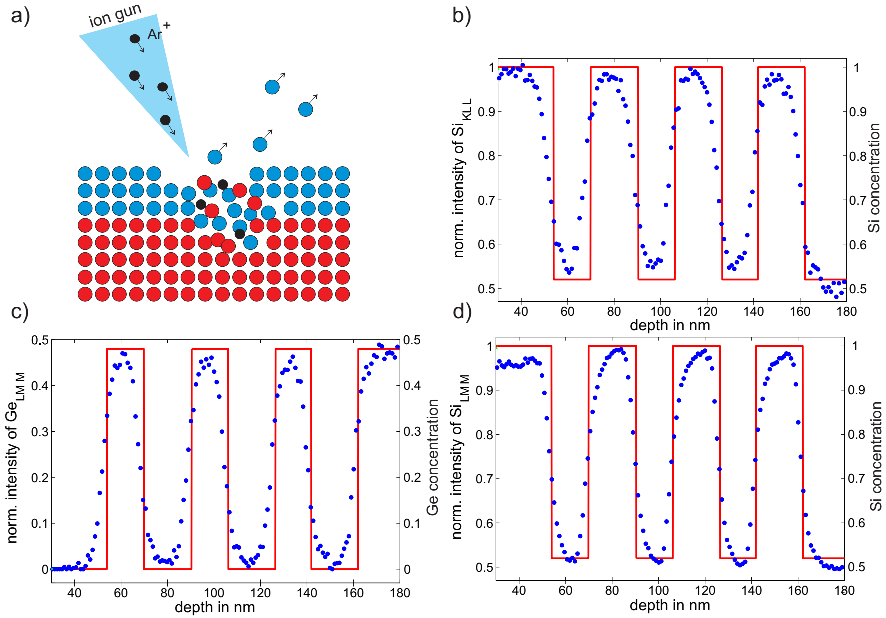

Figure 1.2: a) Schematic illustration of sputter-depth profiling. The surface atoms of the specimen are removed by the bombardment of the specimen surface with Ar^{+}-ions. Due to collision cascades, mixing of the atoms in deeper layers underneath the specimen surface occurs, which alters the genuine concentration-depth profile. b)-d) Measured AES intensity-depth profile of an amorphous $Si/Si_{0.52}Ge_{0.48}$ multilayer (dots) with presumed sharp interfaces (solid line). Due to sputter induced alterations, the sharp interfaces are broadened. Note the different extent of broadening of the two Si intensity-depth profiles (b and d). Due to the smaller kinetic energy of Auger electrons from the Si_{LMM} transition, as compared to the high kinetic energy of Auger electrons from the Si_{KLL} transition, and the resulting smaller information depth of Auger electrons from the Si_{LMM} transition, the broadening of the intensity-depth profile of the Si_{LMM} transition is less pronounced.

The surface analytic technique for sputter-depth profiling has to be chosen with care. For classic interdiffusion studies in bilayered specimens with large concentration differences, e.g. interdiffusion in a bilayer composed of pure A and pure B, AES and XPS are the preferred techniques, since the conversion of the measured intensity to concentration can be highly nonlinear at high concentrations in SIMS due to pronounced matrix effects [76, 77]. SIMS is the preferred choice to study e.g. dopant diffusion in semiconductors [78] due to the high sensitivity of the technique and the high dynamic range.

In this study AES and XPS sputter-depth profiling using Ar^+-ions with a kinetic energy of 1 keV is employed to determine concentration-depth profiles.

Mixing-Roughness-Information depth (MRI) model

During sputter-depth profiling, the specimen is bombarded with ions in order to successively remove the surface layer(s). The kinetic energy of the ions is thereby transferred to the specimen, which results in the removal of surface atoms and also to atomic displacements in deeper layers of the specimen by cascade mixing [79] (see figure 1.2a). This ion-bombardment induced atomic mixing is only one of the sputter induced alterations occurring during sputter-depth profiling. The intrinsic specimen surface and interface roughness as well as the information depth of the Auger electrons or photoelectrons contribute to an additional broadening of the genuine concentration-depth profile upon sputter-depth profiling [75]. As a consequence, the depth resolution of the technique is reduced and features of the genuine concentration-depth profile are masked by these sputter-induced alterations (see figures 1.2b-d).

In order to increase the depth resolution of the sputter-depth profiling technique the Mixing-Roughness-Information depth model [80–89] has been developed. The model aims at describing the sputter induced alterations by physical meaningful parameters, which can be accessed by experiment and/or calculations. In the basic MRI model [80–89], the measured normalised intensity, I/I_0, is given by the convolution of the genuine concentration-depth profile, $X(z)$, and the depth resolution function, g, which describes the sputter induced alterations

$$\frac{I(z)}{I_0} = \int_{-\infty}^{+\infty} X(z') \cdot g(z - z')dz', \tag{1.9}$$

where z is the depth below the specimen surface. The depth resolution

function itself can be approximated by the convolution[1] of the individual contributions describing atomic mixing, surface and interface roughness and information depth. The basic MRI model and its extension performed in this work are described in detail in Chapter 2.

Usually the signal to noise ratio is too low to allow a straightforward deconvolution of equation 1.9 to determine the genuine concentration-depth profile from a measured sputter-depth profile [85, 88]. Therefore, a forward calculation approach is applied. An initial guess of the genuine concentration-depth profile is convoluted with the predetermined depth-resolution function and the result is compared with the measured intensity-depth profile. If the deviation of the calculated intensity-depth profile from the experimentally measured intensity-depth profile is too large, the genuine concentration-depth profile is changed and the comparison of the calculated intensity-depth profile, calculated by the convolution of the changed genuine concentration-depth profile with the depth-resolution function, with the measured intensity-detph profile is repeated until a good agreement between the calculated and the measured intensity-depth profile is obtained (see figure 1.3).

Owing to the forward calculation procedure, there is no unique solution to describe the measured sputter-depth profile. Therefore, a physically reasonable model to describe the genuine concentration-depth profile upon diffusion annealing is mandatory to deduce the genuine concentration-depth profile according the outlined model. In this work, the numerical solution of Fick's second law with a concentration dependent chemical diffusion coefficient has been used (see section 1.5).

[1] Note that a convolution of the individual contributions to the depth-resolution function is not applicable, if the MRI parameters depend on concentration (see Chapter 2).

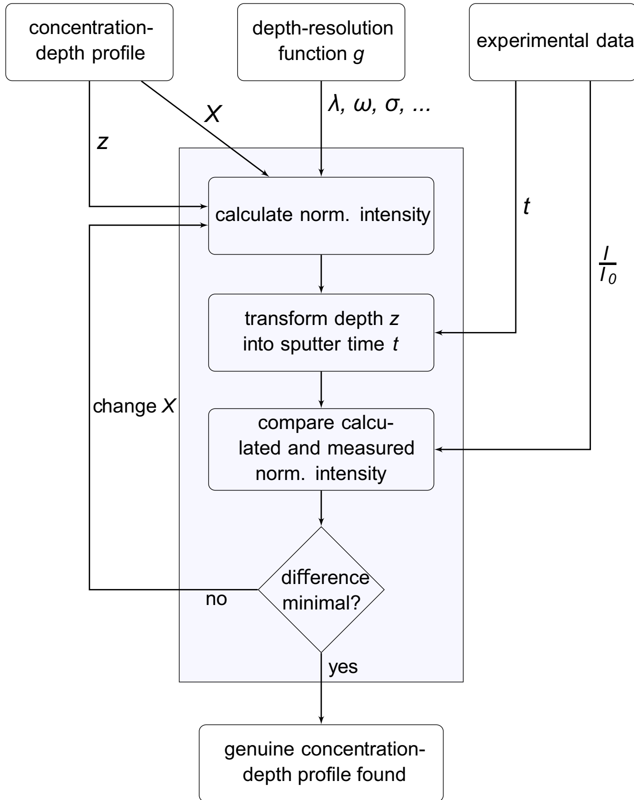

Figure 1.3: Flowchart of the basic MRI model, explaining the forward calculation approach [65]. An initial guess of the genuine concentration-depth profile, X, is convoluted with the predetermined depth-resolution function, g, in order to obtain the calculated normalised intensity in dependence of the depth, z. After transforming the depth into the experimentally measured sputter time, t, the calculated normalised intensity is compared to the measured normalised intensity. The genuine concentration-depth profile is then changed until the difference between the calculated normalised intensity and the measured normalised intensity is minimal.

1.8 Overview of the thesis

In **chapter 2** the Mixing-Roughness-Information depth (MRI) model is extended for the investigation of interdiffusion in thin film systems. To this end, concentration-dependent model parameters are introduced, the effect of concentration gradients on the backscatter correction is investigated and a *multiple-profile* fitting procedure is introduced, which uses more experimental data as the usually applied single-profile fitting, i.e. various intensity-depth profiles are fitted simultaneously. The multiple-profile fitting procedure increases the reliability of deduced model parameters and allows the determination of self-diffusion coefficients in the nanometre range. This extended model is applied to several thin film systems in order to investigate the interrelationship among interdiffusion, microstructure and stress.

In **chapter 3** concentration dependent self-diffusion coefficients of Si and Ge in amorphous $Si_{1-x}Ge_x$ solid solutions are determined. Due to the high sensitivity of the extended MRI model, the annealing conditions could be tailored to avoid crystallisation of the metastable amorphous phase and conclusions on the diffusion mechanism, operating in covalently bond materials without long range order, could be obtained.

In **chapter 4** the influence of vacancy sources and sinks on interdiffusion in single-crystalline Au/Ag bilayered thin films is investigated. To this end, the chemical composition has been determined by AES sputter-depth profiling (and quantified by the extended MRI model) and the defect concentration-depth profile has been determined by *in-situ* positron annihilation Doppler broadening spectroscopy at the positron source NEPOMUC in Garching.

The last part, **chapter 5**, deals with the interplay of stress and interdiffusion in single-crystalline Pd/Ag thin films. To this end, the stress evolution during thermal cycling and isothermal annealing has been determined from *in-situ* stress measurements by XRD.

Chapter 2

Single and multiple profile fitting of AES and XPS intensity-depth profiles for analysis of interdiffusion in thin films

Martin A. Noah[1], David Flötotto[1], Zumin Wang[1], and Eric J. Mittemeijer[1,2]

[1] *Max Planck Institute for Intelligent Systems (formerly Max Planck Institute for Metals Research), Heisenbergstr. 3, D-70569 Stuttgart, Germany*
[2] *Institute for Materials Science, University of Stuttgart, Heisenbergstr. 3, D-70569 Stuttgart, Germany*

Abstract

Simultaneous fitting of independently measured sputter-depth profiles of intensities of Auger electrons or photoelectrons from different Auger transitions (AES) or core levels (XPS) is shown to increase the reliability of the thus determined concentration-depth profiles in diffusion-annealed thin film systems, as compared to the usually applied single profile fitting. In this context an extension of the Mixing-Roughness-Information depth (MRI) model is presented, which includes the concentration dependence of the MRI parameters for mixing and information depth, as well as of the backscattering correction factor and the sputter rate. The thus proposed procedure is applicable for diffusion lengths as small as a few nanometre and was applied to determine the concentration dependent self-diffusion coefficients from measured AES and XPS sputter-depth profiles recorded from diffusion-annealed amorphous Si/polycrystalline Ge bilayers.

2.1 Introduction

Thin film systems are essential components of many advanced devices such as transistors, lasers or solar cells. The functional properties of these thin film systems strongly depend on the sharpness of the sublayer interface(s) [90]. Therefore, fundamental knowledge of interdiffusion in thin film systems is crucial to predict their thermal stability and to improve their properties.

Sputter-depth profiling in combination with surface sensitive and element sensitive techniques (such as AES and XPS) is widely applied for interdiffusion studies to deduce the concentration-depth profiles upon annealing and thereby to determine diffusion data [37]. However, the sputter removal of atomic layers at the surface alters the concentration-depth profile in the remaining specimen by ion-bombardment-induced alterations ("atomic mixing" and "roughening"). Therefore, the direct determination of diffusion data from the measured intensity-depth profiles is impeded. Consequently, the evaluation is often of only qualitative nature [91] and/or considers only a small part (such as the region close at the interface or focuses on a developing concentration plateau away from the interface) of the measured intensity-depth profile [5]. The Mixing-Roughness-Information depth (MRI) model [81, 84, 85] was developed to account for such sputter-induced alterations and thereby to incorporate the whole measured intensity-depth profile in the evaluation. However, many simplifications applied in the original MRI model limit the reliability of the obtained results.

In the present work, distinct improvement in the analysis of diffusion in thin film systems has been realised by multiple (instead of single) profile fitting of sputter-depth profiles and by accounting for the concentration dependence of the MRI parameters, of the sputter rate and of the backscattering correction factors. The significant impact of these improvements on the determination of diffusion data is demonstrated, in particular, for diffusion-annealed amorphous Si/polycrystalline Ge bilayered thin films. Thus, concentration-dependent self-diffusion coefficients can be determined for thin-film systems with diffusion lengths as small as a few nanometres.

2.2 Single profile fitting; original Mixing-Roughness-Information depth model

According to the MRI model [81, 84, 85] the experimentally induced broadening of the measured sputter-depth profile is modelled by a depth-resolution function, g, to account for sputter-induced alterations: The effects of surface and interface roughness, the influence of the effective attenuation length of

the Auger electrons or the photoelectrons, and the influences of preferential sputtering and backscattering. The measured normalised intensity-depth profile, I/I^0, (after sputter-time to sputter-depth conversion) is then given by the convolution of the genuine (i.e not affected by the sputter-depth profiling) concentration-depth profile, X, with the depth-resolution function, g,

$$I^{\mathrm{norm}} = \frac{I(z)}{I^0} = \int_{-\infty}^{+\infty} X(z') \cdot g(z-z')dz', \tag{2.1}$$

where z is the actual sputter depth and z' denotes a running depth parameter. The depth-resolution function, g, comprises the interplay of sputter-induced mixing and information depth, as well as their convolution with the roughness of the surface and interface [85]

$$g = \left(\left[1 - \exp\left(-\frac{w}{\lambda \cdot \cos\phi}\right)\right] \cdot g_w + g_\lambda\right) * g_\sigma, \tag{2.2}$$

where w is the MRI parameter for mixing, λ is the effective attenuation length (EAL) of Auger electrons or photoelectrons, as tabulated in the NIST database [92], and ϕ is the detection angle of the electrons with respect to the specimen-surface normal. Note that the often applied convolution of all three contributions to the depth resolution function g (i.e. $g_\lambda * g_w * g_\sigma$) is only valid if the information depth is smaller than the mixing length [85].

The smearing contributions, g_w, g_σ and g_λ can be taken as follows. The contribution of sputter-induced mixing, g_w, can be described according to a simple approach from Liau et al. [93](adopting a constant concentration in the mixed region). The contribution of roughness, g_σ, can be described by a Gaussian function [81]. The contribution of the information depth, g_λ, is controlled by the attenuation lengths of the electrons. Thus,

$$g_w = \frac{1}{w}\exp\left(-\frac{z-z'+w}{w}\right) \qquad z' < z+w, \text{else } g_w = 0 \tag{2.3}$$

$$g_\sigma = \frac{1}{\sigma\sqrt{2\pi}}\exp\left(-\frac{(z-z')^2}{2\sigma^2}\right) \tag{2.4}$$

$$g_\lambda = \frac{1}{\lambda \cdot \cos\phi}\exp\left(\frac{z-z'}{\lambda \cdot \cos\phi}\right) \qquad z' > z+w, \text{else } g_\lambda = 0 \tag{2.5}$$

where σ is the MRI parameter for roughness. Note that the above illustrated approach is only valid for concentration independent MRI parameters, w and σ, and EAL (see section 2.4.1).

The signal to noise ratio of the experimental data is usually too small to

allow a straightforward deconvolution of Eqn 2.1 [85, 88]. Hence a so-called forward calculation approach is used to resolve the genuine concentration-depth profile (e.g. after diffusion annealing):
Step (i): Firstly, the MRI parameters σ and w of the depth-resolution function have to be determined from a reference measurement, i.e. by iteratively minimising the difference of the experimentally obtained normalised intensity-sputter time profile and the calculated normalised intensity-sputter time profile as obtained by the convolution of the (in this case known) genuine concentration-depth profile (i.e. from an as-prepared specimen with a sharp interface) with the depth-resolution function, while varying σ and w. The projected depth range in the specimen of the ions bombarding the specimen upon sputtering, as determined by SRIM Monte Carlo simulations [94], is thereby used as an initial assumption for the mixing parameter, w.
Step (ii): Secondly, the genuine concentration-depth profile (as established after diffusion annealing) can be deduced by iteratively minimising the difference of the measured normalised intensity-sputter time profile and the calculated normalised intensity-sputter time profile as obtained by the convolution of the assumed genuine concentration-depth profile with the known (predetermined) depth-resolution function, while varying the assumed genuine concentration-depth profile.

Note: The calculated normalised intensity-depth profile (convolution of genuine concentration-depth profile with the depth-resolution function according Eqn 2.1) is transformed into a normalised intensity-sputter time profile for the comparison with the measured normalised intensity-sputter time profile by applying predetermined (on an as-prepared specimen) elemental sputter rates.

2.3 Multiple profile fitting; intensity normalisation

For a bilayered thin film system, with i (interdiffusing) elements, the intensity of Auger electrons or photoelectrons from an element specific Auger transition or core level can be measured during sputter-depth profiling for each element (note: sometimes even several (i.e. high and low energetic) Auger transitions or core levels of the same element are accessible). Often, the peak-to-peak height of the measured differentiated AES spectra or the measured (integrated) intensity of XPS core level spectra is normalised considering the respective elemental sensitivity factors [37, 95] according to

$$I_i^{\mathrm{norm}} = \frac{\frac{I_i}{S_i}}{\sum\limits_j \frac{I_j}{S_j}}, \tag{2.6}$$

where I_i is the measured AES peak to peak height or the (integrated) intensity of the XPS core level spectrum and S_i represents the elemental sensitivity factor for the transition considered of the ith element (which is equal to I_i of a *pure* specimen of element i, measured under the same conditions). This normalisation procedure is applicable only, if the information depths ($\approx$ 3 $\times$ EAL) of the measured Auger electrons or photoelectrons and the backscattering correction factors (only for AES) of the elements concerned are similar. However, if the information depths and the backscattering correction factors of the elements concerned are different, the normalisation procedure according to Eqn 2.6 becomes problematic for inhomogeneous specimens because measured intensities from different (information-) depths (i.e. from depth ranges of different (average) composition) are compared with each other. To allow correction for such effects, a different normalisation procedure is adopted: The measured intensity of the ith element, I_i, is normalised by only S_i (cf. Eqn 2.6)

$$I_i^{\mathrm{norm}} = \frac{I_i}{S_i}. \tag{2.7}$$

The normalisation procedure according to Eqn 2.7 implies that the I_i^{norm}-sputter time profiles for the different transitions of the different elements are independent, whereas this does not hold for the I_i^{norm}-sputter time profiles obtained after normalisation of I_i according Eqn 2.6. As a consequence, all measured intensity-sputter time profiles (after normalisation according to Eqn 2.7) can be used in a *simultaneous* multiple profile fitting procedure. During such a multiple profile fitting procedure, all measured I_i^{norm}-sputter time profiles can be fitted, simultaneously, with the same MRI parameters for roughness and mixing (under the assumption of a constant concentration in the ion-bombardment-induced mixed region), and with the same genuine concentration-depth profile. The different EALs of Auger electrons and/or photoelectrons of the different Auger transitions and/or XPS core level spectra are taken from literature data [92]. During the multiple profile fitting procedure, the sum of the differences of each calculated normalised intensity-depth profile and its corresponing experimentally measured normalised intensity-depth profile is minimized.

The considerably increased amount of independent experimental data in the multiple profile fitting procedure, as compared to the common single profile fitting procedure, increases the reliability of the MRI parameters determined for roughness and mixing (in step (i); see section 2.2) and subsequently (in step (ii); see section 2.2) increases the reliability of the determined genuine concentration-depth profile and thus the diffusion data. In particular,

the utilisation of information from different information depths (due to different EALs of electrons from different Auger transitions or core levels) in the multiple profile fitting procedure increases the reliability of the deduced genuine concentration-depth profile. An example of such a multiple profile (Ge_{LMM}, Si_{KLL} and Si_{LMM}) fitting of an as-prepared a-Si/pc-Ge specimen is given in Fig. 2.1.

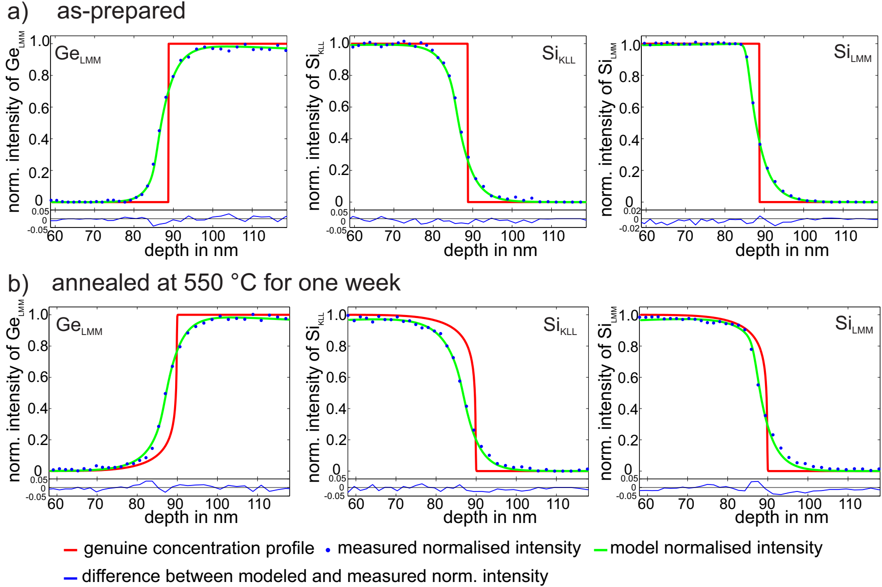

Figure 2.1: Multiple profile fitting to measured AES intensity-depth profiles (Ge_{LMM}, Si_{KLL} and Si_{LMM}) of a) as-prepared and b) diffusion-annealed a-Si/pc-Ge bilayered thin film.

2.4 Extended MRI model

2.4.1 Concentration dependent MRI parameters

In general, the parameter for mixing [94], w, and the EAL [92], λ, are concentration dependent, whereas the roughness parameter, σ, is considered to be independent of concentration [95].

If the MRI parameter for mixing and/or the EAL are dependent on concentration, then g depends on sputter depth and the convolution in Eq. 2.1 does not hold. Note that the mixing length changes gradually upon approaching

concentration variations in the specimen during sputter-depth profiling. The smearing of the genuine concentration-depth profile by mixing, information depth and roughness then has to be calculated following a numerical calculation scheme. Firstly, the contribution due to surface and interface roughness is considered by the convolution of the genuine concentration-depth profile with Eq. 2.4. Secondly, the differential equation [96]

$$\frac{dX_z}{dz} = \frac{1}{w_z}\left(X^0_{z+w} - X_z\right) \cdot \left(1 + \frac{dw_z}{dz}\right) \tag{2.8}$$

is solved. Here X^0_{z+w} is the genuine concentration convoluted with the roughness contribution at the end of the mixed region and X_z the by mixing affected concentration at the instanteneous surface of the specimen at the sputter-depth z. Thirdly, the intensity of Auger- or photoelectrons from regions below the occuring specimen surface have to be corrected by their information depth according to

$$\begin{aligned}\frac{I(z)}{I^0} &= \sum_{z'=z+\Delta}^{z+w} X(z') \cdot \exp\left(-\tfrac{\Delta}{\lambda(z'-\Delta)}\right) \cdot \left(1 - \exp\left(-\tfrac{\Delta}{\lambda(z')}\right)\right) \\ &+ \sum_{z'=z+w+\Delta}^{\infty} X^0(z') \cdot \exp\left(-\tfrac{w+\Delta}{\lambda(z'-\Delta)}\right) \cdot \left(1 - \exp\left(-\tfrac{\Delta}{\lambda(z')}\right)\right)\end{aligned} \tag{2.9}$$

where I^0 is the elemental standard intensity and Δ the discretisation of the depth scale in the numerical calculation scheme.

Although the concentration dependence of w and λ has been recognised before [75, 88, 97, 98], it has hitherto not been applied to experimental profiles. In particular for material systems composed of light and heavy elements the concentration dependence of especially the mixing parameter can become important, resulting in pronounced asymmetry of the normalised intensity-depth profile as demonstrated by model calculations for an undiffused Mg/Au bilayer (see Fig. 2.2). The values for w_{Mg} and w_{Au} were taken from SRIM [94].

For the concentration dependence of the MRI parameter for mixing, w, the back-scatter correction factor, R, the mean effective backscattering decay length, L, and the sputter rate, $\dot{z}$, a linear function can be adopted. Therefore, only the values for the pure components have to be taken from literature or from a fit (step (i); see section 2.2) to an as-prepared specimen with known genuine concentration-depth profile. Analogously, for the concentration dependence of the EAL, a linear concentration dependence of the attenuation cross section (i.e. $1/[\lambda \cdot \cos\phi]$) is adopted [75].

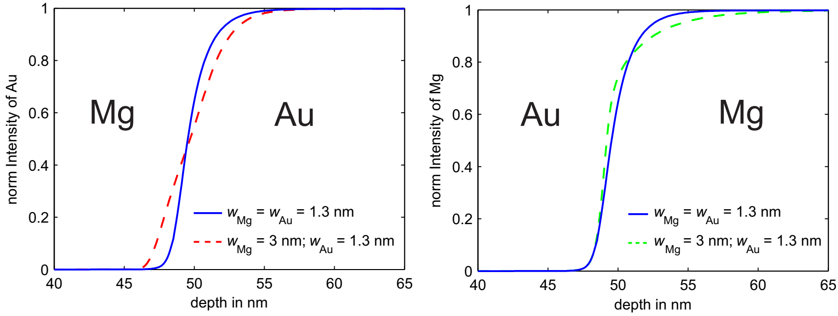

Figure 2.2: Influence of different mixing parameters, w, for undiffused Mg/Au bilayers on the normalised intensity vs. sputter-depth profiles. Sputter conditions: 1 keV Ar^+, incidence angle 42°; MRI parameters: $\lambda = \sigma = 0.5$ nm, $z_0 = 50$ nm.

2.4.2 Backscatter correction

For AES sputter-depth profiling a backscatter correction has to be applied, if the backscattering correction factors of the elements in the investigated system are different, i.e. the primary intensity without the contribution due to backscattered electrons has to be multiplied by a backscattering correction factor to yield the measured intensity. A backscatter correction has been implemented into the MRI model for as-prepared bilayers [89] and multilayers [99] with sharp interfaces, but the effect of smeared interfaces (as due to significant interdiffusion) on the backscatter correction has not been considered until now. To implement a backscatter correction for specimens with a composition varying with depth, a concentration dependent backscattering correction factor, $R(z'(c))$, (as provided by Ref. [100]) is assigned to each depth z' with concentration c. The effective backscattering correction factor, $R_{\text{eff}}(z)$, for the actual sputter depth, z, is then calculated according to

$$\begin{aligned} R_{\text{eff}}(z) - 1 \quad &= \int_z^{z_{\text{sub}}} \frac{1}{L}[R(z') - 1] \exp\left(-\frac{z'-z}{L}\right) dz' \\ &+ [R(z'_{\text{sub}}) - 1] \cdot \exp\left(-\frac{z'_{\text{sub}}-z}{L}\right), \end{aligned} \tag{2.10}$$

where z_{sub} is the depth of the interface between the thin film (bilayer/multilayer) and the substrate and L denotes the mean effective backscattering decay length, which is obtained for each pure component from the fit to an as-prepared specimen (step (i); see section 2.2).

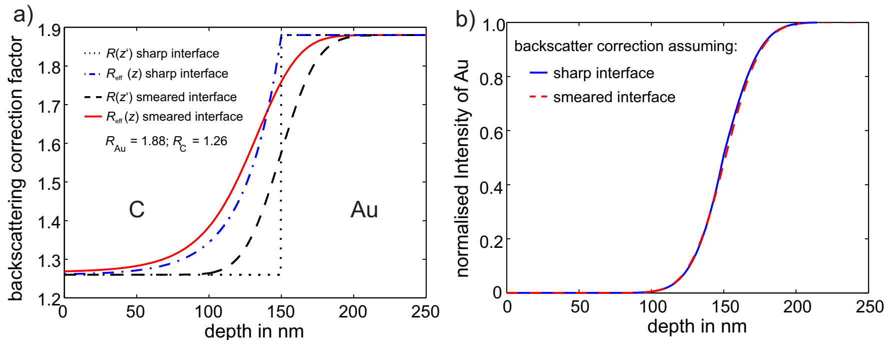

Figure 2.3: a) Backscattering and effective backscattering correction factors for an assumed sharp interface (according to [99]) and for an assumed strongly diffusion smeared interface ($Dt = 200$ nm^2) of a C/Au bilayer. R values of the system components are strikingly different. b) Calculated normalised intensity-depth profiles for the specimen with the strongly (diffusion) smeared C/Au interface, assuming for the calculation of R_{eff} either a sharp interface or adopting the genuine, smeared concentration-depth profile. Evidently, performing the backscatter correction with the genuine, smeared concentration-depth profile (instead of a non-physical sharp interface) is of minor importance. MRI parameters: $z_0 = 150$ nm$, L_{\text{C}} = L_{\text{Au}} = 25$ nm, $\sigma = \lambda = w = 0.5$ nm.

The influence of a smeared interface on $R_{\text{eff}}(z)$ increases with increasing interface width and decreasing mean effective backscattering decay length, L, due to a relatively increasing contribution of backscattered electrons from the smeared interface region. As an example, Fig. 2.3 shows the calculated effective backscattering correction factors and the normalised intensity-depth profile of Au for an extreme case of a very smeared interface and strikingly different backscattering correction factors of the system components (i.e. as holds for the C/Au system considered). It follows that the influence of a smeared interface on the backscatter correction of the normalised intensity-depth profile is minor (≤ 3 %) even for such an extreme case.

2.4.3 Sputter-depth to sputter-time conversion

Often a constant mean sputter rate is assumed for the entire depth range of the multi-element specimen [101]. However, in most cases the sputter rates of the different elements in the investigated system are different. This introduces an asymmetry in the calculated intensity-depth profiles upon sputter-

depth to sputter-time conversion. To account for different elemental sputter rates, a linear concentration dependence of the sputter rate can be used as a first approximation [102]. The elemental sputter rates of the individual elements can be determined from an as-prepared specimen with a sharp interface.

In each step of the iterative fitting procedure the for this step genuine concentration-depth profile is convoluted with the ion-bombardment induced mixing contribution, g_w, and the thus resulting mixing smeared concentration-depth profile is used for the sputter-depth to sputter-time conversion of the calculated normalised intensity-depth profile for the comparison with the measured normalised intensity-sputter time profile.

As a conclusion of the above subsections: The values of the MRI parameters w_A, w_B, L_A, L_B and σ have to be determined from multiple profile fitting to a reference specimen (step (i); see section 2.2), whereas the EAL values, λ_A and λ_B, and the backscattering correction factors, R_A and R_B, of the pure elements are directly taken from literature data [92, 100]. The sputter rates, $\dot{z}_\mathrm{A}$ and $\dot{z}_\mathrm{B}$, are obtained from an as-prepared specimen with a sharp interface.

2.4.4 Numerical calculation of diffusion profiles

Due to the forward calculation approach (see section 2.2), a realistic (numerical) description of the genuine concentration-depth profile is required. To this end, for concentration-depth profiles resulting from interdiffusion, in this work Fick's second law is solved numerically using a fully implicit finite difference scheme [103]. The chemical diffusion coefficient $\widetilde{D}$ can be calculated from the intrinsic diffusion coefficients D_A and D_B according to the Darken equation [45]. The intrinsic diffusion coefficients depend on concentration through both the self-diffusion coefficient and the thermodynamic factor. The thermodynamic factor, Φ, can be taken from literature data [104]. The concentration dependence of the self-diffusion coefficients can be included by e.g. an exponential concentration dependence as in the crystalline Si/Ge system [105] according to

$$D_\mathrm{A}(x_\mathrm{B}) = \left[D^*_\mathrm{A,A} \cdot \exp(-m \cdot x_\mathrm{B})\right] \cdot \Phi, \tag{2.11}$$

where $D_\mathrm{A}(x_\mathrm{B})$ is the intrinsic diffusion coefficient of A at concentration x_B, $D^*_\mathrm{A,A}$ is the self-diffusion coefficient of A in pure A, m is an "asymmetry" factor, which describes the concentration dependence of the self-diffusion coefficient and Φ denotes the thermodynamic factor. The self-diffusion coefficients in the pure components (i.e. $D^*_\mathrm{A,A}$, $D^*_\mathrm{A,B}$, $D^*_\mathrm{B,A}$ and $D^*_\mathrm{B,B}$) serve as

fitting parameters during the iterative multiple profile fitting procedure (step (ii); see section 2.2). The start values for the fitted self-diffusion coefficients have to be of about the same order of magnitude as the final values.

The above described procedure allows determination of concentration dependent self-diffusion coefficients and thus, with knowledge of thermodynamic data, the determination of the concentration dependent interdiffusion coefficient.

2.5 Application of the extended MRI model to interdiffusion in a-Si/pc-Ge bilayered thin films

The here presented multiple profile fitting procedure has been applied to investigate interdiffusion in amorphous-Si/polycrystalline Ge thin films, i.e. to determine the self-diffusion coefficients of Ge and Si *in a-Si* from the AES sputter-depth profiles recorded for the Si_{LMM}, Si_{KLL} and Ge_{LMM} Auger transitions (see Appendix 2.B). The investigation of interdiffusion in amorphous thin films is challenging, since, to prevent crystallisation, only relatively low annealing temperatures can be applied, which implies only very small diffusion lengths of at most a few nanometres.

The concentration dependence of the mixing parameter in the system Si ($w = 2.75$ nm)/ Ge ($w = 3$ nm) is small and the concentration dependence of the backscattering correction factors have a negligible influence on the calculated intensity-depth profiles (see above and Fig. 2.3). However, the concentration dependence of the sputter rate, $\dot{z}$, ($\dot{z}_{Ge}/\dot{z}_{Si} = 1.4$) has to be taken into account in the sputter-time to sputter-depth conversion. The same nominal concentration dependence of the self-diffusion coefficients of Ge and Si is assumed (as a consequence: $D^*_{Si,Si} = D^*_{Ge,Si}$). Note that due to the low annealing temperature, the self-diffusion coefficient of Si *in pure Ge* is thus small that the diffusion zone in the originally pure Ge sublayer ($\sqrt{Dt} < 1$ nm) covers a depth range smaller than the resolution limit.

An Arrhenius plot of the self-diffusion coefficient of Ge *in pure Si*, as determined by the single and the multiple profile fitting procedures, is shown in Fig. 2.4. Obviously, for the single profile fittings, the fitted self-diffusion coefficients, $D^*_{Ge,Si}$ and the deduced activation energy, strongly depend on the chosen AES transition. Because the number of experimental data used for the determination of the MRI parameters (in step (i); see section 2.2) is much larger in case of multiple profile fitting than in case of single profile fitting, it is likely that the MRI parameters, as determined by multiple profile fitting from the reference specimen, are more reliable than those obtained by single profile fitting. See for example Fig. 2.5a, which shows the physically

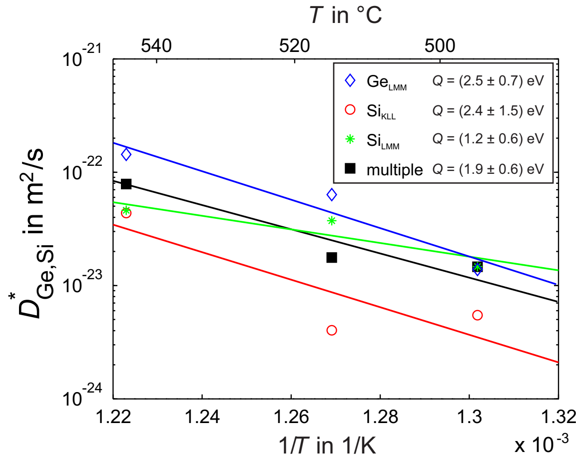

Figure 2.4: a) Arrhenius plot for the determined self-diffusion coefficients of Ge *in pure a-Si*, $D^*_{\mathrm{Ge,Si}}$, in bilayered a-Si/pc-Ge specimens. $D^*_{\mathrm{Ge,Si}}$ strongly depends on the AES transition used for the evaluation. The errors of the self-diffusion coefficient of Ge *in pure a-Si* obtained by single profile fitting of the $\mathrm{Ge_{LMM}}$, $\mathrm{Si_{KLL}}$ and $\mathrm{Si_{LMM}}$ transitions are $3.4 \cdot 10^{-23}\ \frac{\mathrm{m}^2}{\mathrm{s}}$, $17.6 \cdot 10^{-23}\ \frac{\mathrm{m}^2}{\mathrm{s}}$ and $7.1 \cdot 10^{-23}\ \frac{\mathrm{m}^2}{\mathrm{s}}$, respectively, whereas for multiple profile fitting this error amounts to $7.0 \cdot 10^{-23}\ \frac{\mathrm{m}^2}{\mathrm{s}}$, for all annealing temperatures.

impossible variation in the value of σ as determined by the single profile fittings using different (in this case Auger) transitions.

The sensitivity of the fitted self-diffusion coefficients for variations in the MRI model parameters was assessed by fitting the $\mathrm{Si_{LMM}}$, $\mathrm{Si_{KLL}}$ and $\mathrm{Ge_{LMM}}$ normalised intensity-sputter time profiles as recorded for one diffusion-annealed specimen by multiple profile fitting and by single profile fittings. One MRI parameter was changed for each fit, while the others were kept constant. The slope of the linear line fitted to the obtained fitted self-diffusion coefficients, as a linear function of the changed MRI parameter, was taken as the sensitivity parameter, $dD^*_{\mathrm{Ge,Si}}/dx$, and is shown in Fig. 2.5b. In case of single profile fitting, small variations in w_{Ge}, w_{Si}, σ, $\dot{z}_{\mathrm{Ge}}$ and $\dot{z}_{\mathrm{Si}}$ can have large influences on the fitted self-diffusion coefficient of Ge *in pure Si* (see single profile fitting of the $\mathrm{Si_{KLL}}$ normalised intensity-depth profile), whereas these effects are generally smaller in case of multiple profile fitting.

Now the errors in the self-diffusion coefficient, owing to uncertainties in the MRI model parameters are estimated as follows. An uncertainty of

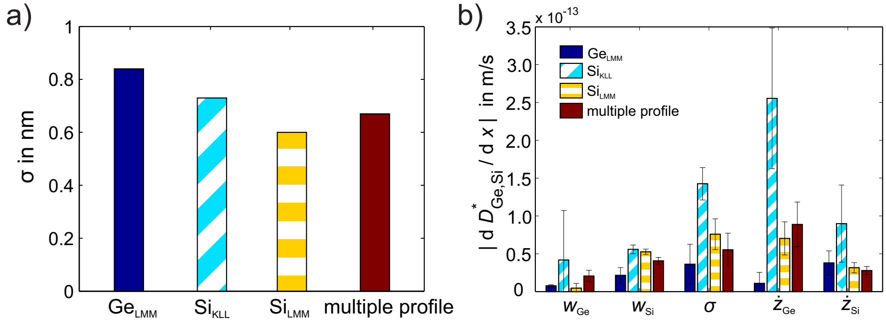

Figure 2.5: a) The roughness parameter, σ, as obtained from multiple and single profile fitting. b) Variation of the fitted self-diffusion coefficient for Ge *in pure a-Si*, $D^*_{\mathrm{Ge,Si}}$, upon variation of the MRI model parameter (x) for multiple and single profile fitting.

0.3 nm is assumed for w_{Ge}, w_{Si} and σ, and an uncertainty of 0.3 nm/min for $\dot{z}_{\mathrm{Ge}}$ and $\dot{z}_{\mathrm{Si}}$. It then follows that the error of the self-diffusion coefficient of Ge *in pure a-Si* as obtained by single profile fittings for the $\mathrm{Ge_{LMM}}$, $\mathrm{Si_{KLL}}$ and $\mathrm{Si_{LMM}}$ transitions is $3.4 \cdot 10^{-23}$ m^2/s, $17.6 \cdot 10^{-23}$ m^2/s and $7.1 \cdot 10^{-23}$ m^2/s, respectively, whereas for multiple profile fitting this error amounts to $7.0 \cdot 10^{-23}$ m^2/s.

Meeting the criteria which are often applied to justify single profile fitting [88], like a small EAL or a high intensity of the investigated Auger or photoelectrons, is not sufficient. The sensitivity as well as the error of the fitted self-diffusion coefficients is larger for single profile fitting of the $\mathrm{Si_{LMM}}$ normalised intensity-depth profile than for single profile fitting of the $\mathrm{Ge_{LMM}}$ normalised intensity depth-profile (the Auger electrons of the $\mathrm{Si_{LMM}}$ transition have a smaller EAL and a higher intensity, as compared to the Auger electrons of the $\mathrm{Ge_{LMM}}$ transition). Considering all available normalised intensity-depth profiles simultaneously in a multiple profile fitting, is a more constrained fitting than single profile fitting and avoids the problem of choosing a normalised intensity-depth profile for the determination of diffusion data. The reliability of the obtained diffusion data is thereby increased (see figure 2.4).

2.6 Conclusions

(i) The normalisation of measured intensity-sputter time profiles of Auger electrons and photoelectrons, determined for thin film systems, by only the corresponding elemental sensitivity factor allows the *simultaneous* fitting of all measured and thus normalised intensity-sputter time profiles. This multiple profile fitting procedure increases pronouncedly the number of independent experimental data used in the evaluation and uses information obtained from different information depths, as compared to the usually applied single profile fitting. As a result, by application of the multiple profile fitting the general sensitivity of the obtained genuine concentration-depth profile and the derived diffusion data on errors in the parameters for mixing, roughness and sputter rate is generally reduced and the reliability of the diffusion data is increased, as compared to single profile fitting.

(ii) The concentration dependences of the MRI parameters for mixing, information depth, backscattering correction factor, mean effective backscattering decay length and sputter rate have been incorporated in the MRI model. The influence of diffusion-annealed, smeared interfaces on the backscatter correction was found to be negligible. However, for the sputter-depth to sputter-time conversion, with concentration dependent sputter rates, a correction for ion-bombardment induced mixing has to be applied.

(iii) Application of the developed multiple profile fitting procedure to diffusion-annealed a-Si/pc-Ge bilayers (diffusion lengths in the range of 4-10 nm) demonstrates that the results obtained by multiple profile fitting are generally more accurate and consistent than those obtained by the single profile fittings.

Acknowledgements

The authors are grateful to Prof. S. Hofmann and Dr. L. P. H. Jeurgens for helpful discussions and to Dipl.-Ing. B. Siegle for carrying out the AES measurements.

Appendix 2.A Specimen preparation

Si/Ge bilayers were deposited via thermal evaporation on Si(111) substrates covered with a native oxide layer in a customized multi-chamber ultrahigh vacuum (UHV) system at a base pressure $< 3{\cdot}10^{-8}$ Pa. Firstly, an a-Ge layer with a thickness of 91 nm was deposited with a deposition rate of 4.8 nm/min at room temperature by thermal evaporation of pure Ge (99.999 %) from

a pyrolytic graphite (PGR) crucible and a high temperature effusion cell. After removing the specimen from UHV, crystallisation of the a-Ge thin film was performed in argon atmosphere in a tube furnace at 460 °C for 2 h to obtain micro-crystalline Ge thin-films with a grain size of ≈ 2 μm. Then the specimen was reintroduced into the UHV system and the developed oxide layer was removed by a thermal heat treatment in ultra high vaccum at 250 °C for 1 h and successively at 450 °C for 7 min. As confirmed by *in-situ* XPS, the oxide layer was completely removed after this thermal heat treatment. Subsequently, a-Si thin-film deposition with a thickness of 95 nm was performed at room temperature by thermal evaporation of pure Si (99.999 %) from a tungsten crucible on oxygen free polycrystalline Ge thin-films.

Diffusion-annealing was performed in quarz ampoules filled with Ar in a salt bath (6050H from Hart Scientific) for one week in a temperature range from 495 °C to 544 °C. The annealing temperature was calibrated with a platinum resistance thermometer (5624 from Hart Scientific).

Appendix 2.B AES sputter-depth profiling

Auger peaks of Si_{LMM} (kinetic energy = 92 eV), Si_{KLL} (1610 eV), Ge_{LMM} (1140 eV), O_{KLL} (503 eV) and C_{KLL} (272 eV) were recorded with a JEOL JAMP-7830F AES system equipped with a field emission electron gun and a hemispherical analyser. The primary electron beam had an energy of 10 keV and was inclined by 30° with respect to the specimen-surface normal of the specimen. Sputter-depth profiling was performed with Ar^{+} ions with a kinetic energy of 1 keV under an incidence angle of 40.5° in the intermittent mode and sputter steps between 20 s and 1 min. Auger electrons were detected under an angle of 25° with respect to the specimen-surface normal in scanning mode over an area of 10 × 10 μm.

Measured AES spectra were differentiated by a 7 point-algorithm as implemented in MultiPak from Physical Electronics and then fitted with a linear least squares fitting procedure, or in the case of overlapping AES spectra, with the target factor analysis. For the target factor analysis, depth regions occupied by the pure elements could be used as internal standards for the profile fitting.

Chapter 3

Concentration-dependent self-diffusion coefficients in amorphous $Si_{1-x}Ge_x$ solid solutions; an interdiffusion study

Martin A. Noah[1], David Flötotto[1], Zumin Wang[1], and Eric J. Mittemeijer[1,2]

[1] *Max Planck Institute for Intelligent Systems (formerly Max Planck Institute for Metals Research), Heisenbergstr. 3, D-70569 Stuttgart, Germany*
[2] *Institute for Materials Science, University of Stuttgart, Heisenbergstr. 3, D-70569 Stuttgart, Germany*

Abstract

Self-diffusion coefficients of Si and Ge in amorphous $Si_{1-x}Ge_x$ (a-$Si_{1-x}Ge_x$) solid solutions were determined quantitatively in the temperature range of 440 °C - 460 °C by the investigation of interdiffusion in amorphous Si/$Si_{0.52}Ge_{0.48}$ multilayers using Auger electron spectroscopy sputter-depth profiling. The determined concentration dependent self-diffusion coefficients of Si and Ge in a-$Si_{1-x}Ge_x$ with $0 \leq x \leq 48$ at.% Ge are about ten orders of magnitude larger than in the corresponding crystalline phases, due to the inherent, excess free volume in the amorphous phase. The self-diffusion coefficient of Si (or Ge) in a-$Si_{1-x}Ge_x$ increases in association with a decreasing activation enthalpy with increasing Ge concentration. This concentration dependence has been related to an overall decrease of the average bond strength with increasing Ge concentration.

3.1 Introduction

Amorphous semiconductors, such as amorphous Si, Ge, and the amorphous solid solutions $Si_{1-x}Ge_x$, are crucial materials in a number of state-of-the-art technologies such as thin-film photovoltaic devices and thin-film transistors, due to e.g. their high, tailorable optical absorption [106] in combination with satisfactory electronic properties [107], and the easy, low-cost manufacturing process even on flexible substrates [14, 108]. Knowledge of diffusion in such amorphous semiconductors is of vital importance for production and real-life applications of devices based on these materials. Furthermore, the classic substitutional (self-)diffusion mechanism based on vacancies is likely not operative in amorphous solids [18]. Against this background, the rate and mechanism of self-diffusion in amorphous semiconductors become scientifically highly intriguing.

However, in contrast with what is known for their crystalline counterparts, experimental self-diffusion data are rare for amorphous semiconductors, and consequently, the mechanism of self-diffusion in amorphous semiconductors has remained largely unknown until now. The reason for the lack of (self-)diffusion data in amorphous solids is the metastability of amorphous materials: often crystallization occurs before any diffusion can be detected. Therefore, techniques which are able to resolve diffusion lengths in the nanometer range are mandatory to investigate diffusion in amorphous materials. To this end, X-ray [29, 30] and neutron [31] diffraction techniques on mutlilayered specimens have been applied to investigate interdiffusion in amorphous $Si_{1-x}Ge_x$ (a-$Si_{1-x}Ge_x$) solid solutions. However, such methods cannot account for the concentration dependence [91, 109–111] of the diffusion coefficients in a-$Si_{1-x}Ge_x$ straightforwardly due to the indirect way of determination of the concentration-depth profile by these methods.

In this study, interdiffusion in a-Si/a-$Si_{0.52}Ge_{0.48}$ multilayers at 440 °C - 460 °C has been investigated by Auger electron spectroscopy (AES) sputter-depth profiling applying the Mixing Roughness Information depth (MRI) model [37, 85, 112] to account for sputter-induced alterations of the measured intensity-depth profiles. This analysis allows to reveal diffusion lengths in the nanometer range [37, 112] and, in contrast with the mentioned X-ray and neutron diffraction methods, enables a direct determination of the concentration-depth profiles. On the basis of thus established concentration-depth profiles, in this work the concentration dependent Si and Ge self-diffusion coefficients in a-$Si_{1-x}Ge_x$ (for $x \leq 48$ at.% Ge) have been deduced and conclusions on the self-diffusion mechanism in amorphous semiconductors have been obtained.

3.2 Experimental procedure

3.2.1 Specimen preparation and microstructural characterization

Amorphous Si/amorphous $Si_{0.52}Ge_{0.48}$ multilayer specimens were prepared in a customized ultrahigh vacuum (UHV) system (base pressure $< 3{\cdot}10^{-8}$ Pa) by thermal (co-) evaporation of pure Si (from a tungsten/tantalum crucible) and pure Ge (from a pyrolytic graphite crucible) (both, Si and Ge, have a purity $>$ 99.999 wt.%) on a Si(001) substrate covered with a 50 nm thick layer of Si_3N_4. Before deposition, the substrate was ultrasonically cleaned successively in aceton and isopropanol and degassed for one hour at 200 °C in UHV. After cooling the substrate to room temperature, a 50 nm thick a-$Si_{0.52}Ge_{0.48}$ solid solution layer was deposited by co-deposition of Si and Ge. Next, pure a-Si and a-$Si_{0.52}Ge_{0.48}$ sublayers with a thickness of 20 nm each were deposited alternatingly up to three times without breaking the UHV. Finally a 50 nm thick pure a-Si capping layer was deposited on top of the multilayer specimen.

The thus prepared specimen was removed from the UHV system, cut into small pieces which were encapsulated in Ar filled quartz ampules. Diffusion annealing was performed in a tube furnace at 440 °C, 450 °C and 460 °C for annealing times of 260 h, 504 h and 672 h.

The microstructure of the as-prepared and the diffusion annealed specimens was investigated by X-ray diffraction (XRD) applying a Bruker D8 diffractometer employing parallel Cu Kα radiation ($\lambda = 1.5406\,\text{Å}$). Θ-2Θ-scans were recorded in a 2Θ range between 24° to 32° with a step size of 0.02° and a measurement time of 300 s to 600 s per step. To avoid any overlap with reflexes from the Si(001) substrate, the specimen was tilted by 5° with respect to the specimen-surface normal.

In addition, the microstructure of the as-prepared and diffusion annealed specimen (460 °C for 504 h and 260 h) were investigated by cross-sectional TEM investigations in Philips CM 200 and in JEOL 4000FX microscopes, operating at an acceleration voltage of 200 kV and 400 kV, respectively. TEM cross-sectional specimens were prepared by applying a so called tripod-polishing method [113]. To this end the specimens were cut into small pieces with a diamond saw and glued together with facing specimen surfaces. The prepared specimen sandwich was pre-thinned perpendicular to the glue joint with a tripod polisher to a thickness of about 10 µm and subsequently thinned by ion milling with an energy of 2.7 keV, while cooling the specimen with liquid nitrogen.

3.2.2 Auger electron spectroscopy sputter-depth profiling

To determine the concentration-depth profiles, AES sputter-depth profiling of the as-prepared and diffusion annealed specimens was conducted with a JEOL JAMP-7830F AES system equipped with a hemispherical analyzer and a field emission electron gun operating at an acceleration voltage of 10 kV and a beam current of 10 nA (see supplementary material of Ref. [112] for details). Sputter-depth profiling was performed with a focused 1 keV Ar^+ ion beam (rastering over the specimen surface) in an intermittent mode with sputter steps of 20 s - 60 s (corresponding to depth steps of 1.1 nm - 3.3 nm). After each sputter step, spectra of the Si_{LMM} (kinetic energy = 92 eV), Si_{KLL}(1610 eV), Ge_{LMM}(1140 eV), O_{KLL}(503 eV) and C_{KLL}(272 eV) Auger transitions were recorded with an energy step size of 1 eV while scanning the primary electron beam over an area of 10 µm × 10 µm. The measured AES spectra were differentiated by a 7 point-algorithm and fitted either with a linear least squares fitting procedure, or in the case of overlapping AES spectra, according to the target factor analysis [114].

In order to account for sputter-induced alterations, such as ion bombardment induced atomic mixing and surface roughening, as well as for the intrinsic specimen surface and interface roughness, in the measured intensity-depth profiles, an (extended) Mixing-Roughness-Information depth (MRI) model was applied [112]. Thereby, the genuine (i.e unsmeared) concentration-depth profile was determined in a forward calculation approach. A detailed description of the model and its application to interdiffusion studies in thin films is given in Ref. [112].

3.3 Results

3.3.1 Microstructure before and after diffusion annealing

As verified by XRD as well as TEM analyzes, the as-prepared multilayer is entirely amorphous (see figures 3.1a-b). No diffraction peaks and no diffraction spots of any crystalline phase were observed in the XRD patterns (see figure 3.1a) and in the selected area electron-diffraction patterns (see inset in figure 3.1b). TEM analysis of the as-prepared specimen revealed a small number of void channels running perpendicular to the surface in particular in the a-Si sublayers (see figure 3.1b), which might have formed as a result of growth instabilities due to the low atomic mobilities of Si and Ge at the deposition conditions [66]. These void channels allowed the penetration of a small amount of oxygen from the outer surface into the a-Si capping

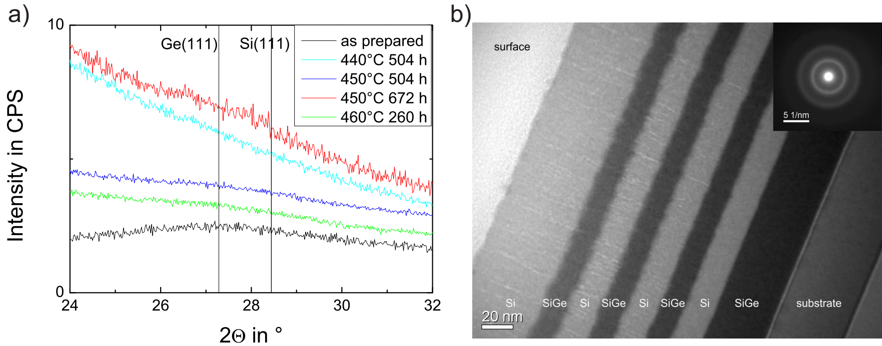

Figure 3.1: a) X-ray diffraction pattern (employing Cu Kα radiation) of an amorphous a-Si/a-$Si_{0.52}Ge_{0.48}$ multilayer specimen in the as-prepared state and after diffusion annealing. The positions for the Ge(111) and Si(111) reflections have been indicated. Evidently, no diffraction peaks can be detected in the measured diffraction patterns. b) Cross-sectional TEM bright field image of an as-prepared Si/$Si_{0.52}Ge_{0.48}$ multilayer specimen. The selected area electron diffraction pattern confirms the amorphous structure of the specimen. Note the void channels running perpendicular to the specimen surface especially in the a-Si sublayers (see the "stripes").

layer.[1] No contamination by oxygen or carbon could be detected by AES beyond a depth of 50 nm (i.e. after the first a-Si/a-$Si_{0.52}Ge_{0.48}$ interface).[2] Applying the extended MRI model, the measured Ge_{LMM}, Si_{KLL} and Si_{LMM} intensity-depth profiles of the as-prepared multilayer can be well described with a single set of MRI parameters for the case of sharp interfaces, thereby indicating the step-like nature of the initial concentration-depth profile (see figure 3.3a).

After diffusion annealing for the highest annealing temperature (460 °C) and the longest annealing time (504 h), partial crystallization of the a-$Si_{0.52}Ge_{0.48}$ sublayers can be observed at some locations in the multilayer according to the TEM analysis, while the pure a-Si sublayers remain entirely

[1] The presence of oxygen in the a-Si capping layer can reduce the measured intensity of the low energetic Si_{LMM} transition (effective attenuation length of 0.42 nm), whereas the high energetic Si_{KLL} and Ge_{LMM} transitions (effective attenuation lengths of 3.17 nm and 2.03 nm, respectively) are practically unaffected (this is compatible with the experimental data shown in figure 3.3a).

[2] The detection limit is estimated, neglecting any matrix effects, according to Ref. [115] to be 1.0 at.% for O_{KLL}, 2.0 at.% for C_{KLL}, 2.2 at.% for Si_{KLL}, 0.9 at.% for Si_{LMM} and 1.0 at.% for Ge_{LMM}, respectively.

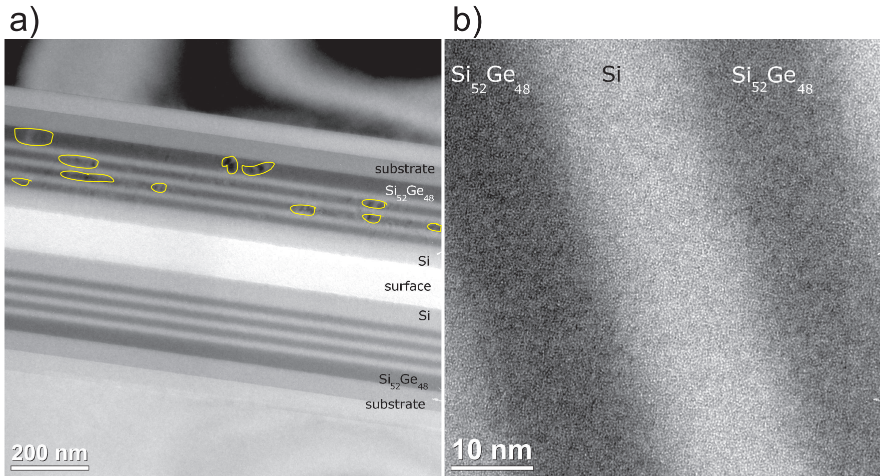

Figure 3.2: a) Cross-sectional TEM bright field image of a $Si/Si_{0.52}Ge_{0.48}$ multilayer after diffusion annealing for 504 h at 460 °C. Partial crystallization of the $Si_{0.52}Ge_{0.48}$ sublayers has occurred in some areas after diffusion annealing (marked with circles), while the pure a-Si sublayers have remained entirely amorphous. b) Cross-sectional TEM high resolution image of a $Si/Si_{0.52}Ge_{0.48}$ multilayer after diffusion annealing for 504 h at 460 °C demonstrating the fully amorphous structure of parts of the specimen.

amorphous (see figures 3.2a-b). XRD analysis demonstrates that no diffraction peaks emerge in the diffraction pattern (see figure 3.1a): this implies that a possibly crystallized fraction is in any case less than 5 vol.%. After diffusion annealing for shorter times (260 h at 460 °C) no crystalline areas can be observed at all in TEM.

3.3.2 Concentration-depth profiles after diffusion annealing and determination of concentration dependent self-diffusion coefficients

The measured AES intensity-depth profiles after diffusion annealing at 460 °C for 504 h reveal an asymmetric change in the concentration-depth profile of the multilayer (see figure 3.3b). While the Ge concentration in the initially a-$Si_{0.52}Ge_{0.48}$ sublayers decreased considerably, no Ge could be detected in the initially pure a-Si sublayers after diffusion annealing. Hence, the diffusion of Si into the a-$Si_{0.52}Ge_{0.48}$ sublayers is much faster than the diffusion of Ge into the pure a-Si sublayers. This observed diffusional asym-

metry indicates that the chemical diffusion coefficient of a-$Si_{1-x}Ge_x$ solid solutions is strongly concentration dependent, as is the case for crystalline $Si_{1-x}Ge_x$ [105, 116]. Hence, the genuine concentration-depth profiles obviously cannot be described with a simple error-type function.

The concentration dependence of the chemical diffusion coefficient has been described in the present diffusion model, incorporated in the MRI forward calculation approach (see Ref. [112]), as follows. The chemical diffusion coefficient as function of the concentration-dependent intrinsic diffusion coefficients is described according to the Darken equation.[3] The intrinsic diffusion coefficients of Si, $D_{\mathrm{Si}}(x)$, and Ge, $D_{\mathrm{Ge}}(x)$, depend on the a-$Si_{1-x}Ge_x$ composition (i.e. the Ge fraction, $x = x_{\mathrm{Ge}}$), through both the self-diffusion coefficients and the thermodynamic factor, Φ, according to

$$\begin{aligned} D_{\mathrm{Si}}(x) &= D^*_{\mathrm{Si\ in\ a\text{-}Si_{1-x}Ge_x}}(x) \cdot \Phi(x) \\ &= [D^*_{\mathrm{Si\ in\ Si}} \cdot \exp(-m_{\mathrm{Si}} \cdot x)] \cdot \Phi(x) \qquad (3.1a) \\ D_{\mathrm{Ge}}(x) &= D^*_{\mathrm{Ge\ in\ a\text{-}Si_{1-x}Ge_x}}(x) \cdot \Phi(x) \\ &= [D^*_{\mathrm{Ge\ in\ Ge}} \cdot \exp(-m_{\mathrm{Ge}} \cdot (1-x))] \cdot \Phi(x), \qquad (3.1b) \end{aligned}$$

where $D^*_{\mathrm{Si\ in\ Si}}$ and $D^*_{\mathrm{Ge\ in\ Ge}}$ are the self-diffusion coefficients of Si in pure Si and Ge in pure Ge, respectively, and m_{Si} and m_{Ge} are "asymmetry" factors, which describe the concentration dependence of the self-diffusion coefficient of Si and Ge, respectively. Here an exponential concentration dependence of the self-diffusion coefficients is adopted, which is well fulfilled in *crystalline* $Si_{1-x}Ge_x$ solid solutions [105, 116], and which may follow from a linear concentration dependence of the activation enthalpy for self-diffusion.

For the completely miscible $Si_{1-x}Ge_x$ system, the thermodynamic factor, Φ, can be well approximated [119] by adopting the regular solution model which leads to

$$\Phi = 1 - 2x(1-x)\frac{\Omega}{RT}, \qquad (3.2)$$

where Ω is the interaction parameter, R is the universal gas constant and T is the absolute temperature. Although thermodynamic data for a-$Si_{1-x}Ge_x$ solid solutions are rather rare, theoretical [120, 121] and experimental [30] studies consistently indicate that, in contrast with the demixing tendency found in crystalline $Si_{1-x}Ge_x$ solid solutions [104, 119, 122–124], a mixing

[3] The transition from the Nernst-Planck regime, pertaining to small diffusion lengths, to the Darken regime, pertaining to large(r) diffusion lengths, in amorphous materials as proposed by Stephenson [117] is estimated to be 1 nm [118] and thus below the diffusion lengths in this study (> 2.2 nm).

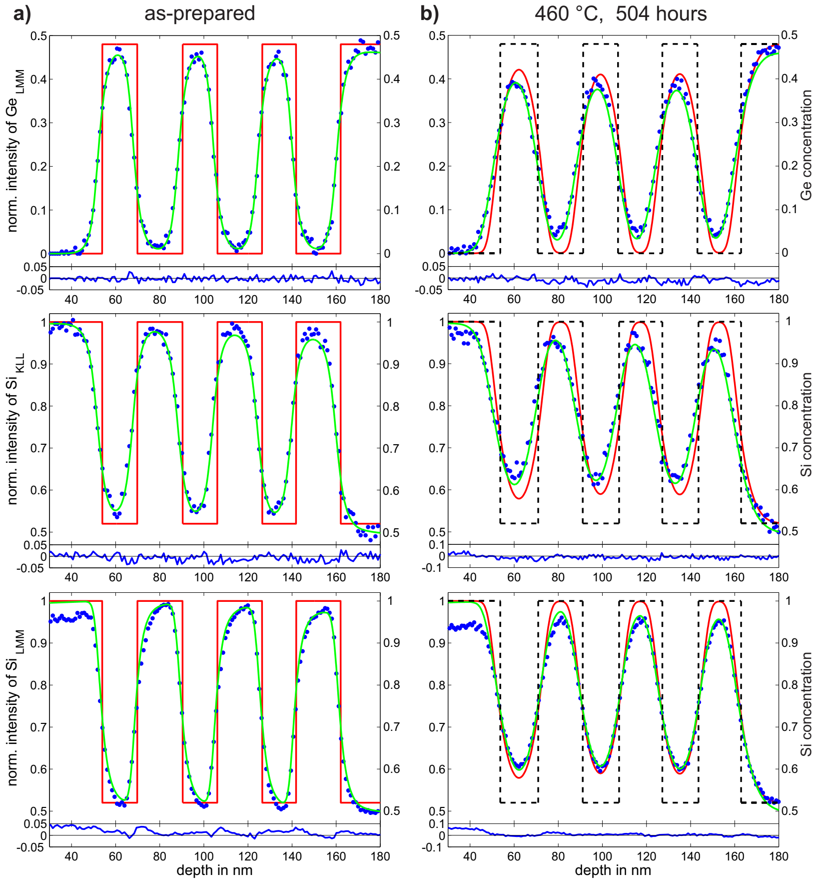

Figure 3.3: Normalized (see Ref. [112]) AES sputter-depth profiles (blue dots) of a) an as-prepared multilayer and b) after diffusion annealing at 460 °C for three weeks. The AES intensity-depth profiles are described by the convolution (green line) of an MRI depth resolution function with a step profile with sharp interfaces as genuine concentration-depth profile (red line) in a). The following MRI parameters were applied: $\sigma = 1.46$ nm, $w_{\mathrm{Ge}} = 2.58$ nm, $w_{\mathrm{Si}} = 3.08$ nm, $R_{\mathrm{Ge}} = 1.69$, $R_{\mathrm{Si}} = 1.40$, $L_{\mathrm{Ge}} = 120$ nm, $L_{\mathrm{Si}} = 100$ nm and $\dot{z}_{\mathrm{Ge}}/\dot{z}_{\mathrm{Si}} = 1.3$. The values for the effective attenuation lengths and the explanation of the symbols have been given in Ref. [112]. For the diffusion annealed specimen b), the measured AES intensity-depth profiles were fitted by the convolution (green line in b) of the same MRI depth resolution function as in a) with a genuine concentration profile (red line in b) given by the solution of Fick's second law. The initial (stepped) concentration-depth profile has been indicated in b) by the black dashed line.

tendency exists in a-$Si_{1-x}Ge_x$ solid solutions (and in the liquid phase [125]).[4] In the present study, a temperature independent interaction parameter is used: $\Omega = -4.03$ kJ/mol (cf. Ref. [121]). The precise value of the interaction parameter has only a small effect on the determined self-diffusion coefficients of Si and Ge in pure a-Si and in the a-$Si_{0.52}Ge_{0.48}$ solid solution (see appendix 3.A).

Now, the fitting parameters in the forward calculation approach (see Ref. [112]) for the determination of the genuine concentration-depth profile of the diffusion annealed specimens are the self-diffusion coefficients in the pure components, $D^*_{\text{Si in Si}}$ and $D^*_{\text{Ge in Ge}}$, the asymmetry factors, m_{Si} and m_{Ge}, and the locations of the initial Si/$Si_{0.52}Ge_{0.48}$ interfaces. To reduce the number of fitting parameters, the self-diffusion coefficients of Si and Ge in a-$Si_{1-x}Ge_x$ solid solutions have been assumed to be the same, which holds for crystalline $Si_{1-x}Ge_x$ solid solutions in the investigated concentration and temperature range. The ratio of the Si self-diffusion coefficient in pure c-Si [127] and the impurity diffusion coefficient of Ge in pure c-Si [105] is calculated to be 1.9 at 450 °C and the ratio of the Ge self-diffusion coefficient in c-$Si_{0.55}Ge_{0.45}$ [105] and the Si self-diffusion coefficient in c-$Si_{0.55}Ge_{0.45}$ [105] is calculated to be 2.7. These differences are similar to the experimental accuracy (see also the discussion about the thermodynamic factor in the appendix 3.A).[5] In the amorphous phase the difference of the self-diffusion coefficients of Si or Ge in amorphous $Si_{1-x}Ge_x$ solid solutions is excpected to be (even more) minor considering the diffusion mechanism in the amorphous phase (which is different as compared to that in the crystalline phase; see discussion in section 3.4). The self-diffusion coefficients of Si and Ge in Si and Ge are thus described according to (cf. Eq. 3.1):

$$D^*_{\text{Si in Si}} = D^*_{\text{Ge in Si}} = D^*_{\text{Ge in Ge}} \cdot \exp(-m_{\text{Ge}}) \tag{3.3a}$$

$$D^*_{\text{Ge in Ge}} = D^*_{\text{Si in Ge}} = D^*_{\text{Si in Si}} \cdot \exp(-m_{\text{Si}}) \tag{3.3b}$$

As a result, the number of independent fitting parameters describing the concentration dependence of the self-diffusion coefficients is reduced from four ($D^*_{\text{Ge in Ge}}$, $D^*_{\text{Si in Si}}$, m_{Ge} and m_{Si}) to two (e.g. $D^*_{\text{Si in Si}}$ and m_{Si}) as it holds (cf. Eq. 3.3):

$$\exp(-m_{\text{Si}}) = \frac{D^*_{\text{Ge in Ge}}}{D^*_{\text{Si in Si}}} = \exp(m_{\text{Ge}}). \tag{3.4}$$

[4] Note that for the liquid $Si_{1-x}Ge_x$ phase a demixing tendency has also been reported [126].

[5] Note that the assumption of similar self-diffusion coefficients of Si and Ge in crystalline $Si_{1-x}Ge_x$ solid solutions does not hold for larger Ge concentrations. The ratio of the Ge self-diffusion coefficient in pure c-Ge [128] and the Si impurity diffusion coefficient in pure c-Ge [129] is calculated to be 12.8.

On this basis, for a given set of numerical values for the fit parameters, the concentration-depth profile can be calculated by solving Fick's second law numerically using a fully implicit finite difference scheme [103]. This procedure has been incorporated in the fitting to the measured smeared concentration-depth profile.

The thus deduced self-diffusion coefficients of Si (equal to those of Ge; see above) in pure a-Si and in the a-$Si_{1-x}Ge_x$ solid solution for $x = 0.48$ are given in table 3.1. The self-diffusion coefficients of Si (or Ge) in the a-$Si_{0.52}Ge_{0.48}$ solid solution are about a factor of five larger than the self-diffusion coefficients of Si (or Ge) in pure a-Si. Using the data for the self-diffusion coefficients of Si (or Ge) in pure a-Si and in the a-$Si_{1-x}Ge_x$ solid solution for $x = 0.48$ given in table 3.1, the temperature dependence of $D^*_{\mathrm{Si\ in\ Si}}$ and $D^*_{\mathrm{Si\ in\ Si_{0.52}Ge_{0.48}}}$ can be described with Arrhenius equations with activation enthalpies, Q, of (1.9 ± 0.7) eV and (2.1 ± 1.2) eV and pre-exponential factors, D_0, of $4.0 \cdot 10^{-11}$ $\mathrm{m^2/s}$ (error: $\log D_0 = \pm\, 11.3$) and $1.9 \cdot 10^{-10}$ $\mathrm{m^2/s}$ (error: $\log D_0 = \pm\, 19.8$) for the a-$Si_{0.52}Ge_{0.48}$ solid solution and pure a-Si, respectively (see figure 3.4).

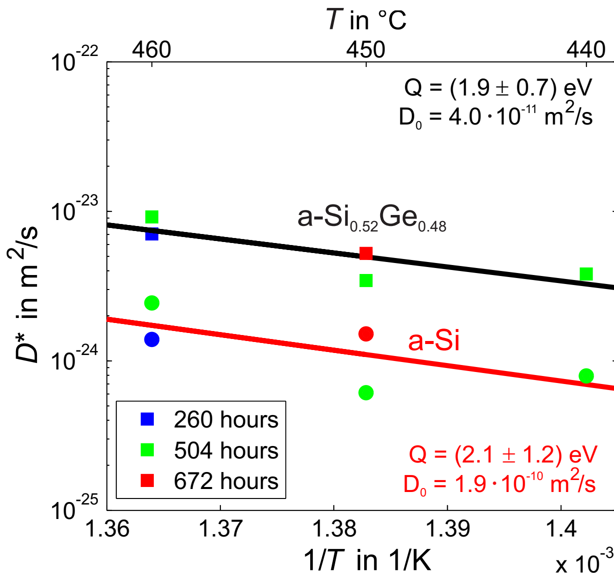

Figure 3.4: Arrhenius plot of the values determined for the self-diffusion coefficient of Si (or Ge) in pure a-Si and in the a-$Si_{1-x}Ge_x$ solid solution for $x = 0.48$.

Table 3.1: Si (or Ge) self-diffusion coefficients, D^*, in pure a-Si and a-$Si_{0.52}Ge_{0.48}$, the intrinsic diffusion coefficient, D, of Si (or Ge) in a-$Si_{0.52}Ge_{0.48}$ (all in units 10^{-24} m^2/s), and the asymmetry factor, m_{Si}, as determined by the MRI forward calculation approach.

temperature	440 °C	450 °C		460 °C	
time	506 h	504 h	672 h	260 h	504 h
$D^*_{\text{Si in a-Si}}$	0.8	0.6	1.5	1.4	2.4
$D^*_{\text{Si in a-Si}_{0.52}\text{Ge}_{0.48}}$	3.8	3.4	5.2	7.1	9.2
$D_{\text{Si in a-Si}_{0.52}\text{Ge}_{0.48}}$	5.9	5.3	8.0	10.8	14.0
m_{Si}	-3.3	-3.6	-2.6	-3.4	-2.8

3.4 Discussion

Within experimental error (the error of the fitted self-diffusion coefficients can be estimated at 80%, as accessed from the deviation of the data points from the fitted straight line in figure 3.4), no pronounced dependence of the self-diffusion coefficients of Si (or Ge) in a-Si or a-$Si_{0.52}Ge_{0.48}$ on the annealing time can be observed. Therefore, a possible structural relaxation in the amorphous specimen [130] has a negligible effect on the self-diffusion coefficients. Indeed structural relaxation in a-Si has been found to occur at the annealing temperatures used in this study at a time scale of only a few hours [31, 131], whereas annealing times of hundreds of hours apply to this study.

The determined values for the self-diffusion coefficient of Si (or Ge) in pure a-Si and in a-$Si_{0.52}Ge_{0.48}$ are about *ten orders of magnitude larger* than the reported values for the self-diffusion coefficient of Si (or Ge) in the corresponding *crystalline* phases (see figure 3.5a and figure 3.5b, respectively). A considerably higher *chemical* diffusion coefficient in the amorphous phase, as compared to the crystalline phase, has been observed in previous studies [29–31, 132].

Extrapolated self-diffusion coefficients of Si (or Ge) in pure a-Ge are in the range of $\approx 1 \cdot 10^{-23}$ m^2/s - $8 \cdot 10^{-23}$ m^2/s in the temperature range studied. However, in contrast to the self-diffusion coefficients of Si (or Ge) in pure a-Si or in a-$Si_{0.52}Ge_{0.48}$, the self-diffusion coefficients of Si (or Ge) in pure a-Ge strongly depend on the chosen value for the interaction parameter, Ω (see figure 3.6 and figure 3.7).

The here experimentally established activation enthalpy for Si (or Ge) self-diffusion in pure a-Si is in between the activation enthalpies found in

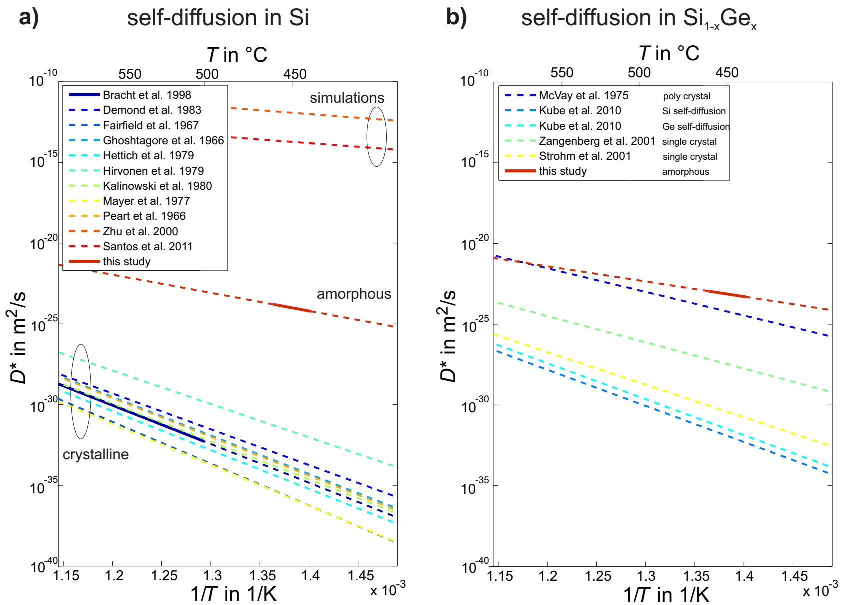

Figure 3.5: a) Comparison of experimentally determined Si self-diffusion coefficients in amorphous and crystalline pure Si. Literature data are taken from Refs. [127, 133–140]. Simulations for Si self-diffusion in a-Si [141] and liquid Si [142] are shown as well. b) Comparison of Ge self-diffusion coefficients in crystalline $Si_{0.50}Ge_{0.50}$ solid solutions as reported in the literature [105, 143–145] with self-diffusion coefficients of Si (or Ge) in the a-$Si_{0.52}Ge_{0.48}$ solid solution, as determined in this study. The temperature ranges in which the experiments were performed have been indicated by solid lines. Extrapolations towards temperatures beyond the experimental temperature ranges have been indicated with dashed lines.

simulations applying the activation relaxation technique, yielding an activation enthalpy of 3 eV [146], and by molecular dynamics simulations for Si self-diffusion in an amorphous continuous random network [141] or in liquid Si [142], yielding an activation enthalpy of about 1 eV. The deviation in the activation enthalpy determined by molecular dynamics simulations, as compared to the activation enthalpy obtained according to the activation relaxation technique, might be explained by the uncertainty in the applied empirical atomic potential for amorphous structures, as indicated in Ref. [147]. The predicted Si self-diffusion coefficients of the molecular dynamics stud-

ies [141, 142] are ten orders of magnitude *larger* than the Si self-diffusion coefficients determined experimentally in this study (see figure 3.5a), indicating that the high temperatures ($> 627\,^{\circ}$C) and short annealing times (< 4 ns) applied in the molecular dynamics simulations might not allow the extrapolation to experimentally realistic annealing conditions.

The self-diffusion coefficients of Si (or Ge) of the amorphous phase being strikingly larger than those of the crystalline phase, suggests that, despite the prevailing similar covalent bonding in amorphous and crystalline $Si_{1-x}Ge_x$ solid solutions, a very different diffusion mechanism operates in a-$Si_{1-x}Ge_x$ solid solutions. The structure of a-Si and a-Ge can be described as a continuous random network of covalently bonded atoms [16], which consists of mainly fourfold coordinated Si or Ge atoms with distorted, as compared to the crystalline structure, bond angles.[6] The occurrence of such distorted coordination polyhedra is associated with the presence of excess free volume involving a smaller (according to Ref. [68] and Ref. [69]: 1.8 % and $< 4\%$ for a-Si and a-Ge, respectively) volume density for the amorphous phase as compared to the corresponding crystalline phase. This excess free volume can facilitate diffusion in the amorphous phase and thus can explain the pronounced larger diffusion coefficients of the amorphous phase as compared to those of the crystalline phase. The experimentally determined activation enthalpy for Si (or Ge) self-diffusion in pure a-Si (2.1 eV) and $Si_{0.52}Ge_{0.48}$ (1.9 eV) is distinctly smaller than the vacancy formation enthalpy in pure c-Si and pure c-Ge (3.6 eV [148] and 2.4 eV [149], respectively). Hence, the formation of equilibrium point defects, such as "vacancies", cannot play a major role for self-diffusion of Si (or Ge) in a-$Si_{1-x}Ge_x$: the activation enthalpy for diffusion in the amorphous phase can be interpreted as an activation enthalpy of migration [18, 150]. The activation enthalpies for the migration of a neutral vacancy in single crystalline Si and Ge are small (0.45 eV [151] and 0.4 eV [149], respectively). Therefore, it is finally suggested that in the relaxed amorphous phase several atoms move in a cooperative way during a diffusion event. Such cooperative movement of atoms has indeed been discussed as a possible diffusion mechanism for amorphous metallic glasses [54, 55]. The needed cooperative movement of several atoms in a diffusion event implies that the free volume in the amorphous phase is distributed over the whole system and that single pieces of free volume do not allow the jump of a single atom: several atoms need to change their position during a diffusion event to rearrange the structure and cause a net atomic displacement [57, 152]. This process is associated with a larger activation enthalpy than that of a single atomic jump.

[6] The detailed structure of a-Si and a-Ge is still debated [17].

The cooperative movement of several atoms has also been shown by simulation of Si self-diffusion in amorphous Si [141, 146, 153, 154]. During one diffusion event typically about 2-4 atoms change their position by more than 0.5 Å and about 30 atoms by more than 0.1 Å [146]. However, contrary to the wide spread cooperative movement of atoms in amorphous metallic glasses [54, 55], in which groups of more than ten atoms participate in a chain-like displacement during one diffusion event [56], in amorphous Si the main displacements of atoms are mainly limited to the nearest neighbors of the diffusing atom [146, 154]. The more localized cooperative movement of atoms in amorphous Si, as compared to the atomic movement in amorphous metallic glasses, can be attributed to the covalent bonding of Si, which can hinder wide spread atomic displacements.

The obtained value for the activation enthalpy for Si (or Ge) self-diffusion in pure a-Si is slightly larger than that in the a-$Si_{0.52}Ge_{0.48}$ solid solution (2.1 eV vs. 1.9 eV) (see figure 3.4). Since the estimated atomic packing density of a-Si (28 %) is smaller than for a-Ge (32 %)[7] a smaller activation enthalpy might be expected for pure a-Si, as compared to a-$Si_{0.52}Ge_{0.48}$, which opposes the experimentally determined trend. Alternatively, it might be suggested that the difference in Si-Si and Ge-Ge covalent bond strength is the origin of the observed concentration-dependence of the activation enthalpy: the Ge-Ge bond is weaker than the Si-Si bond (bond energies of 261 kJ/mol [156] vs. 320 kJ/mol [156], respectively). Thus, the movement of atoms in the cooperative process described above for a diffusion event can be associated with a lower effective enthalpy of migration for larger Ge content.

3.5 Conclusions

- Interdiffusion in amorphous Si/$Si_{0.52}Ge_{0.48}$ specimens requires analysis of diffusion lengths on the nanometer scale in order to avoid crystallization of the amorphous phase. This has been shown to be possible by Auger electron spectroscopy sputter-depth profiling in combination with the forward calculation approach on the basis of the Mixing-Roughness-Information depth model. Thus concentration-depth profiles of multilayered amorphous Si/$Si_{0.52}Ge_{0.48}$ specimens, before and after annealing, could be determined directly.

- The self-diffusion coefficients of Si and Ge in the amorphous phases are about ten orders of magnitude larger than in the corresponding crystalline phases, which is ascribed to the significant amount of excess free volume inherent to the amorphous structure.

- The activation enthalpy for Si (or Ge) self-diffusion in the amorphous phase indicates a cooperative movement of several atoms for a single diffusion event.
- The Si (or Ge) self-diffusion coefficient is strongly concentration dependent. Si (or Ge) self-diffusion in pure a-Si is about a factor of five slower than Si (or Ge) self-diffusion in the a-$Si_{0.52}Ge_{0.48}$ solid solution. This effect may be related to an (overall) decrease of covalent bond strength with increasing Ge content.

Acknowledgments

The authors would like to thank Dr. E. Bischoff and Dipl.-Ing. P. Kopold for TEM investigations and W.-D. Lang for TEM specimen preparation (all with MPI-IS).

Appendix 3.A Influence of the thermodynamic factor on the deduced self- and intrinsic diffusion coefficients and the activation enthalpy

Since thermodynamic data for *amorphous* $Si_{1-x}Ge_x$ solid solutions are rare [121], and the mixing tendency in the *amorphous* phase [30, 120, 121] contrasts with the demixing tendency for *crystalline* $Si_{1-x}Ge_x$ solid solutions [104, 119, 122–124], it appears appropriate to investigate the influence of the adopted value of the interaction parameter, Ω, on the values for the intrinsic and self-diffusion coefficients obtained by fitting. The fitting procedure for the determination of the self-diffusion coefficients from the measured AES intensity-depth profiles has been outlined in section 3.3.2. The self-diffusion coefficient of Si (or Ge) in pure a-Si and the asymmetry factor, m_{Si}, are now used as the only fitting parameters.[8] For each subsequent fit a different value for the interaction parameter, Ω, in the range of $-8.03\,\mathrm{kJ/mol}$ to $2.03\,\mathrm{kJ/mol}$, has been used.

The deduced *intrinsic diffusion* coefficients of Si (or Ge) of the specimen annealed at 440 °C for 506 h, using different values of Ω are shown in figure 3.6. While a change of the interaction parameter has no significant effect on the intrinsic diffusion coefficient in the experimentally accessible concentration range (i.e. $0 \leq x \leq 0.48$), a distinct effect can be observed in the concentration range of $0.48 < x \leq 1$.

The maximum absolute differences of the deduced *self-diffusion* coefficient (for $\Omega = 2\,\mathrm{kJ/mol}, 1\,\mathrm{kJ/mol}, -1\,\mathrm{kJ/mol}, -8\,\mathrm{kJ/mol}$) and the self-diffusion coefficient obtained with $\Omega = -4.03\mathrm{kJ/mol}$ are shown in figure 3.7. It follows that the variation of Ω around the only reported value of $-4.03\,\mathrm{kJ/mol}$ [121] results in a change of the Si (or Ge) self-diffusion coefficients in pure a-Si and in a-$Si_{0.52}Ge_{0.48}$ of less than 28 % and 86 %, respectively. (Note that the change of the (extrapolated) self-diffusion coefficient of Si (or Ge) in pure a-Ge (not investigated in this work) is up to 283 %).

A variation of the interaction parameter, Ω, also influences the deduced *activation enthalpy* for Si (or Ge) self-diffusion in pure a-Si and in a-$Si_{0.52}Ge_{0.48}$. For Si (or Ge) self-diffusion in pure a-Si an up to 27 % higher activation enthalpy is obtained for interaction parameters of $\Omega \neq -4.03\,\mathrm{kJ/mol}$ (i.e $\Omega = 2\,\mathrm{kJ/mol}, 1\,\mathrm{kJ/mol}, -1\,\mathrm{kJ/mol}, -8\,\mathrm{kJ/mol}$), while in a-$Si_{0.52}Ge_{0.48}$ the activation enthalpy can be up to 26 % smaller for interaction parameters of $\Omega \neq -4.03\,\mathrm{kJ/mol}$ (i.e $\Omega = 2\,\mathrm{kJ/mol}, 1\,\mathrm{kJ/mol}, -1\,\mathrm{kJ/mol}, -8\,\mathrm{kJ/mol}$).

[8] The locations of the initial interfaces have been adopted from the fitting procedure applying an interaction parameter of $\Omega = -4.03\,\mathrm{kJ/mol}$ and have not been fitted during the analysis described in this section.

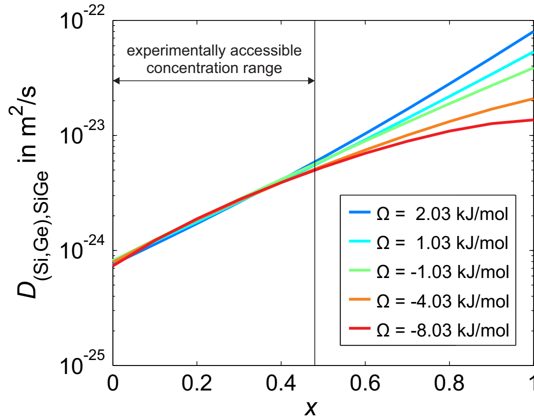

Figure 3.6: Intrinsic diffusion coefficients, D,of Si (or Ge) in a-$Si_{1-x}Ge_x$ as a function of the Ge concentration, x, as deduced from the measured AES intensity-depth profiles using different interaction parameters, Ω. A variation of Ω between -8.03kJ/mol to 2.03kJ/mol has only a minor effect on the deduced intrinsic diffusion coefficients of Si (or Ge) in the experimentally accessible concentration range of $0 \leq x \leq 0.48$.

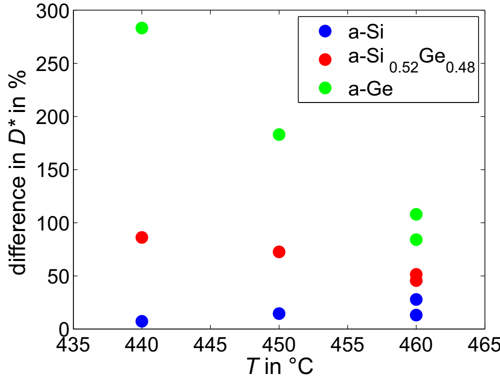

Figure 3.7: Maximum absolute difference of the deduced self-diffusion coefficient of Si (or Ge) in pure a-Si, a-$Si_{0.52}Ge_{0.48}$ solid solution and pure a-Ge as obtained for interaction parameters $\Omega \neq -4.03$ kJ/mol (i.e $\Omega = 2$ kJ/mol, 1 kJ/mol, -1 kJ/mol, -8 kJ/mol) with the self-diffusion coefficient of Si (or Ge) in the corresponding phase as obtained with an interaction parameter of $\Omega = -4.03$ kJ/mol (used in this study) as a function of annealing temperature, T.

Chapter 4

Interdiffusion in epitaxial, single-crystalline Au/Ag thin films studied by Auger electron spectroscopy sputter-depth profiling and positron annihilation

Martin A. Noah[1], David Flötotto[1], Zumin Wang[1,2], Markus Reiner[3], Christoph Hugenschmidt[3] and Eric J. Mittemeijer[1,4]

[1] *Max Planck Institute for Intelligent Systems (formerly Max Planck Institute for Metals Research), Heisenbergstr. 3, D-70569 Stuttgart, Germany*

[2] *School of Materials Science and Engineering, Tianjin University, Tianjin 300052, China*

[3] *Physics Department E21 and Heinz Maier-Leibniz Zentrum (MLZ), Technische Universität München, Lichtenbergstr. 1, 85748 Garching, Germany*

[4] *Institute for Materials Science, University of Stuttgart, Heisenbergstr. 3, D-70569 Stuttgart, Germany*

Abstract

Interdiffusion in epitaxial, single-crystalline Au/Ag bilayered thin films on Si (0 0 1) substrates was investigated by Auger electron spectroscopy (AES) sputter-depth profiling and by *in-situ* positron annihilation Doppler broadening spectroscopy (DBS). By the combination of these techniques identification of the role of vacancy sources and sinks on interdiffusion in the Au/Ag films was possible. It was found that with precise knowledge of the concentration-dependent self-diffusion and impurity diffusion coefficients a distinction between the Darken-Manning treatment and Nernst-Planck treatment can be made, which is not possible on the basis of the determined concentration-depth profiles alone.

4.1 Introduction

Interdiffusion in crystalline metallic diffusion couples is generally controlled by the vacancy mechanism [44]. The equilibrium vacancy concentrations at a given temperature and pressure of the components are generally different [38, 39], which can cause considerably different atomic mobilities of the components. As a consequence, during interdiffusion the difference in the atomic mobilities of the components causes a net flux of vacancies. If the number of active vacancy sources and sinks is high, the equilibrium vacancy concentration can be maintained (e.g by positive and negative climb of dislocation parts of edge character). As a result, the initial interface of the bilayer shifts in the laboratory frame of reference (Kirkendall shift). The developing concentration-depth profiles can then be described with a concentration-dependent chemical diffusion coefficient, applying the Darken-Manning treatment [45, 59].

At early stages of interdiffusion in thin films with a small amount of (line or planar) defects, such as dislocations or grain boundaries, the distance between vacancy sources and sinks is larger than the diffusion length. As a result, the equilibrium vacancy concentration-depth *profile* cannot be maintained during interdiffusion. In the special case of no active vacancy sources and sinks, the Nernst-Planck treatment [50] (also called Nazarov-Gurov treatment [46–49]), which was originally derived for ambipolar diffusion in ionic materials, can then be used to describe the concentration dependence of the chemical diffusion coefficient.

The effect of vacancy sources and sinks is also important from a technological point of view. In the absence of vacancy sources and sinks the difference in atomic fluxes of the components causes a supersaturation of vacancies in the sublayer composed (mainly) of the faster component and at large vacancy supersaturation pore formation can occur [51]. These pores can either be undesirable, i.e. in solder joints where the mechanical stability is reduced by the pores [4], or desirable as for the fabrication of hollow nanoparticles [157, 158].

Despite the above described pronounced scientific and technological interests, the influence of vacancy sources and sinks on the diffusion kinetics has been poorly investigated. Corresponding experimental investigations are very rare and are limited to the study of the effects of vacancies frozen-in due to the preparation method of the thin films [159] and/or the injection of vacancies from the surface and interface(s) [160, 161]. Only a few theoretical attempts have been presented to model the influence of vacancy sources and sinks on the interdiffusion kinetics [162–165].

The fully miscible Ag/Au [166] system appears to be an ideal candidate

for the investigation of the effect of vacancy sources and sinks on interdiffusion. Firstly, the interdiffusion is asymmetric [167–170]: the diffusion of Ag in Au [171, 172] is considerably faster than the diffusion of Au in Ag [173, 174]. Secondly, the lattice parameters of Ag and Au are very similar (difference of 0.18 % at room temperature [73]) allowing the preparation of single-crystalline bilayers practically without misfit dislocations at the Au/Ag interface; such misfit dislocations could serve as vacancy sources and sinks.

In this study the effect of vacancy sources and sinks on interdiffusion in epitaxial single-crystalline Au/Ag bilayers on Si (0 0 1) substrates has been investigated by (i) the *ex-situ* determination of the chemical concentration-depth profile by Auger electron spectroscopy sputter-depth profiling and (ii) by the *in-situ* determination of the defect concentration-depth profile by positron annihilation Doppler broadening spectroscopy.

4.2 Experimental procedure

4.2.1 Specimen preparation

Epitaxial Au/Ag bilayer thin films were prepared in a customised ultrahigh vacuum (UHV) system (base pressure $< 3 \cdot 10^{-8}$ Pa), equipped with high temperature effusion cells for thermal evaporation of pure Ag (> 99.995 wt.%) and pure Au (> 99.999 wt.%) (both from an Al_2O_3 crucible) and a high temperature cracker cell for the generation of atomic hydrogen.

Si (0 0 1) wafer substrates (boron doped; with a resistivity of 1-10 Ωcm, a miscut < 0.1° and dimensions of 13.9 mm × 13.9 mm) were ultrasonically cleaned successively in aceton and isopropanol, rinsed in methanol and thoroughly cleaned by a programmed laser heat treatment up to a maximum temperature of 1100 °C for 80 s in UHV. On the thus prepared contamination free well-ordered Si(0 0 1)-2 × 1 surfaces (as verified by *in-situ* XPS and STM analysis performed in this project) epitaxial Au/Ag bilayers were deposited in successive steps as follows. Firstly, about 0.2 nm (nominal thickness) of Ag was deposited with a deposition rate of 0.2 nm/min on the clean Si(0 0 1)-2 × 1 surface at 160 °C and subsequently annealed for 60 min. This treatment led to a high density of Ag(0 0 1) islands on the surface. Secondly, the specimen was cooled down to room temperature and exposed to atomic hydrogen for 10 min by introducing H_2-gas (0.002 sccm with a purity of 99.99999 vol.%) through the high temperature cracker cell operating at a temperature of > 1600 °C. The thus prepared hydrogen saturated surface with a high density of Ag(0 0 1) islands served as nucleation layer during the subsequent deposition of a continuous 200 nm thick Ag layer with a depos-

ition rate of 31 nm/min at room temperature. The Ag film was annealed for 90 min at a temperature of about 160 °C. Finally, after cooling the specimen down to room temperature, a 150 nm thick Au layer was deposited with a deposition rate of 1.6 nm/min. Some specimens (specimen series B) were then covered with a 20 nm thick protective Si_3N_4 surface layer, as deposited by reactive magnetron sputtering of pure Si (99.999 wt.%) at a nitrogen partial pressure of $6.1 \cdot 10^{-4}$ mbar. It was shown experimentally that the protective Si_3N_4 surface layer had no influence on the determined impurity diffusion coefficients.

The thus prepared specimens were cut into smaller pieces and encapsulated in Ar filled quartz ampoules for the interdiffusion study. The diffusion annealing was performed in a salt bath for annealing times ranging from 1 h up to 3 weeks in a temperature range from 240 °C up to 350 °C.

4.2.2 Microstructural characterisation

The texture of the epitaxial Au/Ag bilayers was investigated by X-ray diffraction (XRD) $\{1\,1\,1\}$ pole-figure measurements ($2\theta = 44.566°$, $\Delta\phi = \Delta\psi = 1°$, where ϕ is the rotation angle around the specimen surface normal and ψ is the angle between the diffraction vector and the specimen-surface normal) in a Philips MRD Pro diffractometer, equipped with a secondary monochromator and employing Co K_α radiation ($\lambda = 1.78897$ Å). In addition, high resolution $2\Theta - \omega$ scans and rocking curves (step size = 0.005°) were measured in a Bruker D8 Discover diffractometer, equipped with a Göbel mirror, a two bounce Ge(2 2 0) crystal, a detector slit of 0.2 mm and employing monochromatic Cu K_α radiation ($\lambda = 1.540598$ Å) [175].

The surface morphology of Ag single layers and Au/Ag bilayers was analysed by a MultiMode atomic force microscope (AFM) from Bruker, equipped with a Si tip (tip radius < 10 nm) and operated in tapping mode.

4.2.3 Auger electron spectroscopy (AES) sputter-depth profiling

AES sputter-depth profiling of the as-prepared and diffusion annealed specimens was conducted with a JEOL JAMP-7830F AES system equipped with a hemispherical analyser as well as a field emission electron gun operating at an acceleration voltage of 10 kV and a beam current of 10 nA (see Ref. [112] for details). Sputter-depth profiling was performed with a focused 1 keV Ar^+ ion beam (rastering over the specimen surface) in an intermittent mode with sputter steps of 20 s - 60 s (corresponding to 1.5 nm - 4.6 nm for Ag and 1.3 nm - 4.0 nm for Au). In order to avoid ion channelling along low indexed lattice planes, an offset of $> 7°$ between the ion-gun and

a [1 1 1] direction[1] was chosen. After each sputter step, spectra of the Ag_{NVV} (kinetic energy = 80 eV), Au_{NVV}(69 eV), Si_{LMM}(92 eV), Ag_{MNN} (351 eV), O_{KLL}(503 eV), Si_{KLL}(1610 eV) and Au_{MNN} (2024 eV) Auger transitions were recorded with an energy step size of 1 eV while scanning the primary electron beam over an area of 1 µm × 1 µm. The measured AES spectra were differentiated by a 7 point-algorithm and fitted with a linear least squares fitting procedure, or in the case of overlapping AES spectra, by applying the target factor analysis [114]. In order to account for sputter-induced alterations, such as ion bombardment induced atomic mixing and surface roughening as well as for the intrinsic specimen surface and interface roughness in the measured intensity-depth profiles, an (extended) Mixing-Roughness-Information depth (MRI) model has been applied [85, 112]. Thereby, the genuine concentration-depth profile was determined in a forward calculation approach with a depth resolution in the nanometre range (see Ref. [112] for details).

4.2.4 Positron annihilation Doppler broadening spectroscopy (DBS)

The measurement of the Doppler broadening of the positron annihilation line is one of the standard techniques for the investigation of defects such as vacancies, pores or grain boundaries, by exposing the specimen to positrons [176, 177]. The annihilation of a positron with an electron in the solid generates two collinear γ-photons with a total energy of 1022 keV. The energies of the two γ-photons are Doppler shifted due to the momentum of the annihilating electron-positron pair. Compared to the momentum of an electron bound in the solid, the momentum of thermalised positrons is negligible small. The mentioned Doppler shift is thereby generally larger for positron annihilation with a core electron (high momentum), than with a valence electron (low momentum). In a perfect crystal, positrons annihilate with both core and valence electrons, while in a defective solid, positrons can be trapped in open volume defects due to their positive charge and annihilate preferably with valence electrons. As a result, the Doppler broadening of the positron-annihilation line is smaller in a defective crystal, as compared to a perfect crystal. A measure for the broadening of the positron-annihilation line at 511 keV is the so-called S-parameter. It is defined as the ratio of the central area below the positron-annihilation peak at the peak maximum and the total area of the positron-annihilation peak [176].

Positrons implanted into a solid thermalise rapidly. The resulting depth distribution can be described with a Makhovian function [177], which de-

[1] In the plane defined by the specimen surface normal, [0 0 1], and the [1 1 1] direction.

pends on the material and the positron-implantation energy. By taking into account the broadening of the positron-implantation profile by diffusion of thermalised positrons, the depth of preferred positron annihilation can be determined. Therefore, depth dependent information about the defect concentration in thin film systems can be obtained by varying the positron-implantation energy and thus changing the depth of preferred positron annihilation.

In-situ positron annihilation Doppler broadening spectroscopy during diffusion annealing of epitaxial Au/Ag bilayered thin films was performed at the positron source NEPOMUC (NEutron induced POsitron source MUniCh) at the research reactor FRM II of the Technical University of Munich [178, 179]. The positron-annihilation peak around 511 keV is usually recorded by four Ge detectors as a function of the positron-implantation energy. For the present study the detector with the largest signal to noise ratio was used. The positron-implantation energy was varied in the range of 0.5 keV - 29 keV with a measurement time of 60 s per step. The as-prepared specimen was mounted on a heatable specimen holder, while constantly measuring the temperature with a pyrometer [180]. After two successive measurements at room temperature, the specimen was heated within ≈ 3 min from room temperature to 330 °C and then annealed at this temperature for 10 h 18 min. In order to reduce the measurement time during diffusion annealing, the range of the used positron-implantation energies was limited to obtain preferred positron annihilation near the Au/Ag interface region, i.e. to the range of 3 keV to 13 keV (in steps of 0.5 keV). An additional measurement point at a positron-implantation energy of 29 keV, which corresponds to preferred annihilation in the Si substrate, served as an internal reference measurement. Starting at a positron-implantation energy of 3 keV, the positron-annihilation line was recorded. The positron-implantation energy was then successively increased to the desired value and the positron-annihilation line was recorded for each set positron-implantation energy. After measuring the positron-annihilation line at a positron-implantation energy of 29 keV, the positron-implantation energy was reduced to 3 keV and the measurement cycle was run again for a total of 22 times. The S-parameter was determined from 30 energy channels (≈ 54 eV per channel) of the detector around the positron-annihilation peak at 511 keV. Two subsequent measurement cycles were averaged in order to increase the statistical significance of the data.

In order to assess the change of the S-parameter in the individual sublayers the VEPFIT program [181, 182] was applied. This program allows the modelling of the S-parameter as a function of the positron-implantation energy in a thin film system with sharp interfaces. Due to the broad positron-implantation profile in high-quality thin films with a small defect concen-

tration (see figure 4.8), the effect of diffusional broadening of the Au/Ag interface during diffusion annealing on the S-parameter is negligible and is thus neglected in the following evaluation.

The temperature dependent positron-diffusion length in the Si substrate ($L_{\mathrm{Si}}(330°\mathrm{C}) = 82$ nm) and the Ag layer ($L_{\mathrm{Ag}}(330°\mathrm{C}) = 37$ nm), were successively determined from reference measurements of a Si(0 0 1) substrate and an epitaxial, single Ag(0 0 1) layer on a Si(0 0 1) substrate. For the determination of the positron-diffusion length in the Ag single layer, the positronium fraction[2] was used in addition to the S-parameter. These diffusion lengths, $L_{\mathrm{Si}}(330\ °\mathrm{C})$ and $L_{\mathrm{Ag}}(330\ °\mathrm{C})$, the layer thicknesses (as determined by the deposition rate) and the S-parameter of the Si substrate (as determined from the first measurement during diffusion annealing) were kept constant during the fitting procedure applied to the measurements performed during diffusion annealing. The remaining fitting parameters thus are the S-parameters of the Au and Ag sublayers and the surface. The positron-diffusion length in the Au sublayer was fitted to 37 nm and was found to be constant during the entire isothermal annealing procedure. The predetermined (from the reference measurements; see above) S-parameter of the single Ag layer was used as starting value for the fitting procedure.

4.3 Results and Discussion

4.3.1 Microstructure

As revealed by the XRD {1 1 1} pole figure measurements, the preparation procedure, as described in section 4.2.1, results in the formation of epitaxial Au/Ag bilayers with a cube-on-cube orientation relationship with respect to the Si(0 0 1) substrate described by

$$\mathrm{Au}(0\,0\,1)\,||\,\mathrm{Ag}(0\,0\,1)\,||\,\mathrm{Si}(0\,0\,1);\ \mathrm{Au}[1\,1\,0]\,||\,\mathrm{Ag}[1\,1\,0]\,||\,\mathrm{Si}[1\,1\,0]. \qquad (4.1)$$

The film exhibits a very small ($<$ 1 vol.%) amount of twins on {1 1 1} planes inclined with respect to the (0 0 1) oriented surface, resulting in a {5 1 1} texture component [183] (see figure 4.1a). The pole figure indicates the presence of small angle grain boundaries (mosaicity). The presence of small angle grain boundaries was also evidenced by the broad $2\Theta - \omega$ scans (FWHM = 0.2°) and rocking curves (FWHM = 0.6°), as compared to the

[2] The positronium fraction corresponding to the annihilation of free o-Ps at the surface was determined from the energy spectrum of the annihilation radiation by evaluating the so-called valley-to-peak ratio (Valley region: 450 - 500 keV, peak region: 500 - 522 keV).

nominal instrumental resolution of about 0.03°. The average distance of the small angle grain boundaries is about 200 nm, as estimated from the perpendicularly aligned trenches observed in the AFM image (see figure 4.1b). These trenches run along the ⟨1 1 0⟩ directions and have a depth of 0.7 nm. The surface of the Au/Ag bilayers (see figure 4.1b), as well as of Ag single layers (not shown) is very smooth with a root mean squared roughness (RMS) of only 0.3 nm. Although a number of specimens with a rougher specimen surface (RMS of 2.2 nm) have been used, the influence of the different film morphologies on the determined impurity diffusion coefficients is small and thus has been neglected in the following discussion.

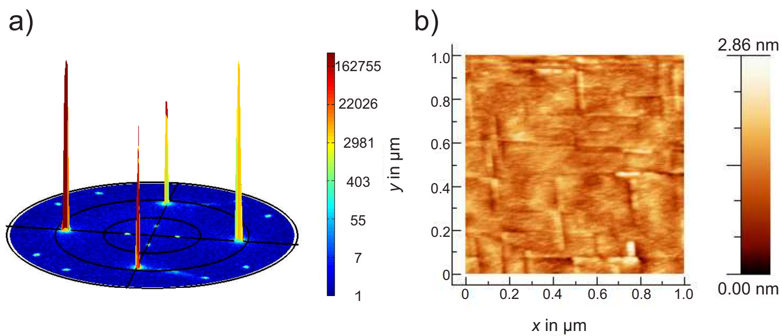

Figure 4.1: a) Ag+Au(111) pole figure of an Au/Ag bilayer prepared by thermal evaporation on a Si (0 0 1) substrate. Beside the pronounced Ag(111)/Au(111) poles, reflections with much smaller intensity of a very small volume fraction (< 1 vol.%) of twins can be observed. The intensity has been plotted in a logarithmic scale. b) AFM image of an Au/Ag bilayer revealing a smooth surface. The visible straight lines, which run along the ⟨1 1 0⟩ directions might belong to the dislocation network necessary to account for the observed mosaicity of the (0 0 1) crystallites.

Table 4.1: MRI parameters for roughness, σ, mixing, w, effective attenuation length in the respective pure component, λ [92], mean effective backscattering decay length, L, and backscattering correction factor, R [100]. The parameters σ, L and w were obtained from a fit to an as-prepared specimen assuming a step like concentration-depth profile. For the mixing parameters, w, the projected ion range, as estimated by SRIM [94] was used as a starting value. The ratio of the sputter rates is $\dot{z}_{\mathrm{Ag}}/\dot{z}_{\mathrm{Au}} = 1.2$.

σ	w_{Ag}	w_{Au}	$\lambda_{\mathrm{Ag}_{NVV}}$	$\lambda_{\mathrm{Ag}_{MNN}}$	$\lambda_{\mathrm{Au}_{NVV}}$	$\lambda_{\mathrm{Au}_{MNN}}$	L_{Ag}	L_{Au}	R_{Ag}	R_{Au}	R_{Si}
4.7 nm	2.86 nm	0.1 nm	0.39 nm	0.59 nm	0.43 nm	1.83 nm	50 nm	50 nm	1.85	1.97	1.32

4.3.2 Concentration-depth profiles

The measured AES intensity-depth profiles of the as-prepared Au/Ag bilayer (see figure 4.2a) can be described with a single set of MRI parameters presuming a sharp[3] Au/Ag interface (see table 4.1). The roughness parameter, σ, is not only comprised of the contributions of the surface and interface roughness, but also by the straggling of the mixing length [85]. Therefore, the value of the roughness parameter is larger than the measured value of the surface roughness by AFM. The large interface roughness dominates the sputter-induced smearing and thus other effects, such as ion-induced atomic mixing, are of smaller importance, which explains the small mixing parameter in Au. Taking for the values of the mixing parameters the values estimated for the projected ion ranges (from SRIM [94]), of $w_{\mathrm{Ag}} \approx w_{\mathrm{Au}} \approx 1.6$ nm, has only a minor effect on the fitted impurity diffusion coefficients.

Upon diffusion annealing the initially sharp Au/Ag interface broadens due to interdiffusion and asymmetric concentration-depth profiles develop (see figures 4.2b-c). The impurity diffusion coefficients have been determined in the present study from the measured sputter-depth profiles, by incorporating the following physical diffusion models in the MRI forward calculation approach (see Ref. [112] for details).

If the activity of vacancy sources and sinks is sufficient to maintain the equilibrium vacancy concentration-depth profile in the specimen upon interdiffusion, the chemical diffusion coefficient, $\widetilde{D}$, is given by the Darken equation [45], including the vacancy-wind factor, S_{wind}, as given by Manning [50, 59]

$$\widetilde{D}_{\mathrm{DM}} = (x_{\mathrm{Ag}} D_{\mathrm{Au}} + x_{\mathrm{Au}} D_{\mathrm{Ag}}) \cdot S_{\mathrm{wind}}, \tag{4.2}$$

[3] No intermixing of the Ag and Au layer during Au thin film deposition is to be expected due to the small kinetic energy of the Au atoms during thin film deposition by thermal evaporation and due to the negligible small volume diffusion of Au into the Ag sublayer at room temperature (cf. Ref. [184]).

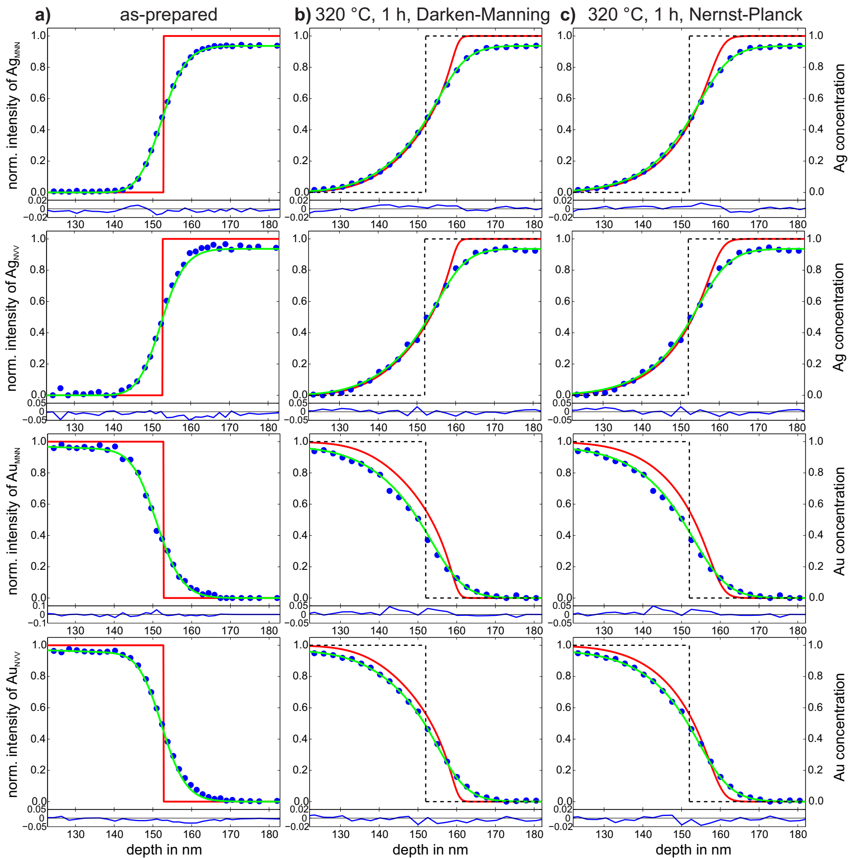

Figure 4.2: Measured AES sputter-depth profiles of different AES transitions (NVV and MNN) of a) an as-prepared Au/Ag bilayer and after diffusion annealing at 320 °C for one hour fitted by applying the MRI model and b) the Darken-Manning treatment or c) the Nernst-Planck treatment. The measured data (blue dots) has been plotted together with the genuine, unsmeared concentration-depth profile (red line) and the fitted normalised intensity-depth profile obtained by the convolution of the genuine, unsmeared concentration-depth profile with the depth-resolution function (green line). The difference between the calculated normalised intensity (green line) and the measured normalised intensity (blue dots) has been given at the bottom of each graphic as solid blue line. The black dotted line shows the initial concentration-depth profile with an assumed sharp interface. The used MRI parameters have been listed in table 4.1. Note that the normalised intensity in the Ag sublayer does not reach a value of 1 even in regions composed of pure Ag due to the backscattering effect (see Ref. [112] for details).

where x_{Ag} and x_{Au} are the molar fractions and D_{Ag} and D_{Au} are the intrinsic diffusion coefficients of Ag and Au, respectively. The vacancy-wind factor, S_{wind}, which describes correlation effects in a random alloy arising by a net flux of vacancies, can be approximately given by [50, 59]

$$S_{\mathrm{wind}} = 1 + \frac{1-f}{f} \cdot \frac{x_{\mathrm{Ag}} x_{\mathrm{Au}} (D^*_{\mathrm{Ag}} - D^*_{\mathrm{Au}})^2}{(x_{\mathrm{Ag}} D^*_{\mathrm{Ag}} + x_{\mathrm{Au}} D^*_{\mathrm{Au}}) \cdot (x_{\mathrm{Ag}} D^*_{\mathrm{Au}} + x_{\mathrm{Au}} D^*_{\mathrm{Ag}})}, \quad (4.3)$$

where f is the geometric correlation factor for the lattice type considered (i.e. 0.7815 for fcc) and D^*_{Ag} and D^*_{Au} are the concentration dependent self-diffusion coefficients of Ag and Au, respectively. Note that the description of Manning is only a valid approximation for similar exchange (jump) frequencies of the components [185]; consideration of the exact description of the vacancy-wind effect according to Ref. [186] is beyond the scope of this manuscript.

If no vacancy sources and sinks are active in the specimen, a non-equilibrium vacancy concentration-depth profile develops upon interdiffusion and the chemical diffusion coefficient is given by the Nernst-Planck equation [46–50]

$$\widetilde{D}_{\mathrm{NP}} = \frac{D_{\mathrm{Ag}} D_{\mathrm{Au}}}{x_{\mathrm{Ag}} D_{\mathrm{Ag}} + x_{\mathrm{Au}} D_{\mathrm{Au}}}. \quad (4.4)$$

The vacancy-wind factor for the Nernst-Planck equation is equal to one, according to the Manning approximation [187].

The concentration dependent intrinsic diffusion coefficients, D_{Ag} and D_{Au}, can be determined from the concentration dependent self-diffusion coefficients, D^*_{Ag} and D^*_{Au}, and the thermodynamic factor, Φ, according to

$$\begin{aligned} D_{\mathrm{Ag}}(x_{\mathrm{Au}}) &= D^*_{\mathrm{Ag}}(x_{\mathrm{Au}}) \cdot \Phi(x_{\mathrm{Au}}) \\ &= \left[D^*_{\mathrm{Ag\ in\ Ag}} \cdot \exp(-m_{\mathrm{Ag}} \cdot x_{\mathrm{Au}})\right] \cdot \Phi(x_{\mathrm{Au}}) \quad (4.5) \\ D_{\mathrm{Au}}(x_{\mathrm{Au}}) &= D^*_{\mathrm{Au}}(x_{\mathrm{Au}}) \cdot \Phi(x_{\mathrm{Au}}) \\ &= [D^*_{\mathrm{Au\ in\ Au}} \cdot \exp(-m_{\mathrm{Au}} \cdot (1 - x_{\mathrm{Au}}))] \cdot \Phi(x_{\mathrm{Au}}), \quad (4.6) \end{aligned}$$

where $D^*_{\mathrm{Ag\ in\ Ag}}$ is the self-diffusion coefficient of Ag in pure Ag and $D^*_{\mathrm{Au\ in\ Au}}$ the self-diffusion coefficient of Au in pure Au. m_{Ag} and m_{Au} are asymmetry parameters, which describe the concentration dependence of the self-diffusion coefficients of Ag and Au, respectively. The self-diffusion coefficients, $D^*_{\mathrm{Ag}}(1) = D^*_{\mathrm{Ag\ in\ Au}} = D^*_{\mathrm{Ag\ in\ Ag}} \cdot \exp(-m_{\mathrm{Ag}}) = D^*_{\mathrm{Ag}}(0) \cdot \exp(-m_{\mathrm{Ag}})$ and $D^*_{\mathrm{Au}}(0) = D^*_{\mathrm{Au\ in\ Ag}} = D^*_{\mathrm{Au\ in\ Au}} \cdot \exp(-m_{\mathrm{Au}}) = D^*_{\mathrm{Au}}(1) \cdot \exp(-m_{\mathrm{Au}})$, are the impurity diffusion coefficients of Ag in Au and of Au in Ag, respectively.

The here adopted exponential concentration dependence, which is usually applied to describe the concentration dependence of self-diffusion coefficient in dilute alloys (see e.g. p. 179 in Ref. [50]), is a good approximation for the whole concentration range in the system Ag/Au in the temperature range studied: the self-diffusion coefficients reported at higher temperatures (718 °C - 925 °C) [167], extrapolated to the annealing temperatures applied in this study (240 °C - 350 °C), can be well described by an exponential concentration dependence over the whole concentration range. The thermodynamic factor, Φ, for the Ag-Au system is faithfully approximated [188] by a regular solution model according to

$$\Phi = 1 - 2x_{\mathrm{Au}}(1 - x_{\mathrm{Au}})\frac{\Omega}{RT}, \tag{4.7}$$

where the concentration and temperature independent interaction parameter Ω equals to -15.6 kJ/mol [188], R is the universal gas constant and T the absolute temperature.

In order to reduce the number of fitting parameters in the MRI forward calculation approach, $D^*_{\mathrm{Ag\ in\ Ag}}$ and $D^*_{\mathrm{Au\ in\ Au}}$ (in the here investigated temperature range of 240 °C - 350 °C) are taken equal to the values determined by fitting the self-diffusion coefficients reported in different studies in an Arrhenius plot and extrapolated to the appropriate temperatures (see figure 4.3).

At temperatures close to the melting point divacancies form in Ag and contribute to Ag self-diffusion in Ag [53, 193, 201]. As a consequence, the reported Ag self-diffusion coefficients in the temperature range 274 °C - 950 °C can be described by a double Arrhenius equation, which considers the contribution of monovacancies (dominant at low temperatures) and divacancies (occurring at high temperatures) according to [53, 202]

$$D = D_{0,1V} \cdot \exp\left(-\frac{Q_{1V}}{RT}\right) + D_{0,2V} \cdot \exp\left(-\frac{Q_{2V}}{RT}\right), \tag{4.8}$$

where $D_{0,1V} = 5.44 \cdot 10^{-6}$ m^2/s, $D_{0,2V} = 3.96 \cdot 10^{-3}$ m^2/s, $Q_{1V} = 1.77$ eV and $Q_{2V} = 2.46$ eV are the temperature independent pre-exponential factors and temperature independent activation enthalpies of the monovacancy (1V) contribution and the divacancy (2V) contribution, respectively. The thus determined activation enthalpies for Ag self-diffusion via monovacancies and via divacancies are in very good agreement with literature values. The formation enthalpy of a monovacancy in Ag is $Q^F_{1V} = 1.11$ eV and the migration enthalpy of a monovacancy in Ag is $Q^M_{1V} = 0.66$ eV [203]. The binding enthalpy of a divacancy is $Q^B_{2V} = 0.38$ eV [204] and the migration enthalpy of a diva-

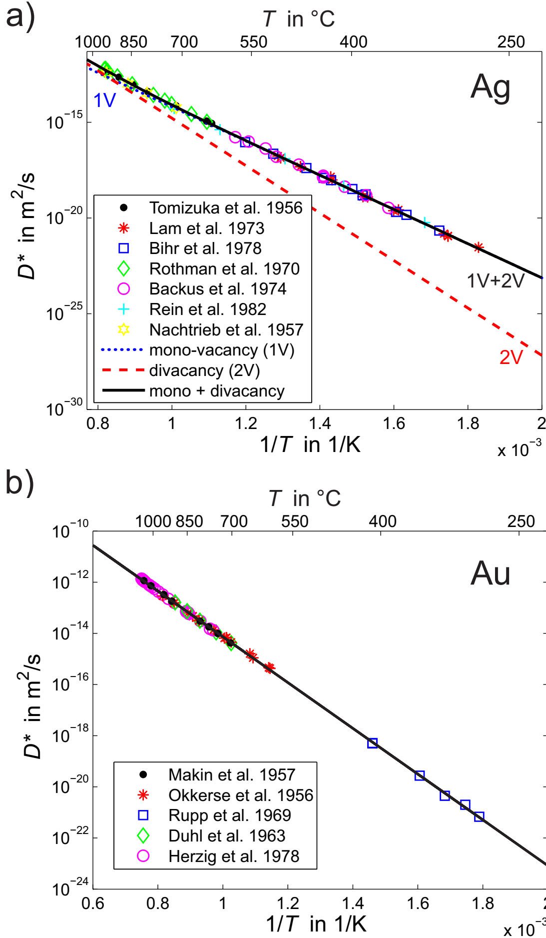

Figure 4.3: a) Ag self-diffusion coefficients in pure Ag (data taken from Refs. [189–195]). The monovacancy contribution has been described with a temperature independent activation enthalpy of $Q_{1V} = 1.77$ eV and a temperature independent pre-exponential factor of $D_{0,1V} = 5.44 \cdot 10^{-6}$ m^2/s. The divacancy contribution has been described with $Q_{2V} = 2.46$ eV and a pre-exponential factor of $D_{0,2V} = 3.96 \cdot 10^{-3}$ m^2/s. b) Au self-diffusion coefficients in pure Au (data taken from Refs. [196–200]) ($Q_{1V} = 1.77$ eV and $D_{0,1V} = 6.50 \cdot 10^{-6}$ m^2/s).

cancy is $Q_{2V}^{M} = 0.57$ eV [203]. These data lead to estimated activation enthalpies of $Q_{1V} = Q_{1V}^{F} + Q_{1V}^{M} = 1.77$ eV and $Q_{2V} = 2Q_{1V}^{F} - Q_{2V}^{B} + Q_{2V}^{M} = 2.41$ eV for Ag self-diffusion in pure Ag via monovacancies and divacancies, respectively. These estimated values very well agree with the above results obtained by fitting Eq. 4.8.

The divacancy contribution in Au is practically negligible [201] and the reported Au self-diffusion coefficients in the temperature range 286 °C-1060 °C (see figure 4.3b) can be described with a single Arrhenius equation with $Q_{1V} = 1.77$ eV, $D_{0,1V} = 6.50 \cdot 10^{-6}$ m^2/s. The literature values for the monovacancy formation enthalpy in Au of $Q_{1V}^{F} = 0.93$ eV and the monovacancy migration enthalpy of $Q_{1V}^{M} = 0.71$ eV [203] result in a slightly smaller activation enthalpy for Au self-diffusion in Au of $Q_{1V}^{\mathrm{Au}} = Q_{1V}^{F} + Q_{1V}^{M} =$ 1.64 eV.

Thus, the remaining fitting parameters in the MRI forward calculation approach for the determination of the genuine concentration-depth profile of the diffusion annealed specimens are the impurity diffusion coefficients (i.e. $D^{*}_{\mathrm{Ag\ in\ Au}} = D^{*}_{\mathrm{Ag\ in\ Ag}} \cdot \exp(-m_{\mathrm{Ag}})$ and $D^{*}_{\mathrm{Au\ in\ Ag}} = D^{*}_{\mathrm{Au\ in\ Au}} \cdot \exp(-m_{\mathrm{Au}})$) and the location of the initial Au/Ag interface.

On the basis of the presented set of equations, the genuine concentration-depth profile has been calculated applying the Darken-Manning (D-M) equation or the Nernst-Planck (N-P) equation by solving Fick's second law numerically using a fully implicit finite difference scheme [103] and fitting to the measured intensity-depth profile (see figure 4.2b-c). The concentration dependence of the intrinsic and chemical diffusion coefficients, applying the D-M or N-P treatment, at an annealing temperature of 320 °C, are shown in figure 4.4.

4.3.3 Self-diffusion/impurity diffusion coefficients

The measured intensity-depth profiles can be described by both the D-M as well as the N-P treatment and give very similar chemical diffusion coefficients (see figure 4.2b and figure 4.2c, respectively and section 4.3.4).

The impurity diffusion coefficients of *Ag in Au* (see table 4.3 and table 4.2), as obtained according to the D-M treatment and according to the N-P treatment, in the temperature range of 240 °C - 350 °C, are in good agreement with the impurity diffusion coefficients extrapolated from higher temperatures (670 °C - 1050 °C) [167, 171, 172] (see figure 4.5).

In contrast, the impurity diffusion coefficients of *Au in Ag*, determined according to the D-M or according to the N-P treatment, are considerably larger than the impurity diffusion coefficients extrapolated from higher tem-

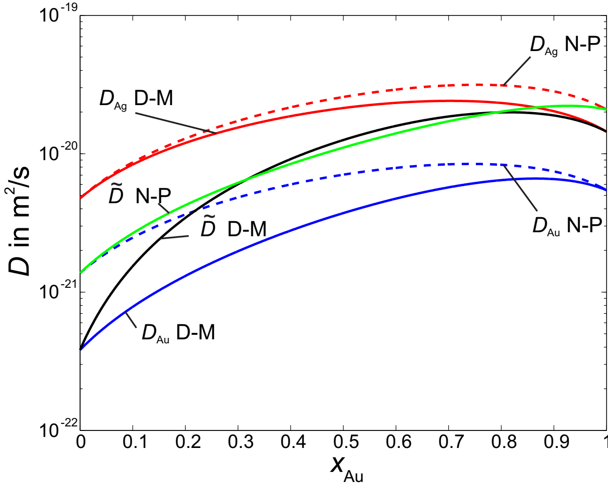

Figure 4.4: Determined intrinsic diffusion coefficients of Ag and Au after diffusion annealing at 320 °C for 1 h as well as the corresponding chemical diffusion coefficients applying the Darken-Manning (D-M) treatment and the Nernst-Planck (N-P) treatment. Due to the concentration dependence of the self-diffusion coefficients, the chemical diffusion coefficients calculated according to the Darken-Manning treatment and the Nernst-Planck treatment differ only relatively modestly, i.e $|(D_{\text{D-M}} - D_{\text{N-P}})/D_{\text{D-M}}| < 0.5$ for $x_{\text{Au}} \geq 10$ at.% .

peratures (718 °C - 925 °C) [167].[4] This deviation can be ascribed to the contribution of divacancies to the diffusion mechanism at higher annealing temperatures. As shown in figure 4.3 divacancies contribute to Ag self-diffusion in Ag at higher temperatures [53, 193, 201]. Thus one can expect that divacancies in the Ag matrix contribute also to the Au impurity diffusion in Ag. It follows that, as a consequence of the divacancy contribution at higher temperatures, the impurity diffusion coefficients of Au in Ag [167], extrapolated to lower temperatures, are too small. For Au self-diffusion in Au, the contribution of divacancies to the diffusion mechanism at higher temperatures is negligible small [171, 200] and the Au self-diffusion coefficients in

[4]Note that the determined impurity diffusion coefficients of Au in Ag are in very good agreement to the extrapolated impurity diffusion coefficients of Au in Ag from Ref. [173]. The latter study has not been considered here since the data reported in that work can be affected by the accidental contamination of the applied radio tracer with a long-lived radioactive impurity [167].

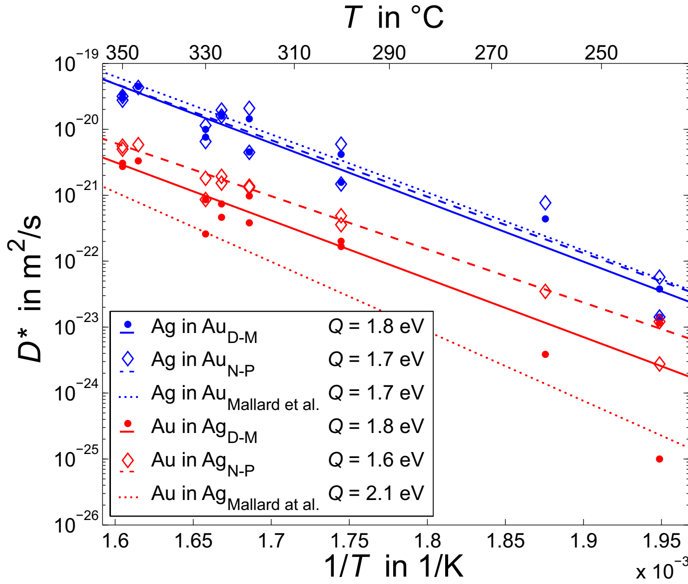

Figure 4.5: Determined impurity diffusion coefficients for Ag in Au, $D^*_{\text{Ag in Au}}$, and Au in Ag, $D^*_{\text{Au in Ag}}$, applying the Darken-Manning (D-M) treatment or the Nernst-Planck (N-P) treatment. Literature data from Ref. [167] extrapolated from higher temperatures are also shown. The activation enthalpies and pre-exponential factors have been listed in table 4.2.

Table 4.2: Activation enthalpy, Q, and pre-exponential factor, D_0, of the impurity diffusion coefficients of Ag in Au and Au in Ag applying the Darken-Manning (D-M) treatment or the Nernst-Planck (N-P) treatment, compared with literature values [167]. Note that due to the large error of the impurity diffusion coefficients of Au in Ag at low annealing temperatures, only data points obtained at $T > 260°\text{C}$ were used for the determination of Q and D_0. For the impurity diffusion coefficients of Ag in Au all data points were used.

		D-M	N-P	Mallard et al. [167]
Ag in Au	Q in eV	1.78 ± 0.12	1.70 ± 0.15	1.74
	D_0 in m^2/s	$1.03^{+10}_{-1} \cdot 10^{-5}$	$2.52^{+51}_{-3} \cdot 10^{-6}$	$7.20 \cdot 10^{-6}$
Au in Ag	Q in eV	1.75 ± 0.20	1.60 ± 0.09	2.09
	D_0 in m^2/s	$4.44^{+179}_{-5} \cdot 10^{-7}$	$4.88^{+20}_{-4} \cdot 10^{-8}$	$8.50 \cdot 10^{-5}$

Table 4.3: Impurity diffusion coefficients of Ag in Au and Au in Ag determined by applying the Darken-Manning (D-M) treatment or the Nernst-Planck (N-P) treatment in units of m^2/s. Specimens of series B have a larger surface roughness (RMS = 2.2 nm), as compared to specimens of series A (RMS = 0.3 nm). Specimen C was investigated by positron annihilation DBS.

specimen	T in °C	t in h	$D^*_{\text{Ag in Au}}$ D-M	$D^*_{\text{Au in Ag}}$ D-M	$D^*_{\text{Ag in Au}}$ N-P	$D^*_{\text{Au in Ag}}$ N-P
A	240	168	$3.99 \cdot 10^{-23}$	$1.00 \cdot 10^{-25}$	$5.74 \cdot 10^{-23}$	$2.76 \cdot 10^{-24}$
A	260	24	$4.38 \cdot 10^{-22}$	$3.86 \cdot 10^{-24}$	$7.67 \cdot 10^{-22}$	$3.48 \cdot 10^{-23}$
A	300	6	$4.18 \cdot 10^{-21}$	$1.66 \cdot 10^{-22}$	$5.96 \cdot 10^{-21}$	$4.88 \cdot 10^{-22}$
A	320	1	$1.44 \cdot 10^{-20}$	$3.82 \cdot 10^{-22}$	$2.08 \cdot 10^{-20}$	$1.37 \cdot 10^{-21}$
A	326	3	$1.58 \cdot 10^{-20}$	$4.63 \cdot 10^{-22}$	$1.59 \cdot 10^{-20}$	$1.53 \cdot 10^{-21}$
A	326	6	$1.68 \cdot 10^{-20}$	$7.38 \cdot 10^{-22}$	$1.96 \cdot 10^{-20}$	$1.94 \cdot 10^{-21}$
A	346	1	$4.47 \cdot 10^{-20}$	$3.32 \cdot 10^{-21}$	$4.31 \cdot 10^{-20}$	$5.84 \cdot 10^{-21}$
B	240	504	$1.42 \cdot 10^{-23}$	$1.16 \cdot 10^{-23}$	$1.42 \cdot 10^{-23}$	$1.21 \cdot 10^{-23}$
B	300	1	$1.57 \cdot 10^{-21}$	$2.00 \cdot 10^{-22}$	$1.48 \cdot 10^{-21}$	$3.57 \cdot 10^{-22}$
B	320	1	$4.53 \cdot 10^{-21}$	$9.74 \cdot 10^{-22}$	$4.48 \cdot 10^{-21}$	$1.32 \cdot 10^{-21}$
B	330	1	$9.96 \cdot 10^{-21}$	$8.56 \cdot 10^{-22}$	$1.14 \cdot 10^{-20}$	$1.81 \cdot 10^{-21}$
B	350	1	$3.43 \cdot 10^{-20}$	$3.05 \cdot 10^{-21}$	$3.16 \cdot 10^{-20}$	$5.56 \cdot 10^{-21}$
B	350	1	$2.99 \cdot 10^{-20}$	$2.73 \cdot 10^{-21}$	$2.77 \cdot 10^{-20}$	$5.00 \cdot 10^{-21}$
C	330	10.3	$7.58 \cdot 10^{-21}$	$2.59 \cdot 10^{-22}$	$6.53 \cdot 10^{-21}$	$8.61 \cdot 10^{-22}$

Au can be described with a single Arrhenius equation over the temperature range of 286 °C - 1060 °C (see figure 4.3b). Even at the melting temperature of Au the divacancy contribution to self-diffusion of Au in pure Au is only 20% [200], whereas it is assumed to be up to 45% [192] or even larger [205] for Ag self-diffusion in pure Ag at the melting temperature of Ag [192]. Consequently, the extrapolation of impurity diffusion coefficients of Ag in Au [167], from high to low temperatures, is justified.

To estimate the contribution of divacancies to Au impurity diffusion in pure Ag the impurity diffusion coefficients of Au in Ag, as determined in this study by the D-M treatment or N-P treatment, and the impurity diffusion coefficients of Au in Ag from higher temperatures [167] are fitted by equation 4.8 (see figure 4.6). If the impurity diffusion coefficients of Au in Ag, as determined according to the N-P treatment, are used the contribution of divacancies[5] to the diffusion mechanism is unrealistically large (i.e. >85% at temperatures >700 °C). If the impurity diffusion coefficients of Au in Ag, as determined according to the D-M treatment, are used a more realistic value of the contribution of divacancies[6] to the diffusion mechanism is obtained (i.e. <35 % at temperatures >700 °C), as compared with the contribution of divacancies to Ag self-diffusion in pure Ag (see figure 4.3a), which is ≈ 15 %

[5] $Q_{1V} = 1.57$ eV, $D_{0,1V} = 2.29 \cdot 10^{-8}$ m²/s, $Q_{2V} = 2.14$ eV, $D_{0,2V} = 1.31 \cdot 10^{-4}$ m²/s
[6] $Q_{1V} = 1.84$ eV, $D_{0,1V} = 2.52 \cdot 10^{-6}$ m²/s, $Q_{2V} = 2.40$ eV, $D_{0,2V} = 1.10 \cdot 10^{-3}$ m²/s

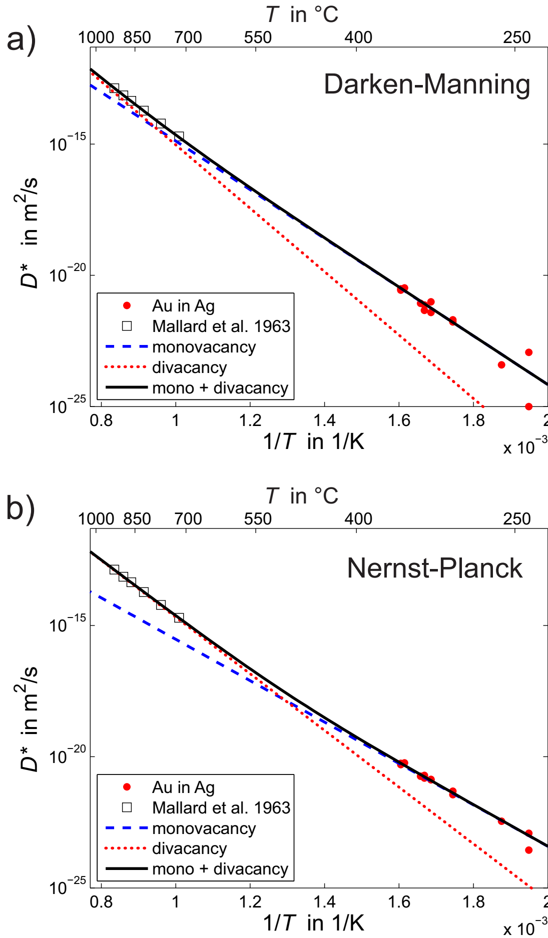

Figure 4.6: Estimation of the divacancy contribution to the diffusion mechanism for Au impurity diffusion in pure Ag, using the literature data from Ref. [167] and the fitted impurity diffusion coefficients of Au in Ag, applying a) the Darken-Manning (D-M) treatment and b) the Nernst-Planck (N-P) treatment. If the Nernst-Planck treatment is applied for fitting of the impurity diffusion coefficients of Au in Ag, an unrealistically large divacancy contribution at higher temperatures is obtained, whereas the divacancy contribution is considerably smaller if the Darken-Manning treatment is applied.

at 700 °C. Thus, the determined impurity diffusion coefficients of Au in Ag obtained by applying the D-M treatment are more realistic than those obtained by applying the N-P treatment. This implies that sufficient vacancy sources and sinks are active during interdiffusion.

4.3.4 Comparison of the Darken-Manning and Nernst-Planck treatments

Despite the considerably different assumption in the D-M treatment and the N-P treatment on the vacancy concentration, the measured intensity-depth profiles can be well described by the D-M treatment as well as the N-P treatment (see figure 4.2b and figure 4.2c, respectively). This is a direct consequence of the relatively modest difference[7] of the chemical diffusion coefficients $\widetilde{D}_{\mathrm{DM}}$ and $\widetilde{D}_{\mathrm{NP}}$ in the concentration range $x_{\mathrm{Au}} \geq 10$ at.%, as obtained from the D-M and the N-P treatment applying the self-diffusion coefficients, $D^{*}_{\mathrm{Ag\ in\ Ag}}$ and $D^{*}_{\mathrm{Au\ in\ Au}}$, from literature and the here obtained impurity diffusion coefficients, $D^{*}_{\mathrm{Ag\ in\ Au}}$ and $D^{*}_{\mathrm{Au\ in\ Ag}}$, as described in section 4.3.2 (see figure 4.4). The interplay of the absolute values of the self-diffusion coefficients, $D^{*}_{\mathrm{Ag\ in\ Ag}}$ and $D^{*}_{\mathrm{Au\ in\ Au}}$, the impurity diffusion coefficients, $D^{*}_{\mathrm{Ag\ in\ Au}}$ and $D^{*}_{\mathrm{Au\ in\ Ag}}$, and the concentration dependence of the self-diffusion coefficients results in relatively modestly different chemical diffusion coefficients and consequently the calculated concentration-depth profiles applying the numerical values of the chemical diffusion coefficients calculated either according to the D-M treatment or the N-P treatment, are very similar and describe the measured intensity-depth profiles almost equally well. The fitted genuine concentration-depth profiles deviate significantly from each other only at small Au concentrations ($x_{\mathrm{Au}} \leq 10$ at.%). This concentration range is very difficult to access by sputter-depth profiling due to the considerable sputter induced broadening of the genuine concentration-depth profile in this concentration range.

It follows that the concentration-depth profiles do not allow to decide between the D-M and N-P approaches. However, such distinction is possible considering the impurity diffusion coefficients as a function of temperature (see section 4.3.3).

[7] The difference between the chemical diffusion coefficient obtained by applying the D-M or the N-P treatment, $|(D_{\mathrm{D\text{-}M}} - D_{\mathrm{N\text{-}P}})/D_{\mathrm{D\text{-}M}}|$, is smaller than 50 % for $x_{\mathrm{Au}} \geq 10$ at.%.

4.3.5 Positron annihilation DBS experiments

The change of the S-parameter in the Au and Ag layer during diffusion annealing depends on the activity of vacancy sources and sinks. As shown in section 4.3.3, substitutional diffusion of Ag in Au is considerably faster than substitutional diffusion of Au in Ag. As a result of this diffusional asymmetry, a supersaturation of vacancies tends to be established in the Ag layer and a vacancy undersaturation tends to be established in the Au layer during interdiffusion, if no vacancy sources and sinks are active. Only if sufficient vacancy sources and sinks are active, vacancies can be generated in the Au sublayer and annihilated in the Ag sublayer. In that case the vacancy concentration-depth profile and thus the S-parameter at the Au/Ag interface remains largely unchanged during diffusion annealing, i.e. the (equilibrium) vacancy concentration is maintained (D-M case). However, in a system without sufficient active vacancy sources and sinks, the equilibrium vacancy concentration cannot be maintained (N-P case). As a result, the vacancy concentration decreases in the Au sublayer and increases in the Ag sublayer upon interdiffusion. In that case the S-parameter in the Au sublayer is expected to decrease, whereas the S-parameter in the Ag sublayer is expected to increase during diffusion annealing.

The determined S-parameters as a function of positron-implantation energy for the different annealing times of 56 min, 337 min and 618 min are shown in figure 4.7a. For each annealing time the set of data is characterised by a U-shaped function. At low positron-implantation energies (< 3 keV), for which positron annihilation occurs predominantly at the surface of the specimen (see the estimated positron-implantation fractions in figure 4.8), the S-parameter exhibits a relatively large value of about 0.484. At intermediate positron-implantation energies (3-8 keV), corresponding to preferred annihilation in the Au (top) sublayer, the S-parameter decreases to a minimum value of about 0.460 at 8 keV. At larger positron-implantation energies (> 8 keV) the S-parameter increases and reaches a maximum value of about 0.505 at a positron-implantation energy of 29 keV, corresponding to predominant positron annihilation in the Si substrate.

Upon diffusion annealing, the S-parameter slightly decreases for positron-implantation energies between 3 keV-13 keV (see figure 4.7a). Approximating the change of the S-parameter over annealing time by a linear function (for an example see inset in figure 4.7b) for each positron-implantation energy, it is revealed (see figure 4.7b) that the decrease of the S-parameter is the most pronounced at a positron-implantation energy of 4.5 keV, which corresponds to preferred positron annihilation in the Au sublayer. At positron-implantation energies corresponding to preferred annihilation in the Ag sub-

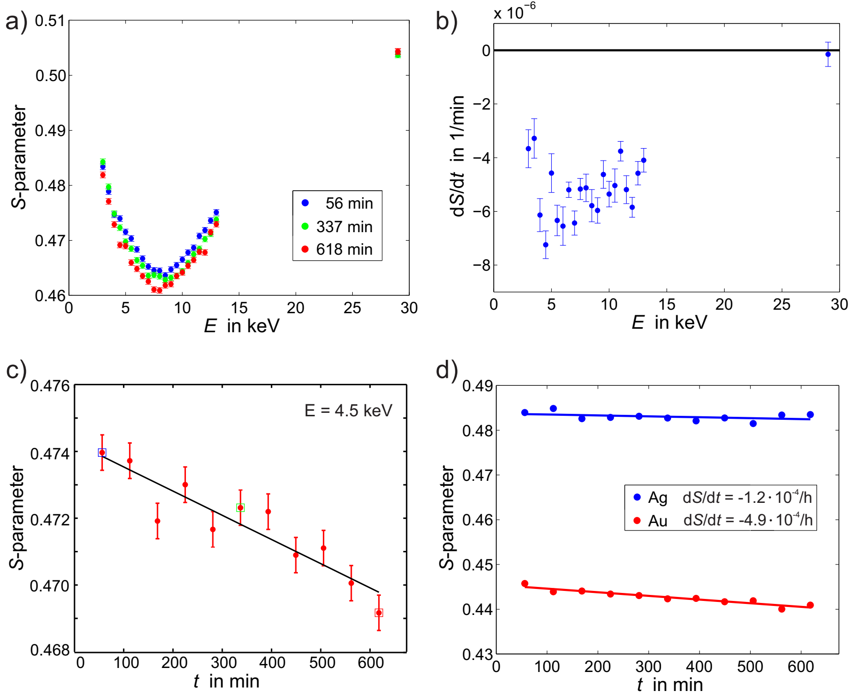

Figure 4.7: a) Evolution of the S-parameter in dependence of the positron-implantation energy for different annealing times at an annealing temperature of 330 °C. b) Time derivative of the S-parameter upon diffusion annealing as a function of positron-implantation energy, as determined from the slopes of the linear functions fitted to c) the time dependent S-parameters determined at different annealing times at each positron-implantation energy. d) Fitted S-parameters of the individual sublayers as a function of annealing time using the VEPFIT [181, 182] program.

layer (> 10 keV) the decrease of the S-parameter over time is smaller than at positron-implantation energies corresponding to preferred annihilation in the Au sublayer. The separation of the change of the S-parameters during diffusion annealing in the individual sublayers applying VEPFIT (see figure 4.7d) confirms this general trend: The decrease of the S-parameter in the Au sublayer is larger than in the Ag sublayer.

The observed decrease of the S-parameter over time (see figure 4.7b-d) might be explained by the establishment of a non-equilibrium vacancy con-

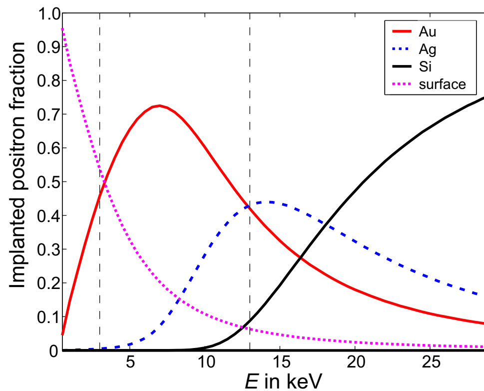

Figure 4.8: Positron-implantation fractions in an Au/Ag bilayer, as estimated using VEPFIT [181, 182]. A positron-diffusion length of 37 nm was assumed for the Ag and Au layer. The investigated positron-implantation energy range (3 keV to 13 keV) for the *in-situ* heating experiments is indicated by dashed lines.

centration-depth profile upon interdiffusion. The decrease of the S-parameter is the strongest at positron implantation energies (about 4.5 keV) corresponding to predominant positron annihilation in the Au sublayer (see figure 4.8), indicating a decrease of the vacancy concentration (N-P case). At larger positron implantation energies, corresponding to preferred annihilation in the Ag sublayer, the S-parameter decreases only slightly (for the N-P case an increase in vacancy concentration and consequently an increase of the S-parameter is expected), which might be attributed to the increase of the S-parameter due to interdiffusion and the simultaneous occurring microstructural changes (e.g. domain growth), causing a small net decrease of the S-parameter in the Ag sublayer.

It is recognised that microstructural changes during diffusion annealing, such as domain growth, might be exclusively responsible for the observed trends in the S-parameters. The growth of domains (i.e. the annihilation of small angle grain boundaries) during diffusion annealing is associated with a decrease of the open-volume defects and thus leads to a decrease of the S-parameter. The extent of domain growth and thus the decrease of the S-parameter is probably smaller in the *pre-annealed* Ag sublayer as compared to the decrease of the the S-parameter in the (*not pre-annealed*) Au sublayer which complies with the determined change of the S-parameter (see figures 4.7b-d).

In general, the broad positron-implantation profiles in metallic thin films with a small defect concentration (and thus a large positron-diffusion length) limits the depth resolution of positron annihilation DBS and hence the sensitivity to determine changes in the defect concentration especially at larger depths. Therefore, in this work both positron-annihilation DBS spectroscopy and AES sputter-depth profiling have been applied in a complementary way to extract information about interdiffusion in thin films.

4.4 Conclusions

Interdiffusion in single-crystalline Au/Ag bilayers on Si (0 0 1) substrates has been investigated by Auger electron spectroscopy sputter-depth profiling and positron-annihilation Doppler broadening spectroscopy. The impurity diffusion coefficients of Ag in Au and Au in Ag could be assessed in the temperature range of 240 °C - 350 °C.

- The results allowed distinction of the application of the Darken-Manning (D-M) treatment and that of the Nernst-Planck (N-P) treatment: the impurity diffusion coefficients at high and low temperatures can be well described according the D-M treatment.

- The experimental accuracy of the determined concentration-depth profile does not allow to distinguish between the D-M and the N-P treatment for the calculation of the chemical diffusion coefficient.

- The *in-situ* positron annihilation Doppler broadening spectroscopy investigations revealed a depth dependent change of the S-parameter during diffusion annealing, which cannot be explained by a change of the vacancy concentration depth profile during diffusion annealing according to either the D-M treatment or the N-P treatment. Most likely, microstructural changes, as domain growth, dominate the observed changes of the S-parameter.

In the investigated epitaxial single-crystalline Au/Ag thin films, sufficient vacancy sources and sinks are likely to be operative during diffusion annealing and the equilibrium vacancy concentration depth profile is likely to be maintained during interdiffusion. It would be desirable to investigate even higher quality thin films where eventually the N-P regime should prevail.

Acknowledgements

The authors want to acknowledge experimental assistance during the positron annihilation measurements from Dipl.-Phys. Thomas Gigl (with TUM), Nina Stitz for AFM measurements (with Uni Stuttgart) and Reinhart Völker for Si_3N_4 thin-film deposition (with MPI-IS).

Chapter 5

Interdiffusion and stress development in single-crystalline Pd/Ag bilayers

Martin A. Noah[1], David Flötotto[1], Zumin Wang[1,2], and
Eric J. Mittemeijer[1,3]

[1] *Max Planck Institute for Intelligent Systems (formerly Max Planck Institute for Metals Research), Heisenbergstr. 3, D-70569 Stuttgart, Germany*
[2] *School of Materials Science and Engineering, Tianjin University, Tianjin 300052, China*
[3] *Institute for Materials Science, University of Stuttgart, Heisenbergstr. 3, D-70569 Stuttgart, Germany*

Abstract

Interdiffusion and stress evolution in single-crystalline Pd/single-crystalline Ag thin films was investigated by Auger electron spectroscopy (AES) sputter-depth profiling and *in-situ* X-ray diffraction (XRD), respectively. The concentration-dependent chemical diffusion coefficient, as well as the impurity diffusion coefficient of Ag in Pd could be determined in the low temperature range of 356 °C to 455 °C. As a consequence of the similarity of the strong concentration-dependences of the intrinsic diffusion coefficients, the chemical diffusion coefficient varies only over three orders of magnitude over the whole composition range, despite the large difference of six orders of magnitude of the self-diffusion coefficients of Ag in Ag and Pd in Pd. It is shown that the Darken-Manning treatment should be adopted for interpretation of the experimental data; the Nernst-Planck treatment yielded physically unreasonable results. Apart from the development of compressive thermal stress, the development of stress in both sublayers separately could be ascribed to compositional stress (tensile in the Ag sublayer and compressive in the Pd sublayer) and dominant relaxation processes, especially in the Ag sublayer. The effect of these internal stresses on the values determined for the diffusion coefficients is shown to be negligible.

5.1 Introduction

It has long been recognised that interdiffusion in thin-film systems is often orders of magnitudes larger than in bulk specimens [12]. This difference is related to the microstructure of thin films, which often contain distinct densities of defects such as grain boundaries and dislocations [5]. These defects offer fast diffusion paths, in association with phenomena (first observed in bulk diffusion couples [6]) like diffusion induced grain boundary migration (DIGM) and diffusion induced recrystallisation (DIR) [7, 8].

Upon interdiffusion distinct intrinsic film stress can develop as a result of microstructural changes or due to the difference in atomic volumes of the interdiffusing components [22–26]. Such states of stress can possibly alter the interdiffusion rates in thin film specimens. A theoretical description of the interrelation of thus developing intrinsic (film) stress and interdiffusion rates has been established on the basis of a so-called network solid concept [60–62], implying conservation of lattice sites in the system and replacing the chemical potential gradient as driving force for interdiffusion by the diffusion potential as driving force. However, no conclusive experimental study on the interrelation of interdiffusion and stress exists up to date. This is generally due to the instability of the microstructure during diffusion annealing; network solids do not occur. Pronounced grain growth and diffusion induced recrystallisation during diffusion annealing of nano-crystalline specimens is associated with distinct stress changes [206, 207] and this effect can mask any stress change due to interdiffusion [22–26]. Against this background, single crystalline hetero-epitaxial thin-film systems may provide a chance to overcome such problems and thus provide a better approach to investigate the interplay of interdiffusion and stress development upon diffusion annealing. To this end, the system Ag-Pd appears as an ideal model system. The lattice parameters of Ag and Pd are sufficiently different (4.08620 Å and 3.89019 Å, respectively), to induce the development of compositional stress during interdiffusion and also to allow the determination of the stress in the two sublayers separately by X-ray diffraction. Furthermore, Ag and Pd are miscible over the whole concentration range [208] and thus no complication by the formation of new phases can occur.

Besides the above sketched fundamental scientific interest for a study of interdiffusion in a hetero-epitaxial single-crystalline Pd/Ag thin film, Ag and Pd thin films are of great technological importance in catalysis [209] and hydrogen separation [210]. The reliability and performance during operation of Ag-Pd based devices strongly rely on a comprehensive knowledge of interdiffusion in this system: for example, for Ag-Pd based membranes used for hydrogen separation the concentration gradient in the surface adjacent

region strongly influences the hydrogen adsorption and hydrogen solubility [211] and thus requires a precise adjustment of the concentration-depth profile, i.e. by annealing of layered systems [37, 212–214]. This is only achievable with a comprehensive knowledge of the concentration-dependent diffusion coefficients. However, self- and impurity diffusion data for the system Ag-Pd are only available for temperatures above 715 °C [195, 215], which temperatures are much larger than the practical, operation temperatures of around 350 °C [211]. The availability of low temperature diffusion data is of even larger importance for Pd/Ag core-shell nanostructures used in optics [216] or catalysis [209, 217]. For such systems, diffusion lengths in the nanometre range can already destroy the functional properties.

In this study, interdiffusion in single-crystalline Pd/single-crystalline Ag bilayers on Si substrates has been investigated in the temperature range from 356 °C to 455 °C by Auger electron spectroscopy (AES) sputter-depth profiling. By correcting the measured Auger electron intensity-depth profiles for sputter-induced alterations, the concentration-dependent chemical diffusion coefficient and the impurity diffusion coefficient of Ag in Pd have been deduced. Furthermore, the stress evolution during thermal cycling and (prolonged) isothermal annealing has been revealed by *in-situ* stress measurements by X-ray diffraction. The results obtained have been discussed in terms of the occurring microstructural changes.

5.2 Experimental procedure

5.2.1 Specimen preparation

Pd/Ag thin films were prepared in two successive deposition steps. Firstly, a single-crystalline, epitaxial Ag(001) thin film with a thickness of 150 nm was deposited at room temperature, in a customised ultrahigh vacuum (UHV) system (base pressure $< 3 \cdot 10^{-8}$ Pa) by thermal evaporation of pure Ag ($>$ 99.995 wt.%) from an Al_2O_3 crucible, onto a thoroughly cleaned Si(001) 2×1 substrate surface (boron doped with a resistivity of 1-10 Ωcm and a miscut $< 0.1°$) (see Ref. [218] for details of the Ag thin film preparation conditions). Subsequently, the specimen was post annealed in UHV at about 160 °C for 90 min. After cooling to room temperature, the specimen was removed from the UHV system and transferred immediately to a magnetron sputtering system. Any contamination on the Ag surface resulting from the air exposure during specimen transfer, was removed by applying a radio frequency-sputter cleaning procedure for 2 min. No carbon or oxygen contamination could be detected by X-ray photoelectron spectroscopy and Auger electron spectroscopy sputter-depth profiling. Next, an epitaxial Pd

layer of either 50 nm or 100 nm thickness, for the stress measurements and the interdiffusion study, respectively, was deposited at room temperature, by magnetron sputtering of pure Pd (99.999 wt.%), onto the epitaxial Ag(001) film. The argon pressure was adjusted to $3.2 \cdot 10^{-3}$ mbar and a power of 150 W or 50 W was applied. In order to avoid oxidation of the Pd film surface during diffusion annealing, the specimen was covered with a 15 nm thick, magnetron sputtered amorphous carbon layer.

In order to determine the concentration-dependent chemical diffusion coefficient by AES sputter-depth profiling the 13.9 mm × 13.9 mm large specimens were cut into small pieces and encapsulated in argon filled quartz ampules. Diffusion annealing was performed in a salt bath for annealing times ranging from 7 min up to 8 h at selected temperatures in a temperature range of 356 °C up to 455 °C.

For the *in-situ* stress measurements by X-ray diffraction, which requires prolonged diffusion annealing, an additional 20 nm thick Si_3N_4 layer was deposited on top of the amorphous carbon capping layer in order to improve the surface stability during the longtime annealing experiments.

5.2.2 Microstructural characterisation

The surface morphology of the single-crystalline Ag single layers and of the single-crystalline, hetero-epitaxial Pd/Ag bilayers was investigated by a Nano Scope IIa atomic force microscope (AFM) from VEECO, equipped with Si tips and operating in tapping mode. The texture of the Pd/Ag bilayers was investigated by using a Philips MRD Pro diffractometer equipped with a secondary monochromator and employing Co K_α radiation (λ = 1.78897 Å). The {1 1 1} pole figures were measured at diffraction angles, 2θ, of 44.57° and 46.94° for the Ag and Pd sublayers, respectively, with steps in ϕ and ψ of $\Delta\phi = \Delta\psi = 1°$, where ϕ is the rotation angle around the specimen-surface normal and ψ is the angle between the diffraction vector and the specimen-surface normal.

Cross-sectional (high resolution) transmission electron microscopy ((HR) TEM) specimens were prepared by a lift-out technique [219], applying a Zeiss Crossbeam 1540 EsB. To this end, thin lamella were cut from the specimen by ion milling applying Ga ions with an energy of 30 keV. The lamella were then transferred to a TEM grid and further thinned with continuously decreasing ion currents (10 nA-10 pA), until electron transparency was achieved. The thus prepared specimens were transferred immediately after preparation to a JEOL ARM200F transmission electron microscope, operating at an acceleration voltage of 200 kV.

5.2.3 In-situ XRD stress measurements

In-situ XRD stress measurements during thermal cycling and isothermal annealing were performed on a Bruker D8 diffractometer equipped with an X-ray lens and an energy dispersive detector (Sol-XE from Bruker) employing Cu K_α radiation ($\lambda = 1.54060$ Å). For *in-situ* heating an Anton Paar DHS 900 heating chamber, mounted on the diffractometer, was applied with a constant argon flow of 5 l/h during the heat treatment. The specimen was subjected to two subsequent thermal cycles, each from 27 °C to 417 °C and back to 27 °C, before performing a third thermal cycle, including an isothermal annealing step for ≈ 4.4 h at 417 °C. To this end, the temperature was changed in steps of 20 °C with a heating/cooling rate of 1 K/s. After each temperature change, a 4 min holding time was applied to allow the specimen to establish a homogeneous temperature. After the 4 min long holding time $\theta - 2\theta$ scans were recorded for 2θ ranges around the (1 1 3), (3 3 1), (3 1 1), (2 0 2), $(3\,\bar{1}\,3)$ and $(3\,\bar{3}\,1)$ poles (at selected ϕ and ψ values) of the single-crystalline Ag and the single-crystalline Pd layers. The measurement time for the six poles of the Ag and Pd sublayers at each temperature step was 12 min, leading to a total time of (12 min+4 min (see above)=) 16 min at each temperature step. The temperature was calibrated by using the determined strain-free lattice parameter [220] and the known thermal expansion of Pd [221]. The Pd peak position did not change due to interdiffusion (see section 5.3.6) and thus could be utilised as an internal reference for temperature calibration.

Due to the well separated diffraction peaks of Ag and Pd (cf. section 5.3.6), the stress parallel to the surface, $\sigma_{||}$, in a sublayer can be determined from the lattice strain, ϵ_ψ, determined from the peak positions of different *hkl* reflections recorded at different ψ (and ϕ), adopting a planar state of stress with equal principal stresses[1], $\sigma_{11} = \sigma_{22} = \sigma_{||}$, (see appendix 5.E) according to (cf. Ref. [220])

$$\epsilon_\psi = \frac{d - d_0}{d_0} = \left[\left(S_{11} - S_{12}\right)\sin^2\psi + 2S_{12}\right] \cdot \sigma_{||} \tag{5.1a}$$

$$\sin^2\psi_0 = -\frac{2S_{12}}{S_{11} - S_{12}} \qquad \text{for} \qquad d = d_0 \tag{5.1b}$$

where d is the measured lattice spacing, d_0 is the strain free lattice spacing, S_{11} and S_{12} are the temperature dependent single-crystalline elastic con-

[1] The investigated single-crystalline thin films do exhibit a (001) surface orientation. Consequently, equal principal stresses are expected for the planar stress state in the investigated bilayer.

stants [222], $\sigma_{||}$ denotes the equibiaxial stress in the thin film, ψ is the angle of the diffraction vector with respect to the specimen-surface normal and ψ_0 represents the strain-free direction.

The lattice spacing of the (1 1 3), (3 3 1), (3 1 1), (2 0 2), $(3\,\bar{1}\,3)$ and $(3\,\bar{3}\,1)$ lattice planes of Ag and Pd were determined from the corresponding diffraction peaks by fitting the Kα_1 and Kα_2 component with a pseudo-Voigt function and applying Bragg's law. A constant intensity ratio of Kα_2 to Kα_1 of 0.5 [223] as well as a 2θ independent background were applied. The equibiaxial in-plane stress in the Ag and Pd sublayers was determined from the slope of the straight line fitted to the experimental data in a plot of ϵ_ψ, versus $\sin^2\psi$ (see appendix 5.E).

5.2.4 Auger electron spectroscopy (AES) sputter-depth profiling

AES sputter-depth profiling of the as-prepared and diffusion annealed specimens was conducted with a JEOL JAMP-7830F AES system equipped with a hemispherical analyser and a field emission electron gun operating at an acceleration voltage of 10 kV and a beam current of 10 nA (for details, see Ref. [112] and its supplemental material). Sputter-depth profiling was performed with a focused 1 keV Ar^+ ion beam (rastering over the specimen surface) in an intermittent mode with sputter steps of 20 s - 60 s (corresponding to layer increments of thickness of 1.7 nm - 5.0 nm for Ag and of 1.1 nm -3.3 nm for Pd). In order to avoid ion channelling along low indexed lattice planes an offset of $\approx 40.5°$ between the ion-gun and the specimen-surface normal was chosen. After each sputter step, spectra of the Ag_{NVV} (kinetic energy = 80 eV), Pd_{NVV}(78 eV), Si_{LMM}(92 eV), Pd_{MNN} (326 eV), Ag_{MNN} (351 eV), O_{KLL}(503 eV) and Si_{KLL}(1610 eV) Auger transitions were recorded with an energy step size of 1 eV while scanning the primary electron beam over an area of 1 µm × 1 µm. The measured AES spectra were differentiated by a 7 point-algorithm and fitted with a linear least squares fitting procedure, or in the case of overlapping AES spectra, with the target factor analysis [114]. The low energetic Ag_{NVV} and Pd_{NVV} AES transitions were not considered for the evaluation, since the similarity of the kinetic energies of these Ag_{NVV} and Pd_{NVV} AES electrons (80 eV and 78 eV, respectively) does not allow a reliable separation with the target factor analysis. In order to account for the effects of sputter-induced alterations, such as ion bombardment induced atomic mixing and surface roughening, as well as the intrinsic specimen surface and interface roughnesses, on the measured intensity-depth profiles, an extended Mixing-Roughness-Information depth (MRI) model has been applied [85, 112]. Thus, the genuine concentration-depth profile is determined in a forward calculation approach (for details, see Ref. [112]).

5.3 Results and Discussion

5.3.1 Initial and annealed microstructure

The as-prepared Pd layer/Ag layer/Si substrate system exhibits a cube-on-cube orientation relationship, as established by the XRD pole-figure measurements (cf. section 5.2.2), according to (see figure 5.1)

$$\mathrm{Pd}(0\,0\,1)\,||\,\mathrm{Ag}(0\,0\,1)\,||\,\mathrm{Si}(0\,0\,1), \quad \mathrm{Pd}[1\,1\,0]\,||\,\mathrm{Ag}[1\,1\,0]\,||\,\mathrm{Si}[1\,1\,0]. \tag{5.2}$$

Both sublayers posses a very small (< 1 vol.%) amount of twins on $\{1\,1\,1\}$ planes, inclined with respect to the (001) oriented specimen surface, resulting in a $\{5\,1\,1\}$ texture component [183]. For both sublayers the pole figures indicate the presence of small angle grain boundaries, i.e. mosaicity in the single-crystalline sublayers; no grain boundaries could be observed by cross-sectional TEM (see figure 5.2a).

The HRTEM image of the as-prepared specimen reveals a significant amount of misfit dislocations at the Pd/Ag interface (see figure 5.2c), which partially relax the large lattice mismatch of Ag and Pd of 5 %. The contrast at the interface indicates that not all coherency stress had become relaxed by the misfit dislocations at the Pd/Ag interface (cf. Ref. [224]).

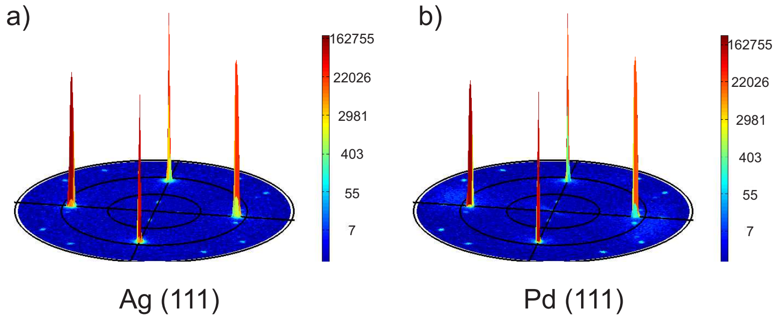

Figure 5.1: (111) pole figures of the Pd/Ag bilayer at a) $2\theta = 44.57°$ corresponding to Ag(111) and at b) $2\theta = 46.94°$ corresponding to Pd(111) reveal a cube on cube orientation relationship of both sublayers with the Si(001) substrate. In addition to the Ag(111) and Pd(111) poles, reflections from twins in both sublayers on 111 planes, inclined with respect to the surface, can be observed (twinned volume < 1 vol.%). The intensity is plotted on a logarithmic scale.

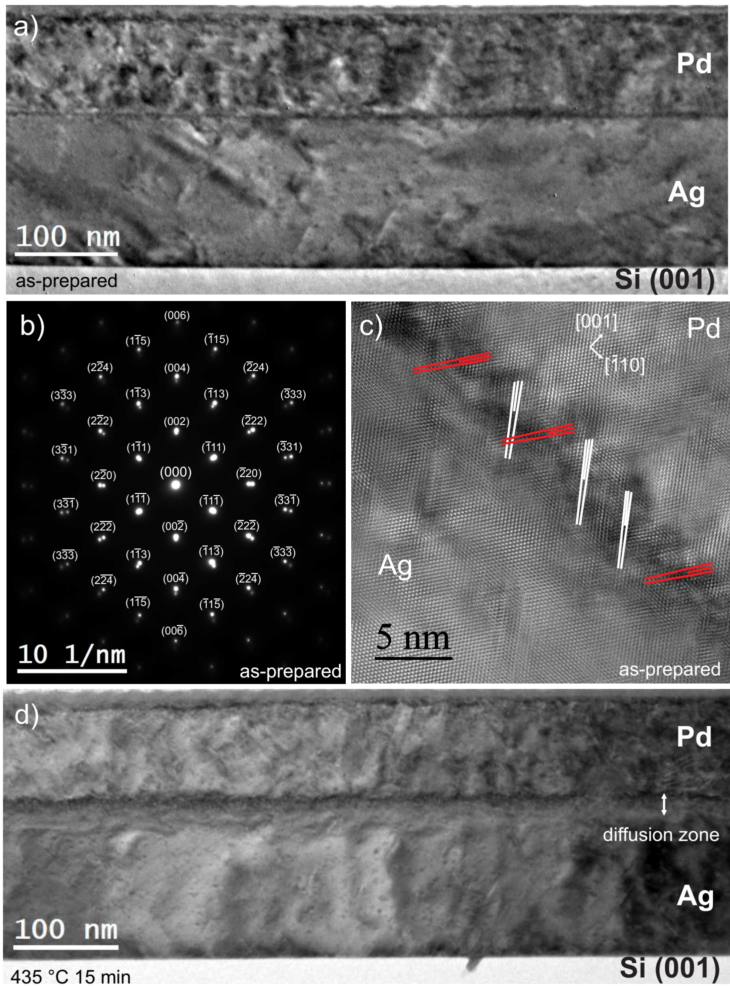

Figure 5.2: a) Cross sectional TEM bright field image of an as-prepared Pd(100 nm)/ Ag(150 nm) bilayer. b) The selected area diffraction pattern of the as-prepared Pd/Ag bilayer (zone axis [110] for both sublayers) shows distinct diffraction spots of the Ag and Pd sublayers and confirms the single-crystalline nature of the sublayers. The contrast in the single crystalline layers is caused by thickness variations, coherency stress at the Pd/Ag interface and (TEM-foil preparation-induced) defects. c) High resolution cross-sectional TEM image of the as-prepared Pd/Ag interface, which shows many misfit dislocations (indicated by white and red symbols). d) Cross sectional TEM bright field image of an Pd/Ag bilayer after diffusion annealing at 435 °C for 15 min. No nucleation of new grains, as by diffusion-induced recrystallisation, is observed.

AFM measurements show that the surface of the Pd/Ag bilayers (see figure 5.3), as well as of Ag single layers (not shown) are very smooth with a root mean squared roughness (RMS) of only 0.3 nm [218] and 0.5 nm for the Ag single layer and the Pd/Ag bilayer, respectively. The bilayers are not completely massive, holes occur with an average distance of ≈ 200 µm, which is very much larger than the diffusion lengths ($2\sqrt{Dt} < 13.6$ nm) pertaining to the experiments used for the determination of diffusion coefficients in this study.

After 15 min of diffusion annealing at 435 °C the establishment of a diffusion zone around the initial Pd/Ag interface could be observed (see figure 5.2d). The emerging contrast of the diffusion zone in the TEM bright field diffraction-contrast image can be related to the diffusion induced development of stress. No change in surface roughness or nucleation of new grains, by diffusion induced recrystallisation, could be observed. However, after prolonged annealing (i.e. $2\sqrt{Dt} > 13.6$ nm)[2] segregation of Ag at the Pd/C interface could be observed, which is accompanied by a pronounced increase in surface roughness (see appendix 5.C). The AES sputter-depth profiling measurements for the determination of the concentration-dependent chemical diffusion coefficient were exclusively performed on specimens, which did not show an increase of the specimen surface roughness (i.e. $2\sqrt{Dt} < 13.6$ nm).

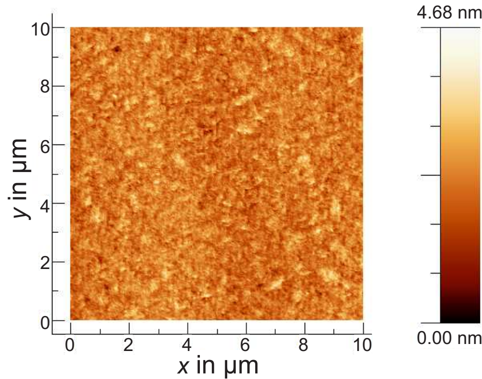

Figure 5.3: AFM image of the surface of an Pd/Ag bilayer. The root mean squared roughness of the surface is 0.5 nm.

[2] As estimated from the maximal chemical diffusion coefficient at the respective annealing temperature.

5.3.2 Concentration-depth profiles

The measured AES intensity-depth profiles of the as-prepared Pd/Ag bilayer with a sharp interface (see figure 5.2c) can be described with the MRI parameters given in table 5.1 (see figure 5.4a). Similar MRI parameters were obtained in case of epitaxial Au/Ag(0 0 1) thin films [218].

AES sputter-depth profiling revealed that upon diffusion annealing an "asymmetric" intensity-depth profile develops (see figure 5.4b). Hence diffusion of Pd into the Ag sublayer is considerably faster than the diffusion of Ag into the Pd sublayer. Consequently, the developing concentration-depth profiles cannot be described with a simple error function model with a concentration-independent chemical diffusion coefficient [41]. In the present study, the measured sputter-depth profiles were modelled by incorporating appropriate physical diffusion models, involving a concentration-dependent chemical diffusion coefficient, in the MRI forward calculation approach as described below (see also Refs. [112, 218]).[3]

As shown by HRTEM analysis, the Pd/Ag interface exhibits a high density of misfit dislocations (see figure 5.2c) due to the relatively large lattice mismatch of Ag and Pd of 5 %. These defects serve as vacancy sources and sinks [225–227] and thus the equilibrium vacancy concentration can be maintained during interdiffusion. This implies that the Darken equation [45] for the chemical diffusion coefficient, $\widetilde{D}$, incorporating the vacancy-wind factor, S_{wind}, of Manning [50, 59], can be applied (see also section 5.3.5):

$$\widetilde{D}_{\mathrm{DM}} = ((1 - x_{\mathrm{Pd}})D_{\mathrm{Pd}} + x_{\mathrm{Pd}}D_{\mathrm{Ag}}) \cdot S_{\mathrm{wind}}, \tag{5.3}$$

where x_{Pd} is the molar fraction of Pd and D_{Ag} and D_{Pd} are the intrinsic diffusion coefficients of Ag and Pd, respectively.[4] The vacancy-wind factor, S_{wind}, which describes correlation effects in a random alloy arising by a net flux of vacancies, can be approximated according to [50, 59]

$$S_{\mathrm{wind}} = 1 + \frac{1-f}{f} \cdot \frac{x_{\mathrm{Ag}}x_{\mathrm{Pd}}(D^*_{\mathrm{Ag}} - D^*_{\mathrm{Pd}})^2}{(x_{\mathrm{Ag}}D^*_{\mathrm{Ag}} + x_{\mathrm{Pd}}D^*_{\mathrm{Pd}}) \cdot (x_{\mathrm{Ag}}D^*_{\mathrm{Pd}} + x_{\mathrm{Pd}}D^*_{\mathrm{Ag}})}, \tag{5.4}$$

where f is the geometric correlation factor for the crystal-lattice (i.e. 0.7815 for the fcc crystal structure [50]) and D^*_{Ag} and D^*_{Pd} are the concentration-

[3] The depth resolution of the applied AES sputter-depth profiling technique, as estimated from the MRI parameters obtained from an as-prepared specimen according to Ref. [85], is $\Delta z = \sqrt{(2\sigma)^2 + (1.67\lambda)^2 + (1.67w)^2} \approx 6.4$ nm, which is less than half of the mean diffusion length of 13.6 nm established in this study. The associated broadening of the depth profile is accounted for in the quantitative analysis.

[4] The effect of the small (< 1 %) deviation of the molar volume from Vegard's law [228] is neglected in this study [103, 229].

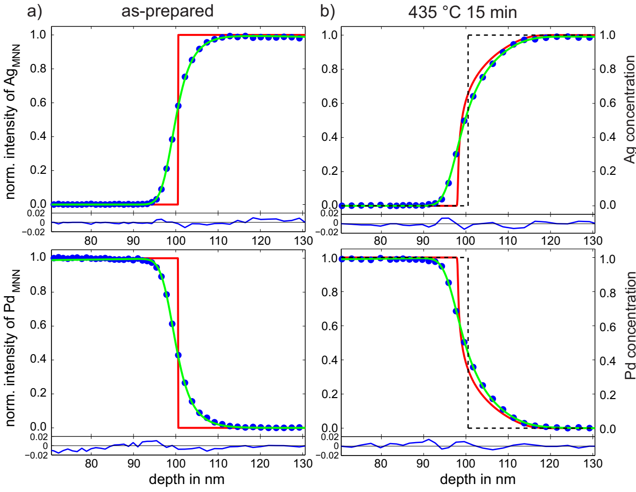

Figure 5.4: Measured AES sputter-depth profiles and deduced concentration-depth profiles of a) an as-prepared Pd(100 nm)/Ag(150 nm) bilayer and b) after diffusion annealing at 435 °C for 15 min. The sputter-depth profiles were fitted by applying the MRI model (see section 5.2.4). The experimental, measured data points have been indicated by blue dots. The assumed genuine concentration-depth profile with a sharp interface for the as-prepared specimen (a) or the fitted one for the annealed specimen (b), as calculated by numerically solving Fick's second law (as discussed in section 5.3.2) have been plotted in red. The corresponding fitted normalised intensity-depth profile, obtained by the MRI model, has been plotted in green. The used MRI parameters have been listed in table 5.1.

Table 5.1: MRI parameters for roughness, σ, mixing, w, effective attenuation length in the respective pure component, λ [92], mean effective backscattering decay length, L, and backscattering correction factor, R [100]. The parameters σ, L and w have been obtained from a fit to an as-prepared specimen adopting a step like concentration-depth profile. For the mixing parameters, w, the projected ion range, as estimated by SRIM [94], has been used as a starting value for the fitting.

σ	w_{Ag}	w_{Pd}	$\lambda_{\mathrm{Ag}_{MNN}}$	$\lambda_{\mathrm{Pd}_{MNN}}$	L_{Ag}	L_{Pd}	R_{Ag}	R_{Pd}	R_{Si}
1.99 nm	3.13 nm	2.88 nm	0.59 nm	0.68 nm	50 nm	50 nm	1.85	1.78	1.32

dependent self-diffusion coefficients of Ag and Pd, respectively. Note that Equation 5.4 is only a valid approximation for similar exchange (jump) frequencies for Ag-vacancy and Pd-vacancy pairs [185]. Consideration of the exact description of the vacancy-wind effect according to Ref. [186] has only a small effect and can be neglected in this study (see appendix 5.B for an estimation of the effect of the vacancy-wind factor on the deduced chemical diffusion coefficient).

The concentration-dependent intrinsic diffusion coefficients, D_{Ag} and D_{Pd}, can be determined from the exponential concentration-dependent self-diffusion coefficients [195, 230] and the thermodynamic factor, Φ, [41] according to

$$\begin{aligned} D_{\mathrm{Ag}}(x_{\mathrm{Pd}}) &= D^*_{\mathrm{Ag}}(x_{\mathrm{Pd}}) \cdot \Phi(x_{\mathrm{Pd}}) \\ &= \left[D^*_{\mathrm{Ag\ in\ Ag}} \cdot \exp(-m_{\mathrm{Ag}} \cdot x_{\mathrm{Pd}})\right] \cdot \Phi(x_{\mathrm{Pd}}) \qquad (5.5) \\ D_{\mathrm{Pd}}(x_{\mathrm{Pd}}) &= D^*_{\mathrm{Pd}}(x_{\mathrm{Pd}}) \cdot \Phi(x_{\mathrm{Pd}}) \\ &= [D^*_{\mathrm{Pd\ in\ Pd}} \cdot \exp(-m_{\mathrm{Pd}} \cdot (1 - x_{\mathrm{Pd}}))] \cdot \Phi(x_{\mathrm{Pd}}), \qquad (5.6) \end{aligned}$$

where $D^*_{\mathrm{Ag\ in\ Ag}}$ is the self-diffusion coefficient of Ag in pure Ag and $D^*_{\mathrm{Pd\ in\ Pd}}$ the self-diffusion coefficient of Pd in pure Pd. m_{Ag} and m_{Pd} are asymmetry parameters, which describe the concentration dependence of the self-diffusion coefficients of Ag and Pd, respectively. The self-diffusion coefficients, $D^*_{\mathrm{Ag}}(1) = D^*_{\mathrm{Ag\ in\ Pd}} = D^*_{\mathrm{Ag\ in\ Ag}} \cdot \exp(-m_{\mathrm{Ag}}) = D^*_{\mathrm{Ag}}(0) \cdot \exp(-m_{\mathrm{Ag}})$ and $D^*_{\mathrm{Pd}}(0) = D^*_{\mathrm{Pd\ in\ Ag}} = D^*_{\mathrm{Pd\ in\ Pd}} \cdot \exp(-m_{\mathrm{Pd}}) = D^*_{\mathrm{Pd}}(1) \cdot \exp(-m_{\mathrm{Pd}})$, are the impurity diffusion coefficients of Ag in Pd and of Pd in Ag, respectively.

The thermodynamic factor, Φ, can be approximated [231] adopting a regular solution model for the Ag-Pd solid solution according to

$$\Phi = 1 - 2x_{\mathrm{Pd}}(1 - x_{\mathrm{Pd}})\frac{\Omega}{RT}, \qquad (5.7)$$

where the concentration-independent interaction parameter Ω has been taken as -9.15 kJ/mol [231],[5] R is the universal gas constant and T is the absolute temperature.

The self-diffusion coefficient of Ag in Ag (see Ref. [218]) is more than six orders of magnitude larger than the self-diffusion coefficient of Pd in Pd [233] in the temperature range of this study (356 °C - 455 °C). Consequently, the chemical diffusion coefficient, calculated according to the Darken-Manning equation, is dominated by the large intrinsic diffusion coefficient of Ag (see

[5] Note that at higher temperatures (1200 K) a more negative mixing enthalpy has been reported [232], implying an interaction parameter of $\Omega = -20.64$ kJ/mol.

figure 5.5a). Therefore, the self-diffusion coefficient of Ag in Ag and the impurity diffusion coefficient of Ag in Pd, which both determine the intrinsic diffusion coefficient of Ag according to equation 5.6, were chosen as fitting parameters (see appendix 5.A for an extended discussion of the chosen fitting parameters), while the intrinsic diffusion coefficient of Pd was calculated from literature data as follows:

(i) Literature data for the self-diffusion coefficient of Pd in Pd obtained in the temperature range of 1050 °C - 1500 °C [233] were extrapolated [6] to the temperature range of this study (356 °C - 455 °C).

(ii) The self-diffusion coefficients of Pd in Ag obtained in Ref. [215] cannot be straightforwardly extrapolated to the temperature range of this study because of the unknown contribution of divacancies in Ag to Pd diffusion in Ag (see Ref. [218] for a discussion of the divacancy contribution to (impurity) diffusion in Ag). Therefore, a double Arrhenius equation [53, 202] was fitted to the self-diffusion coefficients of Ref. [215] in order to estimate the contribution of divacancies to the diffusion mechanism of Pd in Ag:

$$D = D_{0,1V} \cdot \exp\left(-\frac{Q_{1V}}{RT}\right) + D_{0,2V} \cdot \exp\left(-\frac{Q_{2V}}{RT}\right), \qquad (5.8)$$

where $D_{0,1V}$, $D_{0,2V}$, Q_{1V} and Q_{2V} are the temperature independent pre-exponential factors and temperature independent activation enthalpies of the monovacancy (1V) contribution and the divacancy (2V) contribution, respectively. The activation enthalpy of the monovacancy mechanism was chosen in such a way that a fit of equation 5.8 to the self-diffusion coefficients of Ref. [215] results in approximately the same divacancy contribution to the diffusion mechanism of Pd in Ag as for Ag (self-diffusion) in Ag (see Ref. [218]). The thus determined activation enthalpies and pre-exponential factors for Pd diffusion in Ag are $Q_{1V} = 2.20$ eV, $Q_{2V} = 2.89$ eV, $D_{0,1V} = 4.07 \cdot 10^{-5}$ m^2/s and $D_{0,2V} = 2.77 \cdot 10^{-2}$ m^2/s (see table 5.2). This crude estimation of the divacancy contribution to the diffusion mechanism of Pd in Ag is expected to represent an upper limit for the extrapolated impurity diffusion coefficients of Pd in Ag at low temperatures (see appendix 5.A.2 for a discussion of the impact of a smaller impurity diffusion coefficient of Pd in Ag on the determined value of the chemical diffusion coefficient).

It is concluded that the fitting parameters in the MRI forward calculation approach for the determination of the genuine concentration-depth profile

[6] Note that, contrary to Ag self-diffusion in Ag (see what follows in the main text), self-diffusion of Pd in Pd occurs only by the (mono)vacancy mechanism [233]. Consequently it is fully justified to extrapolate the high temperature self-diffusion coefficients of Pd in Pd straightforwardly to lower temperatures.

of the diffusion annealed specimens are the self-diffusion coefficient of Ag in Ag ($D^*_{\mathrm{Ag\ in\ Ag}}$), the impurity diffusion coefficient of Ag in Pd ($D^*_{\mathrm{Ag\ in\ Pd}}$) and the location of the initial Pd/Ag interface. The genuine concentration-depth profile was calculated for each set of values of the fitting parameters by solving Fick's second law numerically using a fully implicit finite difference scheme [103].

5.3.3 Chemical diffusion coefficient

The deduced concentration-dependent chemical diffusion coefficient at all investigated temperatures shows an upward curvature with a maximum at $x_{\mathrm{Pd}} \approx 0.12$ (see figure 5.5b). The chemical diffusion coefficient is generally larger at larger Ag concentrations and decreases monotonously beyond $x_{\mathrm{Pd}} > 0.12$. This concentration dependence is reflected in the “asymmetric broadening” of the original interface as observed upon diffusion annealing (see figure 5.4b). The observed asymmetry in the interdiffusion behaviour can be qualitatively interpreted with the different homologous temperatures (T/T_m) of Ag and Pd. The higher homologous temperature of Ag ($T_m = 660\,°\mathrm{C}$) than of Pd ($T_m = 1555\,°\mathrm{C}$) during diffusion annealing results in a higher vacancy concentration in the Ag sublayer than in the Pd sublayer and consequently leads to a larger (chemical) diffusion coefficient in Ag than in Pd.

Due to the similarity of the strong concentration dependencies of the self-diffusion coefficients of Pd and Ag (see figure 5.5a), the chemical diffusion coefficient varies only by about three orders of magnitude, despite the large difference of six orders of magnitude of the self-diffusion coefficients of Ag in Ag and Pd in Pd. This concentration dependence of the chemical diffusion coefficient of the system Pd/Ag is similar to that of the system Pd/Cu [234], even though the difference in the self-diffusion coefficient of Cu in Cu [235] and the self-diffusion coefficient of Pd in Pd [233] is only three orders of magnitude.

The temperature dependence of the chemical diffusion coefficient for different Pd concentrations can be described with an Arrhenius equation in the investigated temperature range from 356 °C to 455°C. The deduced activation enthalpies and pre-exponential factors are shown in figure 5.6. Note that the uncertainty range of the deduced activation enthalpy and that of the pre-exponential factor, indicated in figure 5.6, increase considerably with increasing Pd concentration. This is related to the smaller sensitivity of the applied procedure for the determination of the chemical diffusion coefficient at higher Pd concentrations.

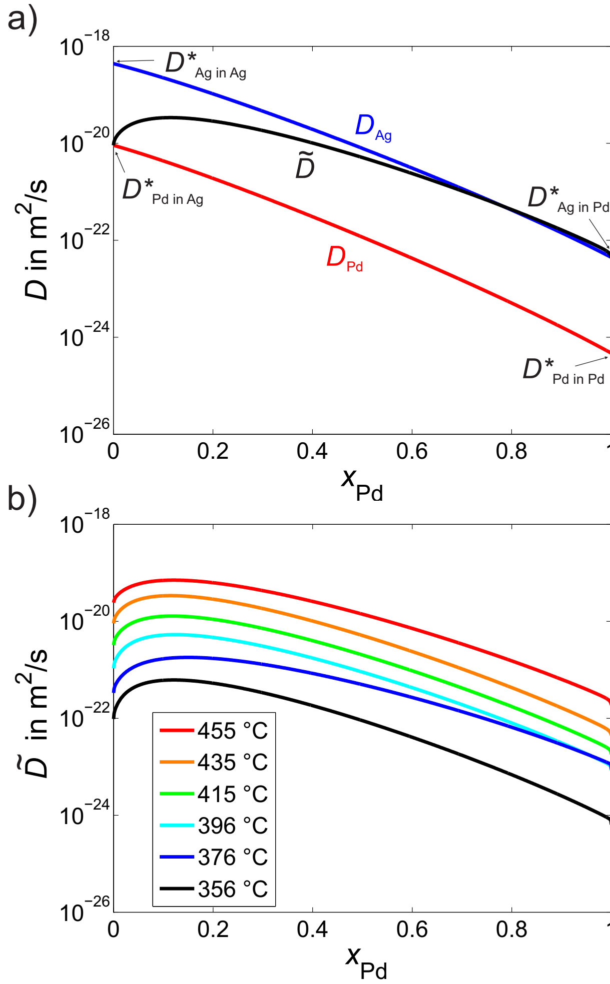

Figure 5.5: a) The self-diffusion, intrinsic diffusion and chemical diffusion coefficients determined as functions of Pd concentration for the specimen annealed at 435 °C for 15 min. b) The concentration dependence of the chemical diffusion coefficient as determined at the applied annealing temperatures.

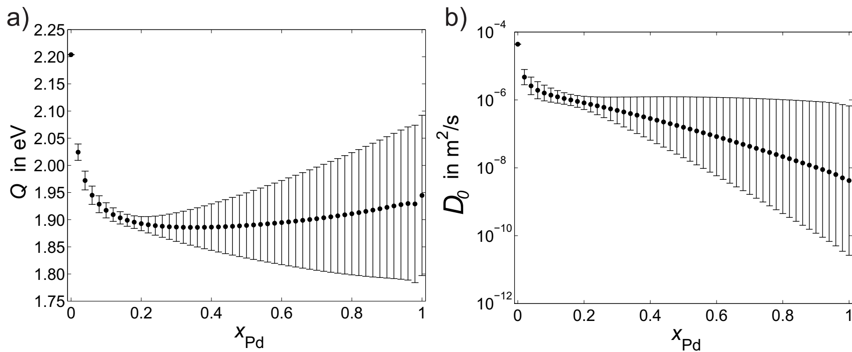

Figure 5.6: Fitted a) activation enthalpy and b) pre-exponential factor of the chemical diffusion coefficient as functions of the Pd concentration; the uncertainty ranges have been indicated.

5.3.4 Fitted self-diffusion/impurity diffusion coefficients

The determined self-diffusion coefficient of Ag in Ag and the impurity diffusion coefficient of Ag in Pd are shown as function of the reciprocal temperature in figure 5.7. The self-diffusion and impurity diffusion coefficients obtained by extrapolation from literature data at higher temperatures (as discussed in section 5.3.2) are shown as well in figure 5.7.

The here determined self-diffusion coefficients of Ag in Ag are about a factor of 3.7 smaller and have a slightly larger activation enthalpy and slightly larger pre-exponential factor than those reported in Ref. [218], which is within the error margin of the applied sputter-depth profiling technique (see figure 5.7).

The impurity diffusion coefficient of Ag in Pd is about three orders of magnitude smaller than the self-diffusion coefficient of Ag in Ag, but exhibits the same activation enthalpy of 1.9 eV. No literature values exist for Ag impurity diffusion in pure Pd and the here deduced impurity diffusion coefficient of Ag in Pd can only be compared with extrapolated literature values, as follows. An approximated impurity diffusion coefficient of Ag in pure Pd can be obtained by extrapolating the values given in Ref. [195] for the self diffusion coefficient of Ag in $Ag_{1-x}Pd_x$ solid solutions with $x < 22$ at.% to pure Pd. Noteworthy, the thus obtained values for the impurity diffusion coefficients of Ag in Pd as function of temperature deviate only slightly from the here determined experimental values (see figure 5.7). Hence it follows that in contrast to Ag self-diffusion in Ag (cf. Ref. [218]) the divacancy contribution to impurity diffusion of Ag in Pd is small, which is compatible with the negligible contribution of divacancies to Pd diffusion in Pd [233].

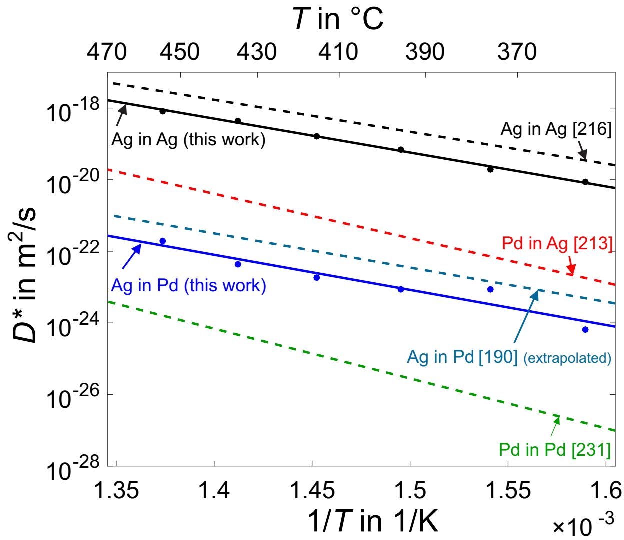

Figure 5.7: The self-diffusion coefficients of Ag in Ag and Ag in Pd, as determined in this work (dots and full lines). Literature data for the self-diffusion coefficients of Ag in Ag [218], Ag in Pd [195], Pd in Ag [215] and Pd in Pd [233] have been shown as well (dashed lines). The data from Refs. [195, 215, 233] were extrapolated to the annealing temperatures applied in this study. The corresponding activation enthalpies and pre-exponential factors have been listed in table 5.2. Note that the impurity diffusion coefficient of Ag in Pd presented here is extrapolated from data in Ref. [195] for (bulk) $Ag_{1-x}Pd_x$ solid solutions with $x < 22$ at.%.

Table 5.2: Activation enthalpy, Q, and pre-exponential factor, D_0, of the self-diffusion and impurity diffusion coefficients.

	Q_{1V} in eV	Q_{1V} in kJ/mol	$D_{0,1V}$ in m²/s	Q_{2V} in eV	Q_{2V} in kJ/mol	$D_{0,2V}$ in m²/s	Reference
Ag in Ag	1.77	171	$5.44 \cdot 10^{-6}$	2.46	237	$3.96 \cdot 10^{-6}$	[218]
	1.88 ± 0.03	181 ± 3	$9.01^{+9}_{-3} \cdot 10^{-6}$				this study
Ag in Pd	1.94 ± 0.15	187 ± 15	$4.19^{+331}_{-3} \cdot 10^{-9}$				this study
	1.90	183	$7.42 \cdot 10^{-9}$				[195]
Pd in Ag	2.20	212	$4.07 \cdot 10^{-5}$	2.89	279	$2.77 \cdot 10^{-2}$	data from [215]
Pd in Pd	2.76 ± 0.03	266 ± 3	$2.05^{+0.5}_{-0.4} \cdot 10^{-5}$				[233]

5.3.5 Application of the Nernst-Planck equation

In the absence of vacancy sources and sinks the equilibrium vacancy concentration cannot be maintained during substitutional interdiffusion (cf. section 5.3.2). Then the chemical diffusion coefficient should be described according the Nernst-Planck equation [46–50]:

$$\widetilde{D}_{\mathrm{NP}} = \frac{D_{\mathrm{Ag}} D_{\mathrm{Pd}}}{x_{\mathrm{Ag}} D_{\mathrm{Ag}} + x_{\mathrm{Pd}} D_{\mathrm{Pd}}}. \tag{5.9}$$

In the following it is investigated, if the measured sputter-depth profiles can be described on this basis.

As discussed in section 5.3.2 (see also appendix 5.A.1), the chemical diffusion coefficient is dominated by the large intrinsic diffusion coefficient of Ag, if the Darken-Manning treatment is adopted. If the Nernst-Planck treatment is adopted, the chemical diffusion coefficient is dominated by the small intrinsic diffusion coefficient of Pd (see appendix 5.A.1). Thus it is not possible to adopt the same fitting parameters, as applied adopting the Darken-Manning treatment. It is now necessary to fit the impurity diffusion coefficient of Pd, i.e. the self-diffusion coefficient of Pd in Pd and the impurity diffusion coefficient of Pd in Ag and adopting the self-diffusion coefficient of Ag in Ag and the impurity diffusion coefficient of Ag in Pd from extrapolated literature data. Since no literature data is available for the impurity diffusion coefficient of Ag in Pd at the low annealing temperatures applied in this study, the impurity diffusion coefficients of Ag in Pd as obtained from the fit applying the Darken-Manning equation has been used here. Note that the physical meaning of the intrinsic diffusion coefficients is the same for the Darken-Manning treatment and the Nernst-Planck treatment.

The resulting concentration-dependent chemical diffusion coefficient, as obtained here by adopting the Nernst-Planck treatment, can be compared with that obtained in section 5.3.3 by adopting the Darken-Manning treatment (see figure 5.8). Despite the entirely different fitting parameters (i.e. the intrinsic diffusion coefficient of Ag for the Darken-Manning treatment and the intrinsic diffusion coefficient of Pd for the Nernst-Planck treatment) the resulting concentration-dependent chemical diffusion coefficients are very similar for $x_{\mathrm{Pd}} > 0.5$ and differ only modestly for $x_{\mathrm{Pd}} < 0.5$, which has also been observed in an interdiffusion study for Au/Ag bilayers [218].

However, the fitted self-diffusion coefficients of Pd in Pd (applying the Nernst-Planck treatment) are two orders of magnitude larger than as expected from literature values. Hence, as expected (cf. section 5.3.2), the Nernst-Planck equation is not applicable to describe the measured concentration-depth profiles; the Darken-Manning equation has to be applied.

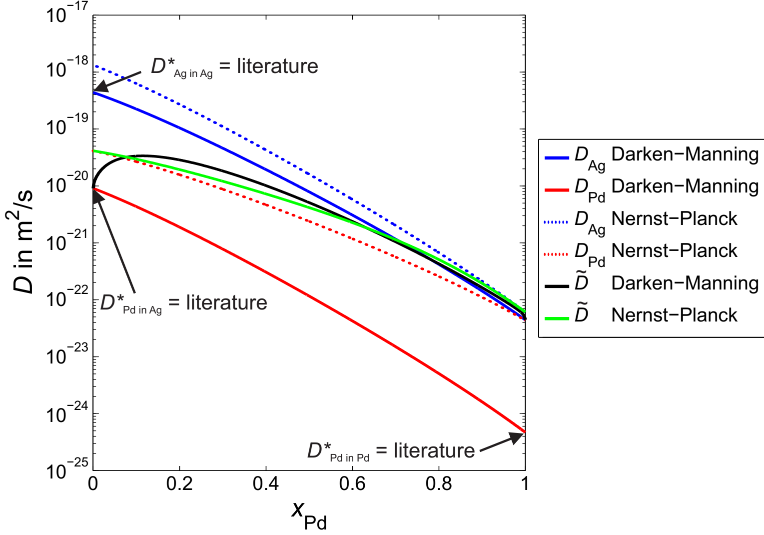

Figure 5.8: Concentration-dependence of the intrinsic and chemical diffusion coefficient as determined in this work, applying either the Darken-Manning (D-M) treatment or the Nernst-Planck (N-P) treatment for a Pd/Ag bilayer annealed at 435 °C for 15 min. The determined chemical diffusion coefficients, obtained applying the D-M treatment or the N-P treatment, are very similar for $x > 0.5$ and differ only modestly for $x < 0.5$. A good agreement of the deduced self and impurity diffusion coefficients with extrapolated literature data is obtained when the D-M treatment is applied. If the N-P treatment is applied the deduced self-diffusion coefficient of Pd in Pd is about two orders of magnitude larger than that expected from extrapolated literature values [233]. Note that the fitting parameters for the D-M treatment and the N-P treatment are different (see discussion in section 5.3.5).

5.3.6 Stress development during interdiffusion

No conclusive experimental study of the interrelation of stress and interdiffusion is available, apart from work on the effect of a pure hydrostatic state of stress on diffusion (see e.g. Refs [28] and [27]). This in particular also holds for previous studies on interdiffusion in Pd/Ag thin films [10, 236–239]. This is mainly, but not only, caused by the occurrence of pronounced microstructural changes during diffusion annealing, especially in nano-crystalline

materials: grain growth, related with DIGM [22–26] and DIR [7, 9, 10, 239] occur. The decrease of grain-boundary density is associated with the reduction of excess free volume, as present in a grain boundary for a polycrystalline thin film attached onto a (rigid) substrate, and leads to the emergence of a tensile stress component parallel to the film surface [240]. Such stress changes mask the stress change intrinsically caused by the interdiffusion process and the corresponding compositional changes. In order to minimise microstructural changes, such as grain growth, during diffusion annealing, single-crystalline specimens have been applied in the present study.

Indeed, no microstructural changes could be detected at gentle annealing conditions (see section 5.3.1) (relevant for the experiments dealt with in sections 5.3.2-5.3.5); microstructural changes, such as Ag segregation to the C/Pd interface, occur only at *much prolonged* diffusion annealing treatments (see appendix 5.C), as unavoidable for the in-situ XRD stress measurements (cf. section 5.2.3).

Evolution of the X-ray diffraction profiles

For the as-prepared specimens the as-measured corresponding diffraction profiles of Ag and Pd are well separated (see the blue curves in figures 5.9a and b). Upon diffusion annealing, the intensity maxima of the Ag and Pd diffraction profiles decrease (see figure 5.9d). At the same time the Ag diffraction profiles become visibly asymmetric: a shoulder develops at the high angle side, which increases with time (see figure 5.9c). The development of this intensity shoulder is indicative of the formation of an Ag rich $Ag_{1-x}Pd_x$ solid solution upon interdiffusion (the lattice parameter of Ag decreases upon dissolving Pd [228]). Since Pd diffusion in Ag is much faster than Ag diffusion in Pd (see section 5.3.2 and figure 5.5), the formation of an Ag rich $Ag_{1-x}Pd_x$ solid solution is much more pronounced than the formation of a Pd rich $Ag_{1-x}Pd_x$ solid solution at the interface of the diffusion couple (see the determined concentration-depth profile in figure 5.4b) and consequently, no such intensity shoulder develops at the lower angle side of the Pd diffraction profile (the lattice parameter of Pd increases upon dissolving Ag [228]). Only the maximum intensity of the Pd diffraction profile decreases with increasing annealing time, because of the loss of Pd from the originally pure Pd sublayer by diffusion of Pd into the Ag sublayer (see figure 5.9d). The maximum intensity of the Ag diffraction profile generally decreases with increasing annealing time due to the loss of Ag by diffusion from the initially pure Ag layer in the Pd sublayer. Contributions like stress development, stress relaxation and small changes in the specimen alignment during thermal cycling cause intensity fluctuations, which are more pronounced for the Ag

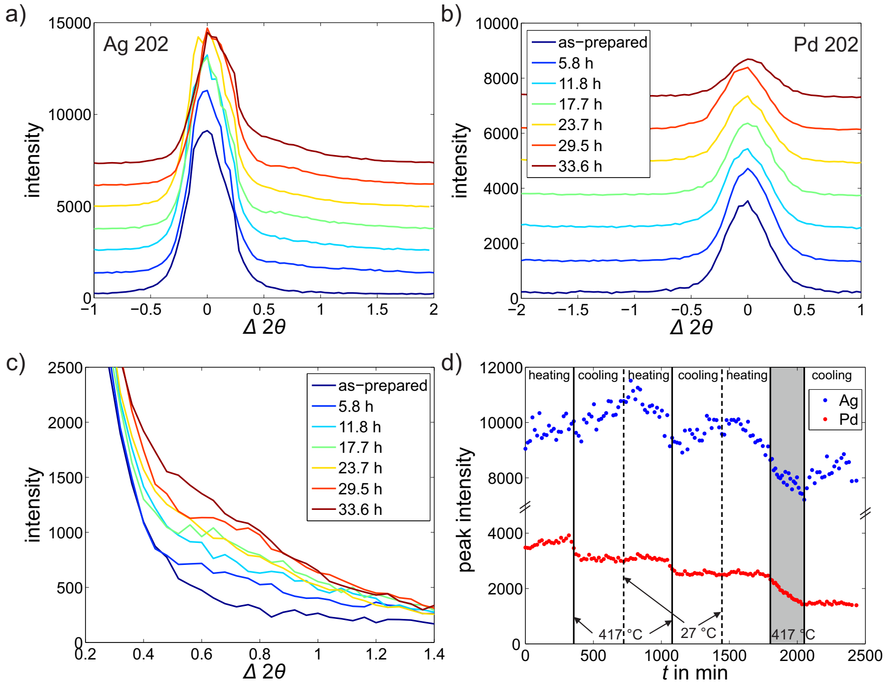

Figure 5.9: Peak evolution of a) the Ag 202 diffraction profile as-measured in the diffraction-angle range of $2\theta = 62.7° - 66.5°$, $\psi = \phi = 45°$ and b) the Pd 202 diffraction profile as-measured in the diffraction-angle range of $2\theta = 66.1° - 70.1°$, $\psi = \phi = 45°$, during thermal cycling and isothermal annealing at 417 °C (cf. section 5.2.3) of an Pd/Ag bilayer. c) During thermal cycling, a shoulder develops at the high angle side of the Ag 202 diffraction profile, while d) only a decrease of the maximum intensity of the Pd 202 diffraction profile can be observed at annealing temperatures between 400 °C and 417 °C. Note that a small change in the alignment of the specimen due to thermal expansion during thermal cycling changes the maximum intensity, which is more pronounced for the sharper Ag 202 diffraction profile (FWHM $\approx$ 0.30°) than the broader Pd 202 diffraction profile (FWHM $\approx$ 0.37°). a-c) All peaks have been shifted to have their maximum at the same 2θ value (to compensate for the peak shift due to changing in-plane film stress) for better comparison ($\Delta 2\theta$ indicates the difference of the diffraction angle with respect to the position of the peak maximum). In addition an ordinate shift for the different annealing times has been applied in a) and b). The indicated times correspond with the total, cumulative times of annealing (first cycle, second cycle and third cycle with isothermal annealing at 417 °C; cf. section 5.2.3).

diffraction profile than for the Pd diffraction profile (which corresponds with a less distinct mosaicity of the Ag sublayer; cf. section 5.3.1).

The here observed trends in the development of the XRD diffractogram during interdiffusion are in agreement with model calculations of the evolution of the X-ray diffraction profiles upon diffusion annealing [241–243] (see appendix 5.D and Ref. [10]). It is emphasised here that the development of the shoulder at the high angle side of the Ag diffraction profiles is *not* associated with the formation of new grains of some preferred composition, as it has been observed in an interdiffusion study of *polycrystalline* Pd/Ag thin films [10]. The development of this intensity shoulder is exclusively the result of the establishment of an asymmetric concentration-depth profile due to the pronounced concentration dependence of the chemical diffusion coefficient and not due to the formation of new grains (see section 5.2.2).

In-plane stress evolution during thermal cycling

The measured evolution of the equibiaxial in-plane film stresses, $\sigma_{||}$ (cf. Eq. 5.1a), and of the strain-free lattice parameters, a_0 (cf. Eq. 5.1b), in each sublayer during thermal cycling are shown in figure 5.10. Note that the extent of interdiffusion during thermal cycling is negligible small at temperatures below 400 °C (e.g. cf. figure 5.9d) and consequently interdiffusion does not contribute significantly to the stress evolution during thermal cycling (with a maximum temperature of 417 °C).

Ag sublayer The as-deposited Ag sublayer in the Pd/Ag bilayer exhibits an in-plane tensile stress of 82 MPa. Upon heating, the stress in the Ag sublayer follows the thermoelastic line[7] up to a temperature of 100 °C (see blue line in figure 5.10a) while the stress in the Ag sublayer decreases to about 0 MPa. Upon further temperature increase non-reversible stress relaxation mechanisms such as thermally activated dislocation glide (and possibly also climb) [245–249], become operative and the stress becomes less negative than predicted by the thermoelastic line. At a temperature of about 300 °C an about constant maximum compressive stress of −138 MPa is established: stress build-up by thermal misfit and stress relaxation appear to establish a stationary state. Upon cooling the specimen from 417 °C back to room

[7] In order to calculate the strain/stress of the single-crystalline Ag sublayer confined by the rigid Si substrate, the temperature-dependent single-crystalline elastic constants of Ag [244] and the temperature-dependent thermal expansion coefficients of Ag [221] and Si [221] have been applied. Note that due to the consideration of the temperature dependence of the thermal expansion coefficients, the expected thermal stress is not a linear function of temperature.

temperature, the stress curve follows the thermoelastic line down to a temperature of 125 °C and a tensile stress of 185 MPa. Upon further cooling, the stress becomes that large that relaxation by dislocation glide [245] becomes feasible and a slightly downward curvature from the thermoelastic line is observed; the tensile stress upon returning at room temperature is 232 MPa. The shape of the second thermal cycle (red curve in figure 5.10a) can be discussed on the same basis as the first thermal cycle (blue curve in figure 5.10a). The thermoelastic line is followed upon heating until a compressive stress develops in the Ag sublayer. Since the starting tensile stress at room temperature for the second cycle is higher than for the first cycle, the temperature, at which the tensile to compressive transition occurs for the Ag sublayer is higher for the second cycle: 220 °C as compared to 100 °C for the first cycle. Compatible with the discussion of the first thermal cycle, the maximum compressive stress at 417 °C in the second cycle (−120 MPa) is about equal to that of the first cycle (−138 MPa). During subsequent isothermal annealing for ≈ 4.4 h at 417 °C in the third thermal cycle (no such isothermal anneals were performed in the first and second thermal cycles; cf. section 5.2.3), the compressive stress at 417 °C continuously relaxes from the initial value of −115 MPa to −80 MPa (see figure 5.10e), while the averaged strain-free lattice parameter of the Ag sublayer decreases as a result of interdiffusion (dissolution of Pd into the Ag sublayer) (see figure 5.10f).

Pd sublayer The as-deposited Pd sublayer in the Pd/Ag bilayer exhibits an in-plane tensile stress of 385 MPa. Upon heating, the stress in the Pd sublayer follows the thermoelastic line[8] up to a temperature of 350 °C while the film stress decreases to about 20 MPa. Upon further temperature increase non-reversible stress relaxation mechanisms become operative (see discussion of the Ag sublayer) and the stress deviates from (decreases less than predicted by) the thermoelastic line. The stress reached at 417 °C equals −19 MPa. During subsequent cooling to room temperature the stress change fully complies with the thermoelastic line, leading to a tensile stress of 430 MPa upon returning at room temperature. The following second thermal cycle can be fully described by thermoelastic behaviour upon annealing and subsequent cooling. During the isothermal annealing for ≈ 4.4 h at 417 °C in the third cycle, only a very small stress relaxation is observed: the compressive stress decreases from −17 MPa at the beginning of isothermal annealing to −14 MPa at the end of isothermal annealing (see figure 5.10e). During the isothermal annealing no change of the strain-free lattice parameter occurs.

[8] In order to calculate the strain/stress of the single-crystalline Pd sublayer confined by the rigid Si substrate, the temperature-dependent single-crystalline elastic constants of Pd [244] and the temperature-dependent thermal expansion coefficients of Pd [221] and Si [221] have been applied.

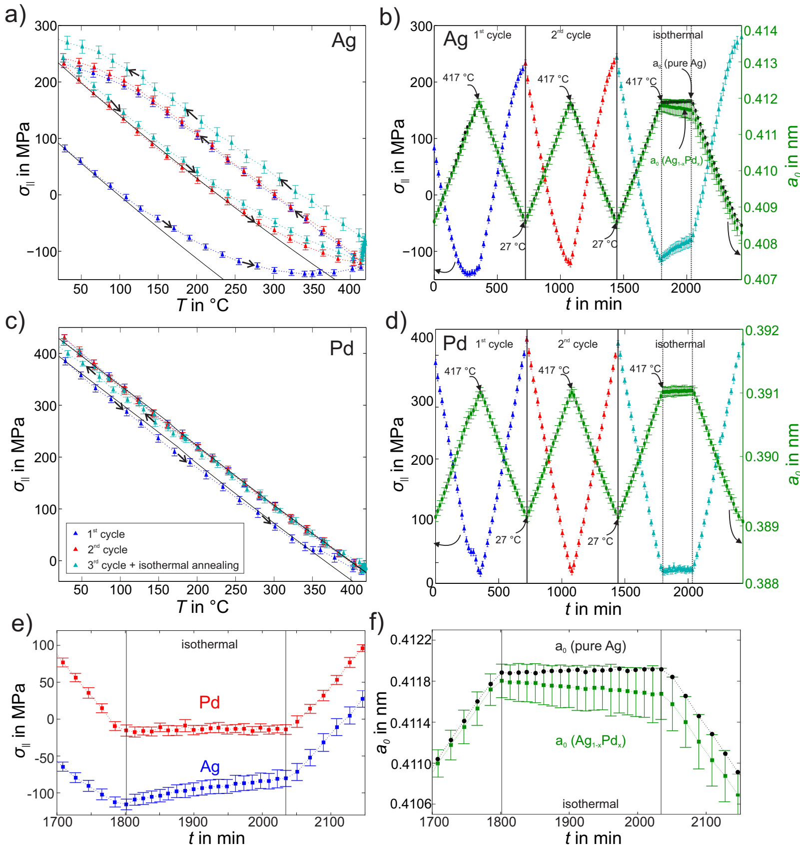

Figure 5.10: Evolution of the stress parallel to the surface, $\sigma_{||}$, a) in the Ag sublayer and c) in the Pd sublayer of the Pd/Ag bilayer as function of the annealing temperature. The stress parallel to the surface as well as the strain-free lattice parameter of b) the Ag sublayer and d) the Pd sublayer in the Pd/Ag bilayer as function of the annealing time. The results shown in a)-d) have been obtained during thermal cycling (cf. section 5.3.6): The first thermal cycle has been indicated in dark blue, the second cycle in red and the last cycle, including the isothermal annealing at 417 °C for 4 h, in light blue. The theoretically expected thermal stress due to the different thermal expansion coefficients of the material and the substrate are shown as black lines, for the heating in the first and second cycle, in a) and c). e) Stress evolution in the Ag sublayer and the Pd sublayer during isothermal annealing at 417 °C. f) During isothermal annealing and subsequent cooling the determined strain-free lattice parameter of the Ag sublayer (green circles) deviates from the expected strain free lattice parameter (becomes smaller than) as expected for pure Ag (black circles) due to intermixing with Pd.

Discussion of stress evolution during interdiffusion

During interdiffusion, different mechanisms may contribute to the overall stress change in the individual sublayers [22–26]:

(i) Difference in molar volume: If the molar volume of the components is different, a compressive compositional stress contribution arises in the sublayer composed mainly of the component with the smaller molar volume and correspondingly a tensile compositional stress contribution arises in the sublayer composed mainly of the component with the larger molar volume. The effect of this compositional stress on interdiffusion has been modelled by the theory of Larché and Cahn [60–62] on the basis of a network solid, i.e. no lattice sites are generated or annihilated during interdiffusion (see section 5.3.7). Since Pd exhibits a smaller molar volume than Ag, the substitution of an Ag atom with a Pd atom upon interdiffusion leads to a tensile compositional stress component in the Ag sublayer and, vice versa, the substitution of a Pd atom with an Ag atom leads to the build-up of a compressive compositional stress component in the Pd sublayer.

(ii) Difference in atomic fluxes: For a system which shows asymmetric substitutional interdiffusion, the equilibrium vacancy concentration-depth profile might not be maintained upon diffusion annealing. If no vacancy sources and sinks are operative, the sublayer composed of the component diffusing faster in the sublayer composed (mainly) of the other component becomes vacancy supersaturated, whereas the sublayer composed of the component diffusing slower in the sublayer composed of (mainly) the other component becomes vacancy depleted. Since the atomic volume of an atom is generally distinctly larger than the volume of a vacancy, a tensile stress component is induced in the sublayer becoming supersaturated with vacancies and a compressive stress component is induced in the sublayer becoming depleted with vacancies. In the present case Pd diffuses faster in Ag than Ag in Pd (see figures 5.4b, 5.5 and 5.7; i.e. $D^*_{\mathrm{Ag\ in\ Pd}} < D^*_{\mathrm{Pd\ in\ Ag}}$). Therefore, a tensile stress component develops in the Pd sublayer and a compressive stress component develops in the Ag sublayer.

Hence, on the basis of the above discussion it could be suggested that the mechanisms (i) and (ii) generate (to an unknown extent (see what follows)) compensating stress components in each of both sublayers.

Due to the considerable lattice mismatch of Ag and Pd the Pd/Ag bilayer is characterised by a semi-coherent interface with a relatively high density of misfit dislocations (cf. see figure 5.2c and section 5.2.2). These misfit dislocations can serve as vacancy sources and sinks upon interdiffusion. The excess vacancies introduced in the Pd sublayer, due to the fast diffusion of Pd atoms into the Ag layer (see above), as compared to the slow diffusion

of Ag atoms into the Pd sublayer, can be annihilated by positive climb of such misfit dislocations [225] into the Pd sublayer. This positive climb of the misfit dislocations causes the development of a (further, see (ii) above) tensile stress component in the Pd sublayer. The creation of vacancies in the Ag sublayer, which is necessary to maintain the equilibrium vacancy concentration, due to the discussed asymmetric interdiffusion behaviour, can occur by negative climb of misfit dislocations. This negative climb of misfit dislocations could cause the development of a compressive stress component in the Ag sublayer. However, since the volume diffusion length of Ag in Ag is of the order of the Ag sublayer thickness at the annealing conditions applied in this study (the volume diffusion length of Pd in Pd is orders of magnitude smaller: < 0.1 nm), it is more likely that vacancies generated at defects in the Ag layer or at the Ag/substrate interface diffuse to the Pd/Ag interface and establish and maintain the desired equilibrium vacancy concentration in the Ag sublayer.

On the basis of the above discussion, it is expected that in the stage where appreciable interdiffusion occurs (i.e. in the thermal cycle experiments not before a temperature above 400 °C occurs) (a) diffusion annealing induces a tensile compositional stress component in the Ag sublayer without a (compressive stress) contribution due to a difference in atomic fluxes, due the establishment and maintenance of the equilibrium vacancy concentration in the Ag sublayer by the generation of vacancies at defects in the Ag sublayer, and (b) diffusion annealing induces a compressive compositional stress component in the Pd sublayer as well as a tensile stress component due to the annihilation of excess vacancies by positive climb of misfit dislocations originally located at the Pd/Ag interface in order to establish and maintain the equilibrium vacancy concentration.

It now can be concluded that in the temperature range where interdiffusion in the Pd/Ag bilayer takes place, compressive stress build-up occurs in the Ag sublayer as a consequence of thermal misfit. The build-up of a tensile compositional stress (due to replacement of Ag atoms by Pd atoms) would occur in the temperature range where stress relaxation mechanism operate in the Ag sublayer ($T > 400$ °C) and thus are not apparent in the measured stress. The observed relaxation of the measured compressive stress (as revealed by the stress measurements at $T > 400$ °C and at the isothermal annealing temperature of 417 °C; see figure 5.10b) can be ascribed to compositional stress and predominantly to microstructural changes associated with dislocation climb and glide (power-law creep by climb-plus-glide [250]) and also out-diffusion of Ag through domain boundaries and holes in the Pd layer (see microstructural characterisation after prolonged diffusion annealing in section 5.C).

For the Pd sublayer, in the temperature range where interdiffusion in the Pd/Ag bilayer takes place, a compressive thermal stress component, a compressive compositional stress component (due to replacement of Pd atoms by Ag atoms) and a tensile stress component (due to the introduction of excess vacancies and their annihilation (by positive climb of misfit dislocations)) can occur. The latter component can contribute to the decrease of the measured compressive stress at $T > 400$ °C and during isothermal annealing at 417 °C (see figure 5.10d).

Since the self-diffusion coefficient of Ag in Ag is about six orders of magnitude larger than the self-diffusion coefficient of Pd in Pd, any stress relaxation may proceed much faster in the Ag sublayer than in the Pd sublayer. Indeed at the (highest) isothermal annealing temperature of 417 °C an only small decrease of compressive stress was observed in the Pd sublayer, but a distinct decrease of compressive stress occurred in the Ag sublayer (see figure 5.10e).

5.3.7 Effect of stress on interdiffusion

Effect of compositional strain

Due to the different atomic sizes of Pd and Ag, compositional strain can develop upon interdiffusion (mechanism (i) discussed in section 5.3.6). The effect of compositional strain on interdiffusion has been described under the assumption that no lattice sites are generated or annihilated during interdiffusion (such solids are called “network” solids) [60–62]. According to this model, the compositional strain changes the gradient of the diffusion potential (the so-called diffusion potential replaces the role of the chemical potential in a crystalline solid; the chemical potential can only be used in a stress-free or only hydrostatically stressed state). The concentration-depth profile in the Pd/Ag bilayer (assuming that it can be considered as a network solid) can be calculated according to [251]

$$
\begin{aligned}
\frac{\partial x_{\mathrm{Ag}}}{\partial t} = \frac{\partial}{\partial z}\Bigg[\widetilde{D}\Bigg(1 + \frac{2\eta^2 x_{\mathrm{Ag}}(1-x_{\mathrm{Ag}})V'}{\Phi RT}\cdot \\
[(x_{\mathrm{Ag}} - x_0)(Y_{\mathrm{Ag}} - Y_{\mathrm{Pd}}) + Y]\Bigg)\frac{\partial x_{\mathrm{Ag}}}{\partial z}\Bigg],
\end{aligned}
\tag{5.10}
$$

where x_{Ag} is the local concentration of Ag, x_0 is the local concentration of Ag before diffusion annealing, t is the diffusion time, z is the location (depth), η denotes the local difference in partial molar volumes, $\overline{V}$, of the components $\eta = (\overline{V}_{\mathrm{Pd}} - \overline{V}_{\mathrm{Ag}})/(3V')$, where V' is the molar volume of the

reference state (i.e. the local molar volume before diffusion annealing), Φ represents the thermodynamic factor, Y_{Ag} and Y_{Pd} are the biaxial moduli of pure Ag and Pd, respectively ($= c_{11} + c_{12} - 2 \cdot c_{12}/c_{11}$, with c_{11} and c_{12} as the elements of the stiffness tensor of the single crystal) of pure Ag and Pd, respectively and Y denotes the local biaxial modulus at the local concentration x_{Ag}, i.e. $Y = x_{\mathrm{Ag}}Y_{\mathrm{Ag}} + (1 - x_{\mathrm{Ag}})Y_{\mathrm{Pd}}$.

Adopting this version of Fick's second law and adopting the fitting procedure for the measured sputter-depth profiles as described in section 5.3.2, the obtained, fitted values of the self-diffusion coefficients of Ag in Ag are the same, within error limits, as those obtained without considering such compositional strain. The impurity diffusion coefficients of Ag in Pd are a factor of two to eight larger if compositional strain, as described by equation 5.10, is considered (see figure 5.11).

However, as made likely before (cf. section 5.3.6) the approach by Larché and Cahn is likely not applicable for in any case the system Pd/Ag because the number of lattice sites clearly is not conserved upon interdiffusion (see discussion in section 5.3.6). The calculation in this section is only meant to demonstrate that the influence of compositional strain on the diffusion coefficients presented in this work is very limited.

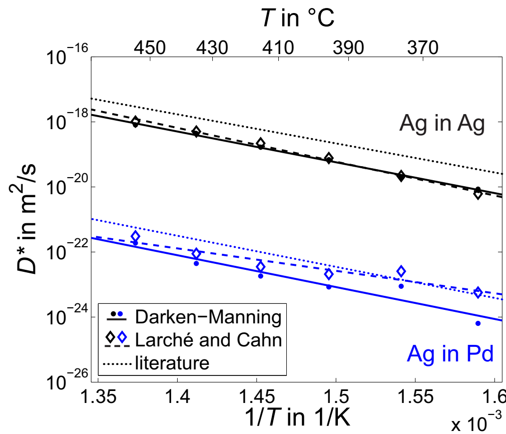

Figure 5.11: Comparison of the self-diffusion coefficient of Ag in Ag and the impurity diffusion coefficient of Ag in Pd as obtained from the present experimental data using the procedure presented in this paper, adopting the Darken-Manning treatment, (see section 5.3.2) and as obtained if the effect of compositional strain, as described by the theory of Larché and Cahn for a network solid [60–62], is Incorporated. Literature data for the self-diffusion of Ag in Ag (cf. Ref. [218]) and the impurity diffusion coefficient of Ag in Pd [195] (extrapolated to the temperature range of this study) are shown as well.

Effect of hydrostatic stress component

It can be suggested that the effect of a planar state of stress on the interdiffusion in the Pd/Ag bilayer can be approximately assessed by considering its equivalent hydrostatic stress component: $p = 2/3\sigma_{||}$. The effect of hydrostatic pressure, p, on the diffusion coefficient, D, is usually described according to [50]

$$\left(\frac{\partial \ln D}{\partial p}\right)_T = -\frac{\Delta V}{RT}, \tag{5.11}$$

where ΔV is the activation volume.

For Ag self-diffusion, the activation volume in the temperature range used in this study is $0.66\,\Omega_{\mathrm{Ag}}$ [194] (atomic volume, $\Omega_{\mathrm{Ag}} = 1.03 \cdot 10^{-5}$ m^3/mol). Taking the activation volume of Pd impurity diffusion in Ag as equal to that for Ag self-diffusion[9] and using the hydrostatic stress component equivalent to the equibiaxial planar state of stress in the Ag sublayer at the beginning of the isothermal annealing at 417 °C (see section 5.3.6), ($p = 2/3 \cdot -115$ MPa), the effect of the planar stress on the diffusion coefficient can be crudely estimated. It follows that the impurity diffusion coefficients of Pd in Ag and the self-diffusion coefficients of Ag in Ag are about 18 % larger if the compressive film stress is considered. This difference is within the experimental error range for the diffusion coefficients presented in this work (cf. table 5.2).[10]

The planar stress in the Pd sublayer at the beginning of isothermal annealing at 417 °C (see section 5.3.6) is negligibly small (-17 MPa). No activation volumes for self-diffusion in Pd have been reported. When an activation volume of $0.66\,\Omega_{\mathrm{Pd}}$, ($\Omega_{\mathrm{Pd}} = 8.86 \cdot 10^{-6}$ m^3/mol) for the impurity diffusion of Ag in Pd is assumed, the deduced impurity diffusion coefficients are less than 2 % larger than the values presented in this work (see figure 5.7).

5.4 Conclusions

- The concentration-dependent chemical diffusion coefficient for Pd/Ag diffusion couples, the self-diffusion coefficient of Ag in Ag and the impurity coefficient of Ag in Pd have been determined in the temperature range of 356 °C to 455 °C, corresponding to a diffusion length of about

[9] Note that the activation volume of Pd impurity diffusion is expected to be different from the activation volume for Ag self-diffusion due to the different atomic sizes and atom-vacancy interactions.

[10] It is noted that the agreement with the self-diffusion coefficients of Ag in Ag as reported in the literature (as determined from bulk diffusion couples, which are likely not affected by stresses) increases if the effect of compressive film stress is considered (cf. figure 5.7).

10 nm, utilising single-crystalline Ag/single-crystalline Pd bilayers, applying AES sputter-depth profiling.

- The concentration-depth profiles after diffusion annealing can only be described by applying the Darken-Manning equation. Adopting the Nernst-Planck equation leads to physically unreasonable self-diffusion coefficients. The equilibrium vacancy concentration is maintained by the presence of defects allowing vacancy generation and annihilation, as misfit dislocations, originally present at the interface of the Pd/Ag sinlge-crystalline diffusion couples.

- Due to the similarity of the strong concentration dependences of the intrinsic diffusion coefficients of Ag and Pd, the chemical diffusion coefficient varies only by about three orders of magnitude over the whole composition range, despite the large difference of six orders of magnitude in the self-diffusion coefficients of Ag in Ag and Pd in Pd.

- The deduced impurity diffusion coefficients of Ag in Pd indicate that the contribution of divacancies to Ag diffusion in Pd is small.

- Upon diffusion annealing a tensile compositional stress can develop in the Ag sublayer. In addition to the operating stress relaxation mechanisms which are promoted by the very high self-diffusion of Ag, thereby an (initial) compressive state of thermal stress decreases significantly.

- Upon diffusion annealing a compressive compositional stress can develop in the Pd sublayer. A minor tensile stress component, compensating in a minor way the (initial) compressive thermal stress and the compressive compositional stress, develops by the positive climb of misfit dislocations (thereby establishing the equilibrium vacancy concentration in the Pd sublayer). (Other) Relaxation mechanisms do not operate significantly in the Pd sublayer.

- The effect of compositional stress as predicted by the Larché-Cahn treatment for network solids, and the effect of a hydrostatic component of stress equivalent to the prevailing planar state of stress are vanishingly small (i.e. of about the experimental accuracy of the diffusion-coefficient values determined in this work).

Acknowledgements

We gratefully acknowledge Dipl.-Ing. Frank Thiele and Reinhart Völker (both with MPI-IS) for Pd, C, and Si_3N_4 thin film deposition by magnetron sputtering, Dipl.-Ing. Bernhard Fenk and Dipl.-Ing. Peter Kopold (both with MPI-FKF) for TEM specimen preparation and assistance with the TEM investigation, as well as Dr. Sabine Haag (formerly with MPI-IS) for providing a script to evaluate the *in-situ* XRD data.

Appendix 5.A Determination of the concentration-dependent chemical diffusion coefficient

For the determination of the concentration-dependent chemical diffusion coefficient from the measured sputter-depth profiles some assumptions, indicated in section 5.3.2, had to be made. In the following, the impact of these assumptions on the obtained results is investigated.

5.A.1 Fitting of the impurity diffusion coefficients of Ag in Pd and of Pd in Ag

The self-diffusion coefficients of Ag [218] and Pd [233] are well known at higher temperatures. Extrapolation of these data down to the low annealing temperatures applied in this study has been performed. Choosing these self-diffusion coefficients as fixed parameters for the calculation of the concentration-depth profile by the MRI forward calculation approach (see section 5.3.2), while fitting the unknown impurity diffusion coefficients of Ag in Pd and of Pd in Ag, then appears to be the best approach. However, fitting of these two impurity diffusion coefficients, while adopting the self-diffusion coefficient of Ag in Ag [218] and the self-diffusion coefficient of Pd in Pd [233] from literature, results in a physically unrealistic concentration-dependence of the chemical diffusion coefficient by applying either the Darken-Manning treatment or the Nernst-Planck treatment (see figure 5.12), as discussed in the following (details about the different diffusion models can be found in Ref. [218]):

If the Darken-Manning equation is applied, the chemical diffusion coefficient changes over three orders of magnitude in the concentration range of $0 < x_{\mathrm{Pd}} < 0.01$. Similarly, if the Nernst-Planck equation is applied the chemical diffusion coefficient changes over almost four orders of magnitude in the concentration range of $0.99 < x_{\mathrm{Pd}} < 1$. The features of the

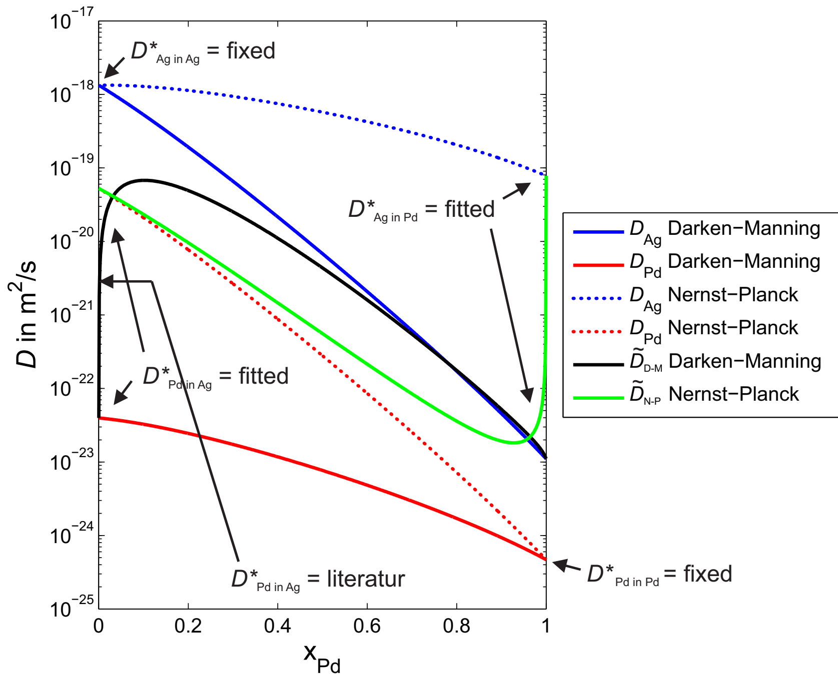

Figure 5.12: Concentration-dependence of the intrinsic and chemical diffusion coefficient, applying either the Darken-Manning treatment or the Nernst-Planck treatment for a specimen annealed at 435 °C for 15 min. The self-diffusion coefficients of Ag in Ag [218] and of Pd in Pd [233] have been adopted from extrapolated literature data, while the impurity diffusion coefficients of Ag in Pd and of Pd in Ag have been fitted according to the MRI forward calculation procedure.

concentration-depth profile, resulting from these large changes in the chemical diffusion coefficient in these tiny concentration ranges cannot be resolved by the applied sputter-depth profiling technique due to the sputter-induced broadening of the measured intensity-depth profile.

If the Darken-Manning treatment is applied, a variation of the impurity diffusion coefficient of Pd in Ag has only a minor effect on the overall concentration-dependence of the chemical diffusion coefficient, due to the dominating influence of the intrinsic diffusion coefficient of Ag. Similarly, if the Nernst-Planck treatment is applied a variation of the impurity diffusion coefficient of Ag in Pd has only a minor effect on the concentration-

dependence of the chemical diffusion coefficient. Note that the measured intensity-depth profiles cannot be described with larger (as shown in figure 5.12) impurity diffusion coefficients of Pd in Ag (Darken-Manning treatment) or smaller (as shown in figure 5.12) impurity diffusion coefficients of Ag in Pd (Nernst-Planck treatment) while adopting the self-diffusion coefficients of Ag in Ag and Pd in Pd from extrapolated literature data. The description of the measured sputter-depth profiles is only possible due to the special features induced by the physically unreasonably large concentration-dependence of the chemical diffusion coefficient.

In conclusion, fitting the impurity diffusion coefficients of Ag in Pd and Pd in Ag, while adopting the self-diffusion coefficient of Ag in Ag and Pd in Pd from literature, is not possible with the applied sputter-depth profiling technique in the system Pd/Ag due to the small sensitivity of the technique for the determination of the smaller intrinsic diffusion coefficient (D_{Pd}), which is a result of the large difference in the intrinsic diffusion coefficients.

5.A.2 No divacancy contribution to the diffusion mechanism of Pd in Ag

The impurity diffusion coefficients of Ag in Pd and of Pd in Ag cannot be used both as fitting parameters due the lack of sensitivity for the much smaller intrinsic diffusion coefficient of Pd due to the dominating contribution of the large intrinsic diffusion coefficient of Ag to the chemical diffusion coefficient (Darken-Manning case) (see section 5.A.1). Hence, the self-diffusion coefficient of Ag in Ag and the impurity diffusion coefficient of Ag in Pd have been used as fitting parameters, while the impurity diffusion coefficient of Pd in Ag and the self-diffusion coefficient of Pd in Pd have been adopted from extrapolated literature data pertaining to bulk specimens (see section 5.3.2).

For the determination of the concentration-dependent chemical diffusion coefficient, the impurity diffusion coefficient of Pd in Ag has to be known in the low temperature range of this study. Therefore, an estimation of the possible contribution of divacancies to the diffusion mechanism at higher annealing temperatures was made and the deduced kinetic data were used for the fitting at the low temperatures of this study (see section 5.3.2). However, the true extent of the divacancy contribution to impurity diffusion of Pd in Ag is unknown and thus the applied crude estimation of the divacancy contribution to the impurity diffusion of Pd in Ag at higher temperatures (see section 5.3.2) might not be justified. It even might be argued that no divacancy contribution to impurity diffusion of Pd in Ag exists (i.e. because of a repulsive interaction between Pd and a vacancy in Ag [215]). Therefore, the fitting procedure outlined in section 5.3.2 was repeated, now directly

extrapolating the impurity diffusion coefficients of Pd in Ag from Ref. [215], *without* consideration of any divacancy contribution to impurity diffusion of Pd in Ag. The resulting concentration-dependence of the chemical diffusion coefficient is shown in figure 5.13. Only at the highest annealing temperature of 455 °C, and at large atomic fraction of Pd, a modest effect on the concentration-dependent chemical diffusion coefficient is revealed.

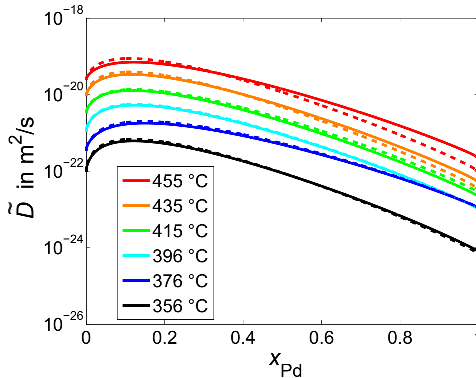

Figure 5.13: The concentration-dependent chemical diffusion coefficient, $\widetilde{D}$, as function of the atomic fraction of Pd, x_{Pd}, obtained by either considering a contribution of divacancies to the impurity diffusion of Pd in Ag (solid lines) or by directly extrapolating the impurity diffusion coefficients of Pd in Ag obtained at higher temperatures in Ref. [215] to the low annealing temperatures applied in this study without considering a contribution of divacancies to the diffusion mechanism (dashed lines).

Appendix 5.B Effect of the vacancy-wind effect on the chemical diffusion coefficient

The effect of the vacancy-wind factor, S_{wind}, on the determined chemical diffusion coefficient is small (see figure 5.14a). Due to the large difference of the self-diffusion coefficient of Ag and Pd, the vacancy-wind factor is almost constant over a concentration range of $0.02 < x_{\mathrm{Pd}} < 0.98$ (see figure 5.14b). The vacancy-wind factor is very close to the maximum value of $1/f = 1/0.7815 = 1.28$ (where f is the geometric correlation factor for the crystal lattice concerned, i.e. 0.7815 for the fcc crystal structure [50]).

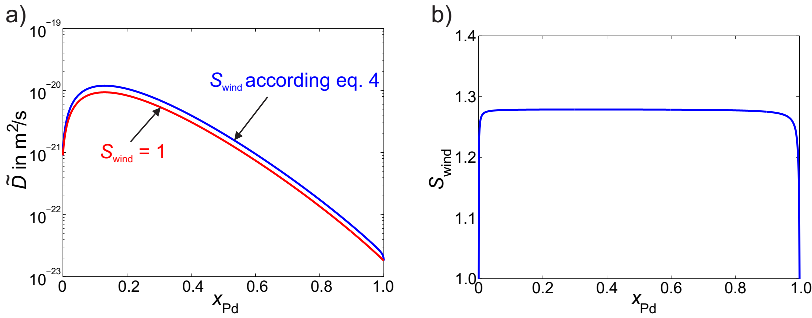

Figure 5.14: a) Chemical diffusion coefficient, $\widetilde{D}$, of the specimen annealed at 415 °C for 1 h, as function of the atomic fraction of Pd, x_{Pd}, calculated with a vacancy-wind factor of 1 (red line) and the vacancy-wind factor, as calculated according to equation 5.4 in the manuscript (blue line). b) The corresponding concentration-dependence of the vacancy-wind factor.

Appendix 5.C Microstructure after prolonged diffusion annealing

Pole-figure measurements, after the third thermal cycle, i.e. including the isothermal annealing for ≈ 4.4 h at 417 °C, (see figure 5.10 for the temperature program) show that the texture of the specimen is maintained (see figure 5.15). Microstructural changes can be observed at the specimen surface. After the prolonged heat treatment (= completion of the third thermal cycle, including the isothermal annealing step at 417 °C), the specimen surface has become rough (see figure 5.16) and an enrichment of Ag at the initial C/Pd interface has occurred (see figure 5.17). The enrichment of Ag at the C/Pd interface is attributed to fast surface diffusion of Ag along isolated holes in the Pd sublayer.[11] Due to the considerably faster surface and interface diffusion, as compared to volume diffusion, Ag atoms can diffuse through these holes and then along the C/Pd interface. The driving force for this process can be the smaller energy of the interfaces C/Ag and Ag/Pd [252], as compared to the interface C/Pd and/or the relaxation of stress in the Ag sublayer (cf. section 5.3.6).

[11] Note that at the temperatures applied in this study, even volume diffusion of Ag in Ag is six orders of magnitude faster than volume diffusion of Pd in Pd.

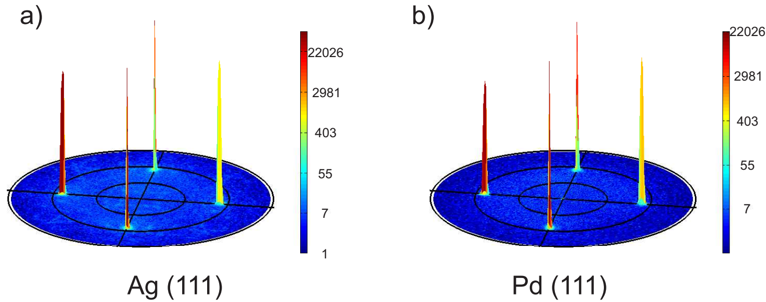

Figure 5.15: (111) pole figures of the Pd/Ag bilayer recorded at a) $2\theta = 44.57°$ corresponding to Ag(111) and at b) $2\theta = 46.94°$ corresponding to Pd(111), after the third thermal cycle, including the isothermal annealing for ≈ 4.4 h at 417 °C (see figure 5.10 for the temperature program). Note that the background intensity has increased upon annealing (cf. figure 5.1 for the as-prepared specimen).

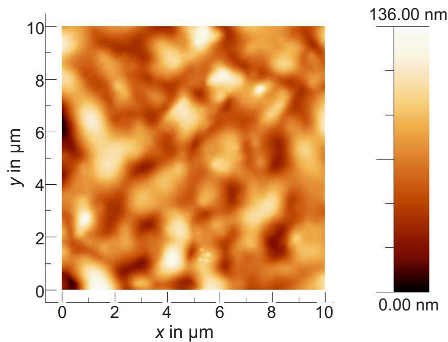

Figure 5.16: AFM image of the surface of a Si_3N_4/C/Pd/Ag thin film after prolonged annealing (i.e. after completing the third thermal cycle , including the isothermal annealing for ≈ 4.4 h at 417 °C) (see figure 5.10 for the temperature program). The surface roughness has increased considerably (root mean squared roughness (RMS) of 20 nm), as compared to the as-prepared state (RMS = 0.7 nm).

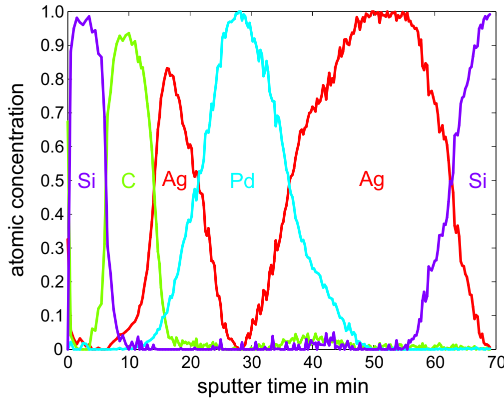

Figure 5.17: AES concentration-depth profiles after prolonged annealing (i.e. after completing the third thermal cycle , including the isothermal annealing for ≈ 4.4 h at 417 °C) (see figure 5.10 for the temperature program). Ag enrichment at the C/Pd interface can be observed. Note that the depth resolution, i.e. the sharpness of the interfaces, is considerably affected by the large surface roughness after diffusion annealing. No conclusion about volume diffusion coefficients can be extracted reliably from this measurement.

Appendix 5.D Fitting of XRD peak evolution upon diffusion annealing

A similar procedure, as applied in Refs. [10, 241–243] has been applied in this work to describe the evolution of the Ag and Pd XRD diffraction profiles during diffusion annealing. For the purpose of the simulation of the X-ray diffraction pattern, the specimen was hypothetically subdivided into slabs with a thickness of 1 nm. The composition of each slab was determined from the calculated concentration-depth profile, according to the procedure as described in section 5.3.2. The expected diffraction pattern of this slab was then calculated assuming a diffraction (sub)profile of the slab of Gaussian shape. The contribution of each slab to the total diffracted intensity was calculated by accounting for the X-ray absorption through the layers between the specimen surface and the slab considered [241]. It was assumed that each slab diffracts independently. The effect of instrumental broadening was considered to be negligible as compared to the diffusion-induced compositional line broadening. The effect of the planar stress, as determined by application of the $\sin^2\psi$ method (cf. section 5.2.3) , on the 2θ positions of

the diffraction (sub)profile, was accounted for as well. To this end, a very simplified stress profile was adopted, where the stress levels in the Ag and Pd sublayers were taken equal to the measured stress values (cf. section 3.62). Thus, the (1 1 3), (3 3 1), (3 1 1), (2 0 2), ($3\bar{1}3$) and ($3\bar{3}1$) diffraction profiles of both Ag and Pd, were fitted simultaneously. For the calculation of the concentration-depth profile, the impurity diffusion coefficient of Ag in Pd and the self-diffusion coefficient of Ag in Ag were taken as determined in this study (see figure 5.7). The fitting parameters were the FWHM of each peak, the ratio of the maxima of the corresponding Ag and Pd profiles and the background intensity in the diffraction profile. The Ag enrichment at the C/Pd interface, as observed after such prolonged annealing (see figure 5.17), has been incorporated as well in the fitting. The results of such a fit to all measured diffraction profiles at room temperature, after the completed third thermal cycle, including the isothermal annealing for $\approx$ 4.4 h at 417 °C (see figure 5.10 for the temperature program), is shown in figure 5.18. In view of the simplicity of the model a reasonable agreement of the model calculations with the measured diffraction profiles is obtained.

This result indicates that the shoulder development at the high angle side of the Ag diffraction peak is a consequence of the asymmetry in the concentration-depth profile (cf. section 5.3.2).

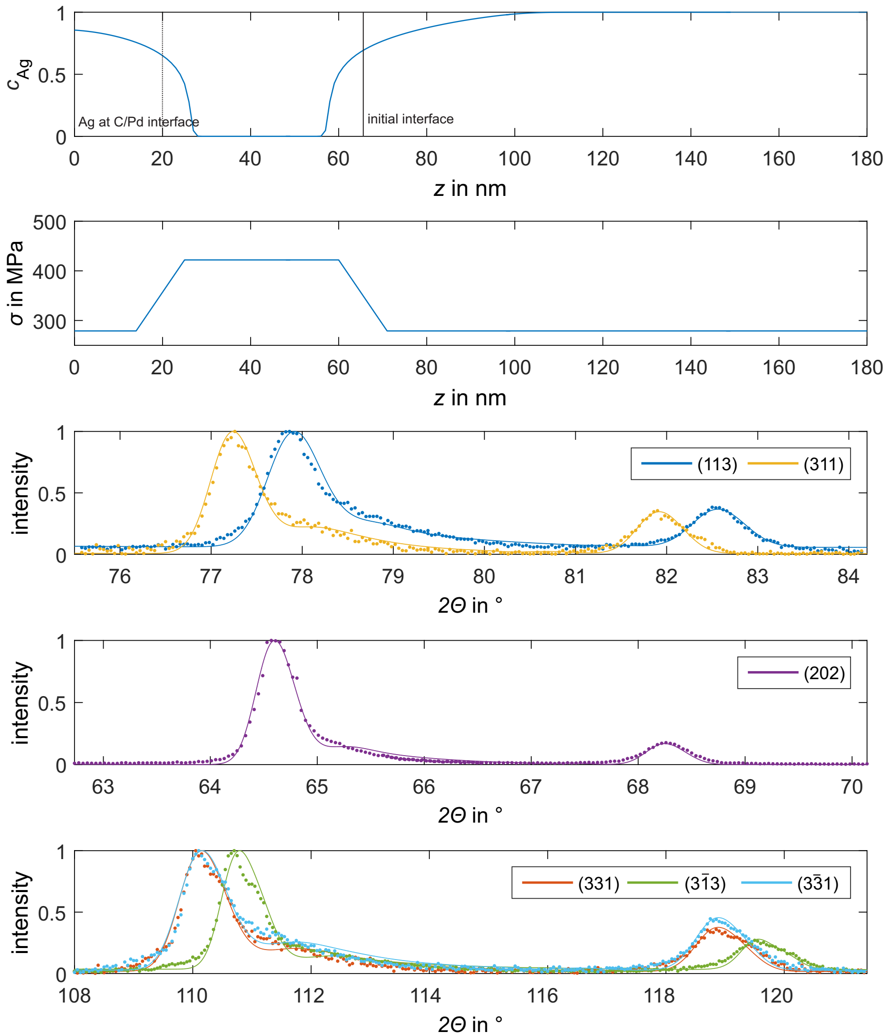

Figure 5.18: Exemplary fit of the X-ray diffractograms recorded at room temperature of the Pd/Ag sublayers after completing the third thermal cycle including the isothermal annealing for ≈ 4.4 h at 417 °C (see figure 5.10 for the temperature program). The development of the shoulder at the Ag peaks can be ascribed to the developing asymmetric concentration-depth profile. After prolonged diffusion annealing, Ag diffusion to the C/Pd interface through holes in the Pd layer could be evidenced by AES sputter-depth profiling (see figure 5.17) and this Ag sublayer has been incorporated in the calculation; the stress level in this Ag sublayer has an only negligible effect on the calculated diffractograms.

Appendix 5.E State of planar stress in the as-prepared state

The assumption of a state of planar stress with equal principal components of stress ($\sigma_{||} = \sigma_{11} = \sigma_{22}$) in the Ag and Pd sublayers has been verified by the measurement of (28 for Ag+28 for Pd) diffraction profiles at different ψ and ϕ. The emergence of straight lines for the dependence of $d \cdot \sqrt{(h^2 + k^2 + l^2)}$ as function of $\sin^2 \psi$ demonstrates that a planar state of stress with rotational symmetry, i.e. with $\sigma_{11} = \sigma_{22} = \sigma_{||}$, prevails (see figure 5.19).

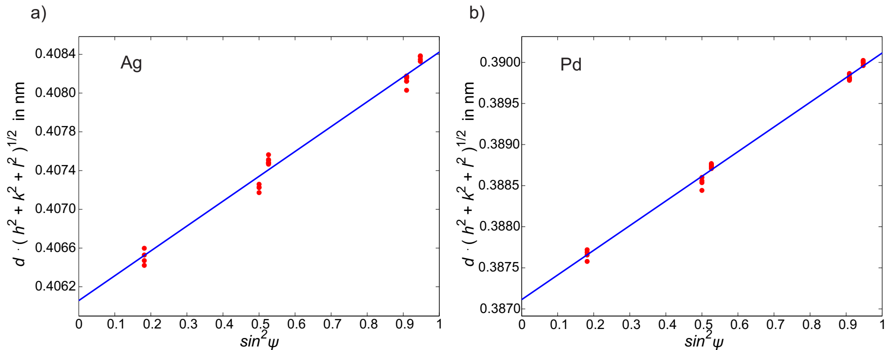

Figure 5.19: $\sin^2\psi$-plots for the a) Ag and b) Pd sublayers of an as-prepared Pd/Ag bilayer. For each sublayer 28 diffraction profiles have been measured. The results are fully compatible with an equibiaxial state of stress in both sublayers.

Chapter 6

Summary

6.1 Summary in the English language

Thin film systems are applied in many technological devices. Their functional properties strongly depend on the sharpness of the included interface(s). Interdiffusion during (thermal) processing or operation can broaden the initially sharp concentration-depth profile at the interface(s) and thus degrade the functional properties of the device. In this thesis, the interrelation of interdiffusion and microstructure of thin films is investigated. To this end, over the whole concentration range fully miscible model systems have been prepared by thermal evaporation and magnetron sputtering. The thin film deposition parameters were carefully adjusted to obtain amorphous or single-crystalline specimens. Due to the absence of short circuit diffusion paths, such as grain boundaries, in these thin films, other microstructural effects on interdiffusion, such as the role of dislocations and the absence of long range order in amorphous materials as well as the interrelation of interdiffusion and stress, can be investigated.

The microstructure of the prepared thin films has been characterised by X-ray diffraction (XRD), (high resolution) transmission electron microscopy ((HR)TEM), atomic force microscopy (AFM) and positron annihilation Doppler broadening spectroscopy (DBS). Information about interdiffusion has been deduced from the concentration-depth profiles measured before and after diffusion annealing by Auger electron spectroscopy (AES) and X-ray photoelectron spectroscopy (XPS) sputter-depth profiling. Sputter-induced alterations due to the sputter-depth profiling procedure have been modelled by applying the Mixing-Roughness-Information depth (MRI) model. To this end, the MRI model has been extended to increase its reliability in interdiffusion studies in thin films (see **Chapter 2**): in interdiffusion studies, the initially sharp interfaces are broadened by interdiffusion during diffusion annealing. In order to model the sputter-induced alterations in the diffusion zone, concentration-dependent MRI model parameters have been introduced. While the concentration dependence of the mixing parameter can have a strong effect on the intensity-depth profiles, the effects of a concentration gradient on the backscatter correction for AES sputter-depth profiling has been found to be negligible small. Since the often applied normalisa-

tion procedure of the measured intensities can generally not be applied due to the different information depths of the signal, an alternative normalisation procedure is introduced, which allows the consideration of independent measured intensity-depth profiles simultaneously in a multiple-profile fitting procedure. This multiple-profile fitting procedure increases the reliability of determined MRI model parameters and increases the reliability of diffusion coefficients which are deduced from the measured intensity-depth profiles of diffusion annealed specimens. This MRI model extension allows to reliably resolve diffusion lengths in the nanometre range from measured AES or XPS sputter-depth profiles. With the knowledge of thermodynamic data of the investigated system, the extended MRI model allows to account for the concentration dependence of the intrinsic diffusion coefficients and allows the determination of self-diffusion coefficients if an assumption on their concentration dependence is made (e.g. an exponential concentration dependence). These MRI model extensions provided the basis for the investigation of the interrelation of interdiffusion and microstructure in thin films, carried out in this work.

In **Chapter 3** interdiffusion in amorphous $Si_{1-x}Ge_x$ (a-$Si_{1-x}Ge_x$) solid solutions with $x \leq 48$ at.% Ge has been investigated in the temperature range of 440 °C - 460 °C. In order to avoid crystallisation of the metastable amorphous phase during diffusion annealing, low annealing temperatures have to be applied. Consequently, only very small diffusion lengths can be realised in reasonable time frames. By applying the extended MRI model to measured AES sputter-depth profiles, these small diffusion lengths in the nanometre range could be measured and concentration dependent self-diffusion coefficients could be deduced.

The amorphous state of the specimen after diffusion annealing was confirmed by XRD and cross-sectional TEM. Structural relaxation of the amorphous phase occurs at much shorter timescales (some hours), as compared to the diffusion annealing conditions applied in this work (hundreds of hours) and has no influence on the deduced self-diffusion coefficients.

It is revealed that the self-diffusion coefficients of Si and Ge in a-$Si_{1-x}Ge_x$ are about ten orders of magnitude larger than the self-diffusion coefficients of Si and Ge in the corresponding crystalline phases. Si and Ge diffuse via the vacancy mechanism at low temperatures in *crystalline* $Si_{1-x}Ge_x$. However, in *amorphous* $Si_{1-x}Ge_x$ no equilibrium point defects, such as vacancies, are present. It is discussed that the free volume inherent in the amorphous phase allows diffusional jumps and explains the considerably larger self-diffusion coefficients in the *amorphous* phase, as compared to the *crystalline* phase. The rather large activation enthalpy of Si and Ge self-diffusion in a-$Si_{1-x}Ge_x$ suggests that the free volume in a-$Si_{1-x}Ge_x$ is distributed over the whole system and does not allow a single atomic jump according a “vacancy-like”

diffusion mechanism. Several atoms need to change their position to allow a diffusional jump of an atom. The observed concentration dependence of the self-diffusion coefficients of Si and Ge in a-$Si_{1-x}Ge_x$ solid solutions is explained by the covalent bonding between the atoms. Due to the smaller covalent bond strength of Ge-Ge, as compared to Si-Si, the self-diffusion coefficient of Si and Ge in a-$Si_{1-x}Ge_x$ solid solutions increases and the activation enthalpy decreases with increasing Ge concentration.

The effect of vacancy sources and sinks on interdiffusion in epitaxial Au/Ag bilayers is investigated in **Chapter 4**. At lower annealing temperatures, the vacancy mechanism is the dominating diffusion mechanism in metals and semiconductors. Since the diffusivities of the components in a classical bilayered diffusion couple are generally different, interdiffusion is accompanied with a net vacancy flux in the direction of the faster diffusing species. Lattice defects, such as grain boundaries and dislocations can serve as vacancy sources and sinks and can maintain the equilibrium vacancy concentration-depth profile upon diffusion annealing (Darken-Manning case). In systems with a small amount of defects, such as grain boundaries and dislocations, the distance between vacancy sources and sinks can be larger than the diffusion length and the equilibrium vacancy concentration-depth profile cannot be maintained during diffusion annealing (Nernst-Planck case).

The system Ag/Au was chosen as a model system, since the lattice parameters of Ag and Au are very similar. This allows the preparation of single-crystalline specimens with practically no misfit dislocations at the Au/Ag interface. The small density of defects allows the determination of the role of vacancy sources and sinks on interdiffusion. To this end, the chemical concentration-depth profile has been measured by AES sputter-depth profiling and evaluated by applying the extended MRI model. The change in the defect concentration-depth profile during diffusion annealing has been measured by *in-situ* positron annihilation Doppler broadening spectroscopy. It was not possible to determine on the basis of the measured concentration-depth profiles alone whether the Darken-Manning or the Nernst-Planck treatment can be applied. However, a detailed evaluation of the deduced impurity diffusion coefficients, considering the divacancy contribution to the diffusion mechanism at elevated temperatures, revealed that the Darken-Manning treatment holds, i.e. the equilibrium vacancy concentration-depth profile is maintained during interdiffusion. The change in the defect concentration-depth profile, as determined by *in-situ* positron annihilation Doppler broadening spectroscopy during diffusion annealing cannot be explained by the change of the vacancy concentration-depth profile. Most likely microstructural changes, i.e. domain growth, are dominating the observed changes of the defect concentration-depth profile during diffusion annealing.

The interrelation of interdiffusion and stress in single-crystalline Pd/Ag bilayers has been investigated in **Chapter 5**. Thin films can exhibit large in-plane stresses, which arise by the preparation method of the thin film (growth stress) and/or by thermally induced stress due to different thermal expansion coefficients of the thin film and the substrate (thermal stress). Such stresses can affect the diffusional jumps of the atoms and can change as a result of interdiffusion. For example, if the molar volumes of the interdiffusing atoms are different, a compressive compositional stress is induced in the sublayer composed of mainly the smaller atoms and a tensile compositional stress is induced in the sublayer composed of mainly the larger atoms.

In this work, interdiffusion in single-crystalline Pd/Ag bilayers has been investigated in the low temperature range of 356 °C to 455 °C. The concentration-depth profiles before and after diffusion annealing could be determined by AES sputter-depth profiling and the extended MRI model. This approach allowed the determination of the concentration-dependent chemical diffusion coefficient, the self-diffusion coefficient of Ag in Ag and the impurity diffusion coefficient of Ag in Pd. Due to the similarity of the concentration dependences of the intrinsic diffusion coefficients, the chemical diffusion coefficient varies over the whole composition range, by only three orders of magnitude, despite the large difference of six orders of magnitude of the self-diffusion coefficients of Ag in Ag and Pd in Pd.

During interdiffusion, the equilibrium vacancy concentration is maintained by the creation and annihilation of vacancies at defects and by the positive climb of misfit dislocations originally located at the Pd/Ag interface. Consequently, the Darken-Manning treatment has to be applied for the description of the concentration-depth profiles after diffusion annealing.

The stress evolution in the Pd and Ag sublayers of the Pd/Ag bilayer upon thermal cycling and isothermal annealing could be determined in each sublayer separately by *in-situ* XRD measurements. Upon diffusion annealing the initial compressive thermal stress in both sublayers relaxes considerably in the Ag sublayer and in a minor way in the Pd sublayer. In the Ag sublayer a tensile compositional stress (due to replacement of (larger) Ag atoms with (smaller) Pd atoms) can develop. Due to the very high mobility of Ag at the annealing temperatures applied, other relaxation processes, such as microstructural changes associated with dislocation glide-plus-climb and also out-diffusion of Ag through holes and domain boundaries in the Pd sublayer occur. In the Pd sublayer, a compressive compositional stress (due to replacement of Pd atoms (smaller) with Ag atoms (larger)) can develop. The compressive (thermal) stress in the Pd sublayer is compensated in a minor way by the tensile stress component induced by the positive climb of misfit dislocations. Other relaxation mechanism do not operate significantly in the Pd sublayer.

6.2 Zusammenfassung in deutscher Sprache

Dünnschichtsysteme werden in vielen technologisch wichtigen Anwendungen eingesetzt. Ihre funktionellen Eigenschaften hängen stark von der Schärfe der enthaltenen Grenzflächen ab. Während der (thermischen) Verarbeitung oder ihres Gebrauches kann das ursprünglich scharfe Konzentrationstiefenprofil an der Grenzfläche durch Interdiffusion verbreitert werden, was zu einer Verschlechterung der funktionalen Eigenschaften des Dünnschichtsystems führt. In dieser Arbeit wird der Zusammenhang zwischen Interdiffusion und Mikrostruktur untersucht. Dafür wurden über den kompletten Konzentrationsbereich mischbare Modellsysteme mit Hilfe von thermischem Verdampfen und Magnetronsputtering hergestellt. Die Abscheideparameter für die Dünnschichtabscheidung wurden dabei sorgfälltig angepasst um entweder komplett amorphe oder einkristalline Proben zu erhalten. Durch die Abwesenheit von schnellen Diffusionspfaden in diesen Dünnschichtsystemen, wie z.B. Korngrenzen, können andere mikrostrukturelle Effekte auf die Interdiffusion, wie die Rolle von Versetzungen oder die Abwesenheit von langreichweitiger Ordnung in amorphen Materialien, untersucht werden.

Die Mikrostruktur der hergestellten Proben wurde mit Hilfe von Röntgendiffraktometrie (XRD), (hochauflösender) Transmissionselektronenmikroskopie ((HR)TEM), Rasterkraftmikroskopie (AFM) sowie Positron-Annihilations-Dopplerverbreiterungs-Spekroskopie (DBS) charakterisiert. Informationen über Interdiffusion wurde von Konzentrationstiefenprofilen gewonnen, die mit Hilfe von Augerelektronenspektroskopie (AES) und Röntgenphotoelektronenspektroskopie (XPS) Sputter-Tiefenprofilierung gemessen wurden. Die durch den Sputtervorgang hervorgerufenen Veränderungen der Probe wurden mit Hilfe des Mixing-Roughness-Information depth (MRI) Modells modelliert. Dafür wurde das MRI Modell erweitert um es verlässlicher für Interdifussionsuntersuchungen an Dünnschichtsystemen zu machen (siehe **Kapitel 2**): In Interdiffusionstudien werden die anfänglich scharfen Grenzflächen während der Diffusionsauslagerung durch Interdiffusion verbreitert. Um die durch das Sputtern verursachten Probenveränderungen in der Diffusionszone zu modellieren wurden konzentrationsabhängige MRI Modellparameter eingeführt. Die Konzenrationsabhängigkeit des Mixing-Parameters hat dabei einen starken Einfluss auf das Intensitätstiefenprofil, wohingegen der Einfluss des Konzentrationsgradienten auf die Rückstreukorrektur der AES Sputter-Tiefen-profilierung einen vernachlässigbar kleinen Einfluss hat. Da die oftmals angewandte Normalisierung der gemessenen Intensitäten wegen den unterschiedlichen Informationstiefen der Signale generell nicht angewandt werden kann, wurde eine alternative Normalisierungsprozedur eingeführt, die es erlaubt unabängig voneinander gemessene Intensitäts Tiefenprofile

gleichzeitig in einer Vielprofil-Anpassungs-Prozedur zu berücksichtigen. Diese Vielprofil-Anassungs-Prozedur erhöht die Verlässlichkeit der bestimmten MRI Modellparameter und erhöht die Verlässlichkeit von Diffusionskoeffizienten, die aus den gemessenen Intensitätstiefenprofilen von diffusionsausgelagerten Proben ermittelt wurden. Mit Hilfe dieser MRI Modellerweiterungen können verlässlich Diffusionslängen in der Größenordnung von einigen Nanometern von gemessenen AES oder XPS Sputter-Tiefenprofilen aufgelöst werden. Mit der Kenntnis von thermodynamischen Daten des untersuchten Systems erlaubt das erweiterte MRI Modell die Konzentrationsabhängigkeit von intrinsischen Diffusionskoeffizienten zu berücksichtigen und ermöglicht es Selbstdiffusionskoeffizienten zu bestimmen, wenn eine Annahme über deren Konzentrationsabhängigkeit (z.B. eine exponentielle Konzentrationsabhängigkeit) gemacht wird. Diese MRI Modellerweiterungen stellen die Grundlage für die Untersuchung des Zusammenhanges zwischen Interdiffusion und Mikrostruktur in Dünnschichtsystemen bereit.

In **Kapitel 3** wird Interdiffusion in amorphen $\mathrm{Si}_{1-x}\mathrm{Ge}_x$ (a-$\mathrm{Si}_{1-x}\mathrm{Ge}_x$) Festkörperlösungen mit Konzentrationen von $x \leq 48$ at.% Ge im Temperaturbereich von 440 °C - 460 °C untersucht. Um die Kristallisation der metastabilen amorphen Phase während der Diffusionsauslagerung zu vermeiden müssen niedrige Auslagerungstemperaturen gewählt werden. Die Diffusionslängen sind deshalb nach praktisch vernünftigen Auslagerungszeiten sehr klein. Durch die Anwendung des erweiterten MRI Modells auf gemessene AES Sputtertiefenprofile konnten Diffusionslängen im Nanometerbereich gemessen werden und konzentrationsabhängige Selbstdiffusionskoeffizienten bestimmt werden.

Der amorphe Zustand der Proben nach der Diffusionsauslagerung wurde mit Hilfe von XRD sowie mit TEM Querschnitten nachgewiesen. Strukturelle Relaxationen der amorphen Phase erfolgen in deutlich kürzeren Zeiten (einige Stunden) im Vergleich zu den Diffusionsauslagerungsbedingungen (hunderte Stunden) und beeinflussen deshalb die bestimmten Selbstdiffusionkoeffizienten nicht.

Es wurde beobachtet, dass die Selbstdiffusionskoeffizienten von Si und Ge in a-$\mathrm{Si}_{1-x}\mathrm{Ge}_x$ um ungefähr zehn Größenordnungen größer sind, als die Selbstdiffusionskoeffizienten von Si und Ge in der entsprechenden kristallinen Phase. Si und Ge diffundieren in *kristallinem* $\mathrm{Si}_{1-x}\mathrm{Ge}_x$ bei niedrigen Temperaturen nach dem Leerstellenmechanismus. In *amorphem* $\mathrm{Si}_{1-x}\mathrm{Ge}_x$ sind allerdings keine Gleichgewichtspunktdefekte, wie z.B. Leerstellen, vorhanden. Es wird diskutiert, dass das Freie Volumen der amorphen Phase Diffusionssprünge erlaubt und so die deutlich größeren Selbstdiffusionskoeffizienten in der *amorphen* Phase gegenüber der *kristallinen* Phase erklärt. Die eher große Aktivierungsenthalpie von der Si und Ge Selbstdiffusion in

a-$Si_{1-x}Ge_x$ lässt vermuten, dass das Freie Volumen in a-$Si_{1-x}Ge_x$ über das gesamte System verteilt ist und keinen Sprung eines einzelnen Atoms nach einem “leerstellenartigen” Diffusionsmechanismus erlaubt. Mehrere Atome müssen ihre Position ändern, um einen Diffusionssprung zu erlauben. Die beobachtete konzentrationsabhängigkeit der Selbstdiffusionskoeffizienten von Si und Ge in a-$Si_{1-x}Ge_x$ Festkörperlösungen wird durch die kovalente Bindung zwischen den Atomen erklärt. Aufgrund der geringeren Bindungsstärke von Ge-Ge, im Vergleich zu Si-Si, steigt der Selbstdiffusionskoeffizient von Si und Ge in a-$Si_{1-x}Ge_x$ und sinkt die Aktivierungsenthalpie mit steigender Ge Konzentration.

Der Einfluss von Leerstellenquellen und -senken auf Interdiffusion in epitaktischen Au/Ag Doppelschichten wird in **Kapitel 4** untersucht. Bei niedrigen Auslagerunstemperaturen ist der Leerstellenmechanismus der dominierende Diffusionsmechanismus in Metallen und Halbleitern. Da die Diffusivitäten der Komponenten in einem klassischen Doppelschicht Diffusionspaar unterschiedlich sind, ist Interdiffusion mit einem Netto Leerstellenfluß in Richtung der schneller diffundierenden Komponente verknüpft. Gitterdefekte, wie Korngrenzen oder Versetzungen können das Gleichgewichtsleerstellenkonzentrationstiefenprofil während der Diffusionsauslagerung aufrecht erhalten (Darken-Manning Fall). In Systemen mit einer geringen Dichte an Defekten, wie Korngrenzen oder Versetzungen, kann der Abstand zwischen Leerstellenquellen und -senken größer als die Diffusionslänge sein und somit kann die Gleichgewichtsleerstellenkonzentration während der Diffusionsauslagerung nicht aufrecht erhalten werden (Nernst-Planck Fall).

Das System Ag/Au wurde als Modellsystem gewählt, da die Gittermparameter von Ag und Au sehr ähnlich sind. Dies ermöglicht die Herstellung von einkristallinen Proben, die praktisch keine Fehlpassungsversetzungen an der Au/Ag Grenzfläche besitzen. Diese geringe Defektkonzentration erlaubt die Untersuchung der Rolle von Leerstellenquellen und -senken auf die Interdiffusion. Dazu wurde das chemische Konzentrationstiefenprofil mit Hilfe von AES Sputter-Tiefenprofilierung gemessen und mit dem erweiterten MRI Modell ausgewertet. Die Änderung im Defektkonzentrationstiefenprofil während der Diffusionsauslagerung wurde mit Hilfe von *in-situ* Positronen Annihilations Dopplerverbreiterungs Spektroskopie untersucht. Es war nicht möglich zwischen dem Darken-Manning Modell und dem Nernst-Planck Modell zu unterscheiden, wenn nur die gemessenen Konzentrationstiefenprofile herangezogen wurden. Eine detaillierte Auswertung der bestimmten Fremdatomsdiffusionskoeffizienten, die den Beitrag von Doppelleerstellen zum Diffusionsmechanismus bei hohen Temperaturen berücksichtigt, zeigt jedoch, dass das Darken-Manning Modell erfüllt ist, d.h. das Leerstellenkonzentrationstiefenprofil während der Diffusionsauslagerung aufrecht erhalten wird.

Die Veränderung im Defektkonzentrationstiefenprofil, die mit Hilfe der *in-situ* Positronen Annihilations Dopplerverbreiterungs Spektroskopie ermittelt wurde, kann nicht mit der Änderung des Leerstellenkonzentrationstifenprofils erklärt werden. Höchstwahrscheinlich dominieren mikrostrukturelle Änderungen, wie z.B. Domänenwachstum, die beobachteten Änderungen des Defektkonzentrationstiefenprofils.

Die Wechselwirkung zwischen Interdiffusion und Spannungen in einkristallinen Pd/Ag Doppelschichten wird in **Kapitel 5** untersucht. Dünne Schichten können sehr große planare Spannungen aufweisen, die durch die Herstellung der dünnen Schicht (Wachstumsspannungen) und/oder von thermischer Spannung, die durch einen Unterschied in den thermischen Ausdehnungskoeffizienten des Substrates und der Schicht herrühren, hervorgerufen werden (thermische Spannungen). Solche Spannungen können die Sprünge der Atome beeinflussen und sich durch diese ändern. Wenn zum Beispiel die molaren Volumen der diffundierenden Atome unterschiedlich sind, so wird eine konzenrationsbedingte Druckspannung in der Subschicht hervorgerufen, die hauptsächlich aus den kleineren Atomen besteht und es wird eine konzentrationsbedingte Zugspannung in der Subschicht erzeugt, die hauptsächlich aus den größeren Atomen aufgebaut ist.

In dieser Arbeit wurde Interdiffusion in einkristallinen Pd/Ag Doppelschichten in dem niedrigen Temperaturbereich von 356 °C bis 455 °C untersucht. Die Konzentrationstiefenprofile vor und nach der Diffusionsauslagerung wurden mit AES Sputter-Tiefenprofilierung und dem erweiterten MRI Modell bestimmt. Dieses Vorgehen erlaubte die Bestimmung des konzentrationsabhängigen chemischen Diffusionskoeffizienten, des Selbstdiffusionskoeffizienten von Ag in Ag und des Fremdatomsdiffusionskoeffizienten von Ag in Pd. Wegen der Ähnlichkeit der Konzenrationsabhängigkeit der intrinsischen Diffusionskoeffizienten, ändert sich der chemische Diffusionskoeffizent über den gesamten Konzentrationsbereich nur über drei Größenordnungen, obwohl sich die Selbstdiffusionskoeffizienten von Ag in Ag und von Pd in Pd um sechs Größenordnungen unterscheiden.

Die Gleichgewichtsleerstellenkonzentration in dem Dünnschichtsystem wird während dem Diffusionsauslagern durch die Erzeugung und Vernichtung von Leerstellen an Defekten und durch positives Klettern von Fehlpassungsversetzungen, die ursprünglich an der Pd/Ag Grenzfläche waren, aufrecht erhalten. Folglich muss das Darken-Manning Modell für die Beschreibung der Konzentrationstiefenprofile verwendet werden.

Die Spannungsentwicklung während des thermischen Zyklierens und des isothermen Auslagerns konnte in der Pd und Ag Subschicht der Pd/Ag Doppelschicht getrennt voneinander mit Hilfe von *in-situ* röntgendiffraktometrischen Messungen bestimmt werden. Die anfängliche thermische Druckspan-

nung in beiden Subschichten relaxiert während der Diffusionsauslagerung deutlich in der Ag Subschicht und sehr gering in der Pd Subschicht. In der Ag Subschicht kann eine konzentrationsbedingte Zugspannung (durch den Austausch von (größeren) Ag Atomen mit (kleineren) Pd Atomen) ausgebildet werden. Durch die sehr große Mobilität von Ag bei den angewandten Auslagerungsbedingungen, laufen andere Relaxationsprozesse, wie Mikrostrukturänderungen in Verbindung mit dem Gleiten und Klettern von Versetzungen und ebenso der Herausdiffusion von Ag durch Löcher und Domänengrenzen in der Pd Subschicht, ab. In der Pd Subschicht kann sich eine konzentrationsbedingte Druckspannung ausbilden. Die thermische Druckspannung in der Pd Subschicht wird zu einem kleinen Teil durch die Zugspannungskomponente, die durch das positive Klettern von Fehlpassungsversetzungen hervorgerufen wird, kompensiert. Andere Relaxationsprozesse spielen in der Pd Subschicht keine nennenswerte Rolle.

Bibliography

[1] M. Kuball, M. Ťapajna, R. J. T. Simms, M. Faqir, and U. K. Mishra, Microelectron. Reliab. **51**, 195 (2011).

[2] K. D. Dobson, I. Visoly-Fisher, G. Hodes, and D. Cahen, Sol. En. Mat. Solar Cells **62**, 295 (2000).

[3] M. Hawraneck, J. Zimmer, W. Raberg, K. Prügl, S. Schmitt, T. Bever, S. Flege, and L. Alff, Appl. Phys. Lett. **93**, 012504 (2008).

[4] K. Zeng, R. Stierman, T.-C. Chiu, D. Edwards, K. Ano, and K. N. Tu, J. Appl. Phys. **97**, 024508 (2005).

[5] J. Chakraborty, U. Welzel, and E. J. Mittemeijer, Thin Solid Films **518**, 2010 (2010).

[6] F. J. A. den Broeder, Acta Metall. **20**, 319 (1972).

[7] E. J. Mittemeijer and A. M. Beers, Thin Solid Films **65**, 125 (1980).

[8] G. Schmitz, D. Baither, M. Kasprzak, T. H. Kim, and B. Kruse, Scr. Mater. **63**, 484 (2010).

[9] A. M. Eich, M. Kasprzak, A. Gusak, and G. Schmitz, Acta Mater. **60**, 3469 (2012).

[10] D. Baither, T. H. Kim, and G. Schmitz, Scr. Mater. **58**, 99 (2008).

[11] R. G. Kirsch, J. M. Poate, and M. Eibschutz, Appl. Phys. Lett. **29**, 772 (1976).

[12] E. J. Mittemeijer, *Fundamentals of Materials Science* (Springer Berlin / Heidelberg, 2010, Chapter 9) pp. 438–439.

[13] G. K. Williamson and R. E. Smallman, Philos. Mag. **1**, 34 (1956).

[14] K. L. Chopra, P. D. Paulson, and V. Dutta, Progress in Photovoltarics: Research and Applications **12**, 69 (2004).

[15] D. E. Polk, J. Non-Cryst. Solids **5**, 365 (1971).

[16] F. Wooten, K. Winer, and D. Weaire, Phys. Rev. Lett. **54**, 1392 (1985).

[17] M. M. J. Treacy and K. B. Borisenko, Science **335**, 950 (2012).

[18] H. Schmidt, M. Gupta, and M. Bruns, Phys. Rev. Lett. **96**, 055901 (2006).

[19] R. Koch, J. Phys.: Condens Matter **6**, 9519 (1994).

[20] D. Flötotto, Z. M. Wang, L. P. H. Jeurgens, and E. J. Mittemeijer, Appl. Phys. Lett. **104**, 091901 (2014).

[21] Y. Kuru, U. Welzel, and E. J. Mittemeijer, Appl. Phys. Lett. **105**, 221902 (2014).

[22] Y. Kuru, J. Chakraborty, U. Welzel, M. Wohlschlögel, and E. J. Mittemeijer, Mater. Sci. Forum **524-525**, 801 (2006).

[23] Y. Kuru, M. Wohlschlögel, U. Welzel, and E. J. Mittemeijer, Thin Solid Films **516**, 7615 (2008).

[24] J. Chakraborty, U. Welzel, and E. J. Mittemeijer, J. Appl. Phys. **103**, 113512 (2008).

[25] J. Sheng, U. Welzel, and E. J. Mittemeijer, Z. Krist. Supl. **30**, 247 (2009).

[26] J. Sheng, U. Welzel, and E. J. Mittemeijer, Advanced Materials Research **89-91**, 503 (2010).

[27] H. Mehrer, Defect and Diffusion Forum **129-130**, 57 (1996).

[28] P. Klugkist, A. N. Aleshin, W. Lojkowski, L. S. Shivindlerman, W. Gust, and E. J. Mittemeijer, Acta Mater. **49**, 2941 (2001).

[29] S. M. Prokes and F. Spaepen, Appl. Phys. Lett. **47**, 234 (1985).

[30] S. M. Prokes and F. Spaepen, Mater. Res. Soc. Symp. Proc. **56**, 383 (1986).

[31] C. Janot, A. Bruson, and G. Marchal, J. Phys. (Paris) **47**, 1751 (1986).

[32] H. Schmidt, M. Gupta, T. Gutberlet, J. Stahn, and M. Bruns, Acta Mater. **56**, 464 (2008).

[33] F. Hartung and G. Schmitz, Phys. Rev. B **64**, 245418 (2001).

[34] P. Stender, Z. Balogh, and G. Schmitz, Ultramicroscopy **111**, 524 (2011).

[35] G. B. Thompson, M. K. Miller, and H. L. Fraser, Ultramicroscopy **100**, 25 (2004).

[36] A. Bukaluk, Appl. Surf. Sci. **175-176**, 790 (2001).

[37] J. Y. Wang and E. J. Mittemeijer, J. Mater. Res. **19**, 3389 (2004).

[38] R. O. Simmons and R. W. Balluffi, Phys. Rev. **119**, 600 (1960).

[39] R. O. Simmons and R. W. Baluffi, Phys. Rev. **125**, 862 (1962).

[40] H. Mehrer, *Diffusion in Solids: Fundamentals, Methods, Materials, Diffusion-Controlled Processes* (Springer Berlin / Heidelberg, 2007).

[41] P. G. Shewmon, *Diffusion in Solids* (Minerals, Metals & Materials

Society, 1989).

[42] D. A. Porter, K. E. Easterling, and M. Y. Sherif, *Phase Transformations in Metals and Alloys* (CRC Press, 2008) p. 92.

[43] J. Philibert, *Atom Movements - Diffusion and Mass Transport in Solids* (Les Éditions de Physique, Les Ulis, France, 1991) pp. 207–209.

[44] A. D. Smigelskas and E. O. Kirkendall, Trans. AIME **171**, 130 (1947).

[45] L. S. Darken, Trans. AIME **175**, 184 (1948).

[46] A. V. Nazarov and K. P. Gurov, Fiz. metal. metalloved. **34**, 936 (1972).

[47] A. V. Nazarov and K. P. Gurov, Fiz. metal. metalloved. **37**, 496 (1974).

[48] A. V. Nazarov and K. P. Gurov, Fiz. metal. metalloved. **38**, 486 (1974).

[49] A. V. Nazarov and K. P. Gurov, Fiz. metal. metalloved. **38**, 689 (1974).

[50] J. Philibert, *Atom Movements - Diffusion and Mass Transport in Solids* (Les Éditions de Physique, Les Ulis, France, 1991).

[51] R. W. Balluffi, Acta Metall. **2**, 194 (1954).

[52] L. Kornblit, phys. stat. sol. **115**, 485 (1983).

[53] H. Mehrer and A. Seeger, phys. stat. sol. **39**, 647 (1970).

[54] F. Faupel, P. W. Hüppe, and K. Rätzke, Phys. Rev. Lett. **65**, 1219 (1990).

[55] F. Faupel, W. Frank, M.-P. Macht, H. Mehrer, V. Naundorf, K. Rätzke, H. R. Schober, S. K. Sharma, and H. Teichler, Rev. Mod. Phys. **75**, 237 (2003).

[56] C. Oligschleger, C. Gaukel, and H. R. Schober, J. Non-Cryst. Solids **250-252**, 660 (1999).

[57] C. Bos, F. Sommer, and E. J. Mittemeijer, Acta Mater. **53**, 5333 (2005).

[58] A. D. Le Claire, Philos. Mag. **14**, 1271 (1966).

[59] J. R. Manning, Phys. Rev. B **4**, 1111 (1971).

[60] F. C. Larché and J. W. Cahn, Acta Metall. **21**, 1051 (1973).

[61] F. C. Larché and J. W. Cahn, Acta Metall. **30**, 1835 (1982).

[62] F. C. Larché and J. W. Cahn, Acta Metall. **33**, 331 (1985).

[63] M. Ohring, *Materials science of thin films* (Academic Press, 2002).

[64] D. Flötotto, Z. M. Wang, L. P. H. Jeurgens, and E. J. Mittemeijer, J. Appl. Phys. **112**, 043503 (2012).

[65] M. A. Noah, *Interdiffusion in Thin Films*, Diploma thesis, University of Stuttgart (2011).

[66] A. S. Dalton, Y. V. Kondratenko, and E. G. Seebauer, Chem. Eng. Sci. **65**, 2172 (2010).

[67] C. Becker, T. Sntheimer, S. Steffens, S. Scherf, and B. Rech, Energy Procedia **10**, 61 (2011).

[68] J. S. Custer, M. O. Thompson, D. C. Jacobson, J. M. Poate, S. Roorda, W. C. Sinke, and F. Spaepen, Appl. Phys. Lett. **64**, 437 (1994).

[69] E. E. Khawaja, S. M. A. Durrani, A. B. Hallakm, and M. Sakhawat Hussain, J. Non-Cryst. Solids **170**, 308 (1994).

[70] L. Vitos, A. V. Ruban, H. L. Skriver, and J. Kollár, Surf. Sci. **411**, 186 (1998).

[71] J. Narayan and B. C. Larson, J. Appl. Phys. **93**, 278 (2003).

[72] R. W. Olesinski, A. B. Gokhale, and G. J. Abbaschian, Bulletin of Alloy Phase Diagrams **10**, 635 (1989).

[73] W. M. Haynes, T. J. Bruno, and D. R. Lide, eds., *CRC Handbook of Chemistry and Physics*, 95th ed. (CRC Press/Tylor and Francis, Internet Version 2015).

[74] C. Hugenschmidt, K. Schreckenbach, M. Stadlbauer, and B. Straßer, Nucl. Instrum. Meth. A **554**, 384 (2005).

[75] S. Hofmann, *Auger- and X-ray Photoelectron Spectroscopy in Materials Science* (Springer Verlag Heidelberg, New York, Dordrecht, London, 2013).

[76] G. Gillen, J. M. Phelps, R. W. Nelson, P. Williams, and S. M. Hues, Surf. Interface Anal. **14**, 771 (1989).

[77] P. C. Zalm, Rep. Prog. Phys. **58**, 1321 (1995).

[78] H. Bracht, S. Schneider, and R. Kube, Microelectron. Eng. **88**, 452 (2011).

[79] P. Sigmund, "Sputtering by Particle Bombardment," (Springer Berlin / Heidelberg, 1981) Chap. Ion Bombardment: Theoretical Concepts, pp. 9–71.

[80] S. Hofmann, J. Vac. Sci. Technol. B **10**, 316 (1992).

[81] S. Hofmann, Surf. Interface Anal. **21**, 673 (1994).

[82] S. Hofmann, Vacuum **48**, 607 (1997).

[83] S. Hofmann and J. Schubert, J. Vac. Sci. Technol. A **16**, 1096 (1998).

[84] S. Hofmann, Reports On Progress In Physics **61**, 827 (1998).

[85] S. Hofmann, Surf. Interface Anal. **27**, 825 (1999).

[86] S. Hofmann, Thin Solid Films **398**, 336 (2001).

[87] S. Hofmann, Phil. Trans. R. Soc. A **362**, 55 (2004).

[88] S. Hofmann, Appl. Surf. Sci. **241**, 113 (2005).

[89] S. Hofmann and J. Y. Wang, Surf. Interface Anal. **39**, 324 (2007).

[90] J. Jung, O. Yu, S. Olubuyide, J. L. Hoyt, D. A. Antaniadis, M. L. Lee, and E. A. Fitzgerald, Appl. Phys. Lett. **84**, 3319 (2004).

[91] A. Csik, G. A. Langer, D. L. Beke, Z. Erdélyi, M. Menyhárd, and A. Sulyok, J. Appl. Phys. **89**, 804 (2001).

[92] C. J. Powell and A. Jablonski, *NIST Electron Effective-Attenuation-Length Database Version 1.3, SRD 82* (National Institute of Standards and Technology, Gaithersburg, 2011).

[93] Z. L. Liau, B. Y. Tsaur, and J. W. Mayer, J. Vac. Sci. Technol. **16**, 121 (1979).

[94] J. F. Ziegler, M. D. Ziegler, and J. P. Biersack, Nucl. Instrum. Meth. B **B268**, 1818 (2010).

[95] J. Y. Wang, U. Starke, and E. J. Mittemeijer, Thin Solid Films **517**, 3402 (2009).

[96] Y. Liu, Bachelor thesis, Shantou University (2012).

[97] S. Hofmann and J. Y. Wang, J. Surf. Anal. **10**, 52 (2003).

[98] P. Prieto, S. Hofmann, E. Elizalde, and J. M. Sanz, Surf. Interface Anal. **36**, 1392 (2004).

[99] S. Hofmann, J. Y. Wang, and A. Zalar, Surf. Interface Anal. **39**, 787 (2007).

[100] C. J. Powell and A. Jablonski, *NIST Backscattering-Correction-Factor Database Version 1.0, SRD 154* (National Institute of Standards and Technology, Gaithersburg, 2011).

[101] S. Hofmann and V. Kesler, Surf. Interface Anal. **33**, 461 (2002).

[102] S. Hofmann and W. Mader, Surf. Interface Anal. **15**, 794 (1990).

[103] J. Crank, *The Mathematics of Diffusion*, 2nd ed. (Calarendon Press: Oxford, 1975).

[104] A. Qteish and R. Resta, Phys. Rev. B **37**, 1308 (1988).

[105] R. Kube, H. Bracht, J. Lundsgaard Hansen, A. Nylandsted Larsen, E. E. Haller, S. Paul, and W. Lerch, J. Appl. Phys. **107**, 073520 (2010).

[106] A. S. Ferlauto, G. M. Ferreira, J. M. Pearce, C. R. Wronski, R. W. Collins, X. Deng, and G. Ganguly, J. Appl. Phys. **92**, 2424 (2002).

[107] J. Bullock, D. Yan, Y. Wan, A. Cuevas, B. Demaurex, A. Hessler-

Wyser, and S. De Wolf, J. Appl. Phys. **115**, 163703 (2014).

[108] C.-S. Yang, L. L. Smith, C. B. Arthur, and G. N. Parsons, Journal of Vacuum Science & Technology B **18**, 683 (2000).

[109] Z. Czigány, G. Radnóczi, K. Järrendahl, and J. E. Sundgren, J. Mater. Res. **12**, 2255 (1997).

[110] A. Csik, D. L. Beke, G. A. Langer, Z. Erdélyi, L. Daroczi, K. Kapta, and M. Kis-Varga, Vacuum **61**, 297 (2001).

[111] J. Nyéki, C. Girardeaux, Z. Erdélyi, G. A. Langer, and G. Erdélyi, Surf. Sci. **495**, 195 (2001).

[112] M. A. Noah, D. Flötotto, Z. M. Wang, and E. J. Mittemeijer, Surf. Interface Anal. **46**, 1057 (2014).

[113] J. Ayache, L. Beaunier, J. Boumendil, G. Ehret, and D. Laub, *Sample Preparation Handbook for Transmission Electron Microscopy: Methodology* (Springer Berlin / Heidelberg, 2010).

[114] *MultiPak, Physical Electronics, Inc.* (2014).

[115] S. Hofmann, *Auger- and X-ray Photoelectron Spectroscopy in Materials Science* (Springer Berlin / Heidelberg, 2013) p. 279.

[116] Z. Erdélyi and D. L. Beke, J. Mater. Sci. **46**, 6465 (2011).

[117] G. B. Stephenson, Acta Mater. **36**, 2663 (1988).

[118] F. Spaepen, J. Magn. Magn. Mater. **156**, 407 (1996).

[119] R. W. Olesinski and G. J. Abbaschian, Bulletin of Alloy Phase Diagrams **5**, 180 (1984).

[120] C. Tzoumanekas and P. C. Kelires, Phys. Rev. B **60**, 14205 (1999).

[121] C. Tzoumanekas and P. C. Kelires, Phys. Rev. B **66**, 195209 (2002).

[122] V. T. Bublik, S. S. Gorelik, A. A. Zaitsev, and A. Y. Polyakov, phys. status solidi (b) **66**, 427 (1974).

[123] A. Qteish and R. Resta, Phys. Rev. B **37**, 6983 (1988).

[124] S. Gironcoli, P. Giannozzi, and S. Baroni, Phys. Rev. Lett. **66**, 2116 (1991).

[125] V. S. Sudavtsova and V. G. Kudin, Inorg. Mater. **37**, 319 (2001).

[126] S. Amore, D. Giuranno, R. Novakovic, E. Ricci, R. Nowak, and N. Sobczak, Calphad **44**, 95 (2014).

[127] H. Bracht, E. E. Haller, and R. Clark-Phelps, Phys. Rev. Lett. **81**, 393 (1998).

[128] E. Hüger, U. Tietze, D. Lott, H. Bracht, D. Bougeard, E. E. Haller,

and H. Schmidt, Appl. Phys. Lett. **93**, 162104 (2008).

[129] H. H. Silvestri, H. Bracht, J. Lundsgaard Hansen, A. Nylandsted Larsen, and E. E. Haller, Semicond. Sci. Technol. **21**, 758 (2006).

[130] S. Roorda, W. C. Sinke, J. M. Poate, D. C. Jacobson, S. Dierker, B. S. Dennis, D. J. Eaglesham, F. Spaepen, and P. Fouss, Phys. Rev. B **44**, 3702 (1991).

[131] A. Witvrouw and F. Spaepen, J. Appl. Phys. **74**, 7154 (1993).

[132] P. D. Persans and A. F. Ruppert, Mater. Res. Soc. Symp. Proc. **57**, 329 (1987).

[133] F. J. Demond, S. Kalbitzer, H. Mannsperger, and Damjantschitsch, Phys. Lett. A **93**, 503 (1983).

[134] J. M. Fairfield and B. J. Masters, J. Appl. Phys. **38**, 3148 (1967).

[135] R. N. Ghoshtagore, Phys. Rev. Lett. **16**, 890 (1966).

[136] G. Hettich, H. Mehrer, and K. Maier, Inst. Phys. Conf. Ser. **46**, 500 (1979).

[137] J. Hirvonen and A. Anttila, Appl. Phys. Lett. **35**, 703 (1979).

[138] L. Kalinowski and R. Seguin, Appl. Phys. Lett. **36**, 171 (1980).

[139] H. J. Mayer, H. Mehrer, and K. Maier, Inst. Phys. Conf. Ser. **31**, 186 (1977).

[140] R. F. Peart, phys. status solidi **15**, K119 (1966).

[141] I. Santos, M. L. A., and L. Pelaz, Phys. Rev. B **83**, 153201 (2011).

[142] Z. G. Zhu and C. S. Liu, Phys. Rev. B **61**, 9322 (2000).

[143] G. L. McVay and A. R. DuCharme, Inst. Phys. Conf. Ser. **23**, 91 (1975).

[144] A. Strohm, T. Voss, W. Frank, J. Räisänen, and M. Dietrich, Physica B **308-310**, 542 (2001).

[145] N. Zangenberg, J. Lundsgaard Hansen, J. Fage-Pedersen, and A. Nylandsted Larsen, Phys. Rev. Lett. **87**, 125901 (2001).

[146] F. Valiquette and N. Mousseau, Phys. Rev. B **68**, 125209 (2003).

[147] L. Pizzagalli, J. Godet, J. Guénolé, S. Brochard, E. Holmstrom, K. Nordlund, and T. Albaret, J. Phys.: Condens. Matter **25**, 055801 (2013).

[148] S. Dannefaer, P. Mascher, and D. Kerr, Phys. Rev. Lett. **56**, 2195 (1986).

[149] H. M. Pinto, J. Coutinho, V. J. B. Torres, S. Öberg, and P. R. Briddon,

Mater. Sci. Semicond. Process. **9**, 498 (2006).

[150] H. Schmidt, W. Gruber, T. Gutberlet, M. Ay, J. Stahn, U. Geckle, and M. Bruns, J. Appl. Phys. **102**, 043516 (2007).

[151] G. D. Watkins, Mater. Sci. Semicond. Process. **3**, 227 (2000).

[152] E. J. Mittemeijer, *Fundamentals of Materials Science* (Springer Berlin / Heidelberg, 2010,) pp. 438–439.

[153] G. T. Barkema and N. Mousseau, Phys. Rev. Lett. **81**, 1865 (1998).

[154] N. Mousseau and G. T. Barkema, Phys. Rev. B **61**, 1898 (2000).

[155] B. Cordero, V. Gómez, A. E. Platero-Prats, M. Revés, J. Echeverría, E. Cremades, F. Barragán, and S. Alvarez, Dalton Trans. **21**, 2832 (2008).

[156] A. Ciccioli, G. Gigli, G. Meloni, and E. Testani, J. Chem. Phys. **127**, 054303 (2007).

[157] F. Aldinger, Acta Metall. **22**, 923 (1974).

[158] H. J. Fan, U. Gösele, and M. Zacharias, Small **3**, 1660 (2007).

[159] S. Chakravarty, M. Jiang, U. Tietze, D. Lott, T. Geue, J. Stahn, and H. Schmidt, Acta Mater. **59**, 5568 (2011).

[160] W. P. Gillin, D. J. Dunstan, K. P. Homewood, L. K. Howard, and S. B. J., J. Appl. Phys. **73**, 3782 (1993).

[161] O. M. Khreis, W. P. Gillin, and K. P. Homewood, Phys. Rev. B **55**, 15813 (1997).

[162] F. D. Fischer and J. Svoboda, Acta Mater. **58**, 2698 (2010).

[163] J. Svoboda and F. D. Fischer, Acta Mater. **59**, 1212 (2011).

[164] H. Wan, Y. Shen, X. Jin, Y. Chen, and J. Sun, Acta Mater. **60**, 2528 (2012).

[165] H. Wan, Y. Shen, X. Jin, Y. Chen, and J. Sun, Acta Mater. **60**, 2539 (2012).

[166] H. Okamoto and T. B. Massalski, Bull. Alloy Phase Diagrams **4**, 30 (1983).

[167] W. C. Mallard, A. B. Gardner, R. F. Bass, and L. M. Slifkin, Phys. Rev. B **129**, 617 (1963).

[168] M. J. Dallwitz, Acta Metall. **20**, 1229 (1972).

[169] K. Meinel, M. Klaua, C. Ammer, and H. Bethege, phys. status solidi (a) **106**, 493 (1988).

[170] Y. Liu, L. Zhang, and Y. Ge, J. Phase Equilib. Diffus. **29**, 405 (2008).

[171] C. Herzig and D. Wolter, Z. Metallkd. **65**, 273 (1974).

[172] S. M. Klotsman, N. K. Arkhipova, A. N. Timofeyev, and L. S. Trakhtenberg, Fiz. metal. metalloved. **20**, 390 (1965).

[173] F. E. Jaumot and A. Sawatzky, J. Appl. Phys. **27**, 1186 (1956).

[174] H. W. Mead and C. E. Birchenall, Trans. AIME **209**, 874 (1957).

[175] E. J. Mittemeijer and U. Welzel, eds., *Modern Diffraction Methods* (Wiley-VCH. Weinheim, 2012, Chapter 12).

[176] P. J. Schultz and K. G. Lynn, Rev. Mod. Phys. **60**, 701 (1988).

[177] M. J. Puska and R. M. Nieminen, Rev. Mod. Phys. **66**, 841 (1994).

[178] C. Hugenschmidt, B. Lówe, J. Mayer, C. Piochacz, P. Pikart, R. Repper, M. Stadlbauer, and K. Schreckenbach, Nucl. Instrum. Meth. A **593**, 616 (2008).

[179] C. Hugenschmidt, H. Ceeh, T. Gigl, F. Lippert, C. Piochacz, M. Reiner, K. Schreckenbach, S. Vohburger, J. Weber, and S. Zimnik, J. Phys. Conf. Ser. **505**, 012029 (2014).

[180] M. Reiner, P. Pikart, and C. Hugenschmidt, J. Phys. Conf. Ser. **443**, 012071 (2013).

[181] A. van Veen, H. Schut, J. de Vries, R. A. Hakvoort, and M. R. Ijpma, AIP Conf. Proc. **218**, 171 (1991).

[182] A. van Veen, H. Schut, M. Clement, J. M. M. de Nijs, A. Kruseman, and M. R. IJpma, Appl. Surf. Sci. **85**, 216 (1995).

[183] B. Okolo, P. Lamparter, U. Welzel, T. Wagner, and E. J. Mittemeijer, Thin Solid Films **474**, 50 (2005).

[184] F. J. Palomares, M. Serrano, A. Ruiz, F. Soria, K. Horn, and M. Alonso, Surf. Sci. **513**, 283 (2002).

[185] I. V. Belova and G. E. Murch, Philos. Mag. A **80**, 1469 (2000).

[186] L. K. Moleko, A. R. Allnatt, and E. L. Allnatt, Philos. Mag. A **59**, 141 (1989).

[187] I. V. Belova, A. R. Allnatt, and G. E. Murch, Philos. Mag. **87**, 4169 (2007).

[188] S. Hassam, M. Gambino, M. Gaune-Escard, J. Bros, and J. Ågren, Metall. Trans. A **19A**, 409 (1988).

[189] C. T. Tomizuka and E. Sonder, Phys. Rev. **103**, 1182 (1956).

[190] N. Q. Lam, S. J. Rothman, H. Mehrer, and L. J. Nowicki, phys. stat. sol. **57**, 225 (1973).

[191] J. Bihr, H. Mehrer, and K. Maier, phys. stat. sol. **50**, 171 (1978).

[192] S. J. Rothman, N. L. Peterson, and J. T. Robinson, phys. stat. sol. **39**, 635 (1970).

[193] J. G. E. M. Backus, H. Bakker, and H. Mehrer, phys. stat. sol. **65**, 151 (1974).

[194] G. Rein and H. Mehrer, Philos. Mag. **45**, 467 (1982).

[195] N. H. Nachtrieb, J. Petit, and J. Wehrenberg, J. Chem. Phys. **26**, 106 (1957).

[196] S. M. Makin, A. H. Rowe, and A. D. LeClaire, Proc. Phys. Soc. B **70**, 545 (1957).

[197] B. Okkerse, Phys. Rev. **103**, 1246 (1956).

[198] W. Rupp, U. Ermert, and R. Sizmann, phys. stat. sol. **33**, 509 (1969).

[199] D. Duhl, K.-I. Hirano, and M. Cohen, Acta Metall. **11**, 1 (1963).

[200] C. Herzig, H. Eckseler, W. Bussmann, and D. Cardis, J. Nucl. Mater. **69/70**, 61 (1978).

[201] A. Seeger and H. Mehrer, phys. stat. sol. **29**, 231 (1968).

[202] H. Mehrer, *Diffusion in Solids: Fundamentals, Methods, Materials, Diffusion-Controlled Processes* (Springer Berlin / Heidelberg, 2007) pp. 303–306.

[203] P. Ehrhart, *Atomic Defects in Metals*, edited by H. Ullmaier (Springer Berlin / Heidelberg, 1991).

[204] M. Doyama and J. S. Koehler, Phys. Rev. **127**, 21 (1962).

[205] G. Neumann and V. Tölle, Philos. Mag. **54**, 619 (1986).

[206] C. V. Thompson and R. Carel, J. Mech. Phys. Solids **44**, 657 (1996).

[207] D. Flötotto, Z. M. Wang, L. P. H. Jeurgens, and E. J. Mittemeijer, J. Appl. Phys. **118**, 055305 (2015).

[208] B. Predel, in *Landolt-Börnstein - Group IV Physical Chemistry*, Vol. 5A, edited by O. Madelung (Springer Berlin / Heidelberg, 1991).

[209] J. Huang, S. Vongehr, S. Tang, H. Lu, and X. Meng, J. Phys. Chem. C **114**, 15005 (2010).

[210] J. Shu, B. P. A. Grandjean, and S. Kaliaguine, Appl. Catal., A **119**, 305 (1994).

[211] H. Amandusson, L.-G. Ekedahl, and H. Dannetun, J. Membr. Sci. **193**, 35 (2001).

[212] J. Shu, A. Adnot, B. P. A. Grandjean, and S. Kaliaguine, Thin Solid Films **286**, 72 (1996).

[213] G. Zeng, A. Goldbach, L. Shi, and H. Xu, Int. J. Hydrogen Energy **37**, 6012 (2012).

[214] M. E. Ayturk, E. A. Payzant, S. A. Speakman, and Y. H. Ma, J. Membr. Sci. **316**, 97 (2008).

[215] N. L. Peterson, Phys. Rev. **132**, 2471 (1963).

[216] J. Chen, B. Wiley, J. McLellan, Y. Xiong, Z.-Y. Li, and Y. Xia, Nano Lett. **5**, 2058 (2005).

[217] Y. Sun, Z. Tao, J. Chen, T. Herricks, and Y. Xia, J. Am. Ceram. Soc. **126**, 5940 (2004).

[218] M. A. Noah, D. Flötotto, Z. M. Wang, M. Reiner, C. Hugenschmidt, and E. J. Mittemeijer, Acta Mater. **107**, 133 (2016).

[219] J. Ayache, L. Beaunier, J. Boumendil, G. Ehret, and D. Laub, *Sample Preparation Handbook for Transmission Electron Microscopy: Methodology* (Springer Berlin / Heidelberg, 2010, Chapter 6).

[220] U. Welzel, J. Ligot, P. Lamparter, A. C. Vermeulen, and E. J. Mittemeijer, J. Appl. Crystallogr. **38**, 1 (2005).

[221] Y. A. Touloukian, *Thermal Expansion* (IFI/Plenum, 1977).

[222] A. G. Every and A. K. McCurdy, *Second and Higher Order Elastic Constants*, edited by D. F. Nelson, Landolt-Börnstein - Group III Condensed Matter volume 29a (Springer Berlin / Heidelberg, 1992).

[223] R. Delhez and E. J. Mittemeijer, J. Appl. Cryst. **8**, 609 (1975).

[224] D. Cherns and M. J. Stowell, Thin Solid Films **29**, 107 (1975).

[225] J. W. Matthews, Thin Solid Films **25**, 199 (1975).

[226] A. M. Beers and E. J. Mittemeijer, Thin Solid Films **48**, 367 (1978).

[227] J. S. Kirkaldy and G. Savva, Acta Mater. **45**, 3115 (1997).

[228] M. Hoffmann, A. Marmodoro, E. Nurmi, K. Kokko, L. Vitos, A. Ernst, and W. Hegert, Phys. Rev. B **86**, 094106 (2012).

[229] J. S. Kirkaldy and D. J. Young, *"Diffusion in the Condensed State"* (The Institute of Metals, London, 1987).

[230] R. L. Rowland and N. H. Nachtrieb, J. Phys. Chem. **67**, 2817 (1963).

[231] D. Feng and P. Taskinen, J. Mater. Sci. **49**, 5790 (2014).

[232] J. P. Chan and R. Hultgren, J. Chem. Thermodynamics. **1**, 45 (1969).

[233] N. L. Peterson, Phys. Rev. **136**, A568 (1964).

[234] I. B. Borovski, I. D. Marchuko, and Y. E. Ugaste, Phys. Met. Metallogr. **22**, 43 (1966).

[235] D. B. Butrymowicz, J. R. Manning, and M. E. Read, J. Phys. Chem. Ref. Data **2**, 643 (1973).

[236] V. M. Kosevich, A. N. Gladkikh, M. V. Karpovskyi, and V. N. Klimenko, Interface Science **2**, 247 (1994).

[237] V. M. Kosevich, A. N. Gladkikh, M. V. Karpovskyi, and V. N. Klimenko, Interface Science **2**, 261 (1994).

[238] V. M. Kosevich, A. N. Gladkikh, M. V. Karpovskyi, and V. N. Klimenko, Interface Science **2**, 271 (1994).

[239] V. M. Kosevich, V. N. Klimenko, A. N. Gladkikh, and M. V. Karpovskyi, Interface Science **3**, 151 (1995).

[240] Y. Kuru, M. Wohlschlögel, U. Welzel, and E. J. Mittemeijer, Appl. Phys. Lett. **95**, 163112 (2009).

[241] R. Delhez and E. J. Mittemeijer, J. Appl. Phys. **49**, 4770 (1978).

[242] B. Bolle, A. Tidu, and J. J. Heizmann, J. Appl. Cryst. **32**, 27 (1999).

[243] T. Gressmann, A. Leineweber, and E. J. Mittemeijer, Philos. Mag. **88**, 145 (2008).

[244] A. G. Every and A. K. McCurdy, in *Landolt-Börnstein - Group III Condensed Matter*, Vol. 29A, edited by D. F. Nelson (Springer Berlin / Heidelberg, 1992).

[245] M. D. Thouless, K. P. Rodbell, and C. Carbral, J. Vac. Sci. Technol. A **14**, 2454 (1996).

[246] R.-M. Keller, S. P. Baker, and E. Arzt, J. Mater. Res. **13**, 1307 (1998).

[247] R.-M. Keller, S. P. Baker, and E. Arzt, Acta Mater. **47**, 415 (1999).

[248] S. P. Baker, A. Kretschmann, and E. Arzt, Acta Mater. **49**, 2145 (2001).

[249] G. Dehm, T. Wagner, T. J. Balk, and E. Arzt, J. Mater. Sci. Technol. **18**, 113 (2002).

[250] H. J. Frost and M. F. Ashby, *Deformation-Mechanisms Maps* (Pergamon Press, Oxford, Chapter 1, 1982).

[251] J. Chakraborty, U. Welzel, and E.J. Mittemeijer, unpublished work, see J. Chakraborty, *"Diffusion in Stressed Thin Films"*, Ph.D. thesis, University of Stuttgart (2005, pp. 14-23).

[252] M. J. Verstraete, J. Dumont, R. Sporken, R. L. Johnson, F. Wiame, K. Temst, J. Swerts, F. Mirabela, G. Jacques, and X. Gonze, Phys. Rev. B **70**, 205427 (2004).

List of Publications

1. Martin A. Noah, David Flötotto, Zumin Wang, and Eric J. Mittemeijer, *Single and multiple profile fitting of AES and XPS intensity-depth profiles for analysis of interdiffusion in thin films*, Surf. Interface Anal. **46**, 1057 (2014). (Chapter 2 of this thesis)

2. Martin A. Noah, David Flötotto, Zumin Wang, and Eric J. Mittemeijer, *Con-centration-dependent self-diffusion coefficients in amorphous* $Si_{1-x}Ge_x$ *solid solutions; an interdiffusion study*, J. Appl. Phys. **117**, 165306 (2015). (Chapter 3 of this thesis)

3. Martin A. Noah, David Flötotto, Zumin Wang, Markus Reiner, Christoph Hugenschmidt and Eric J. Mittemeijer, *Interdiffusion in epitaxial, single-crystalline Au/Ag thin films studied by Auger electron spectroscopy sputter-depth profiling and positron annihilation*, Acta Mater. **107**, 133 (2016). (Chapter 4 of this thesis)

4. Martin A. Noah, David Flötotto, Zumin Wang, and Eric J. Mittemeijer, *Interdiffusion and stress development in single-crystalline Pd/Ag thin films*, J. Appl. Phys. **119**, 145308 (2016). (Chapter 5 of this thesis)

Danksagung

Die vorliegende Arbeit wurde am Max-Planck Institut für Intelligente Systeme (ehemals Max-Planck Institut für Metallforschung), Stuttgart, und dem Institut für Materialwissenschaft der Universität Stuttgart angefertigt. An dieser Stelle möchte ich allen danken, die zum Gelingen der Arbeit beigetragen haben.

An erster Stelle möchte ich meinem Doktorvater, Herrn Prof. Dr. Ir. E.J. Mittemeijer, für die Aufnahme in seiner Abteilung und die Überlassung des interessanten Forschungsthemas danken. Das entgegengebrachte Vertrauen sowie die große Freiheit meine Arbeit selbst gestalten zu können war sehr motivierend. Die zahlreichen wissenschaftlichen Diskussionen regten stets zum Nachdenken an und trugen maßgeblich zum Gelingen der Arbeit bei. Für diese außergewöhnliche Unterstützung und Förderung möchte ich mich herzlich bedanken.

Herrn Prof. Dr. J. Bill danke ich für die freundliche Übernahme des Mitberichts und Herrn Prof. Dr. T. Schleid für die freundliche Bereitschaft den Prüfungsvorsitz zu übernehmen.

Meinen täglichen Betreuern Dr. David Flötotto und Prof. Dr. Zumin Wang möchte ich für die kontinuierliche Hilfestellung, Motivation und Diskussionsbereitschaft danken. Ihr großes Interesse an der Arbeit half bei der Übwerwindung vieler Schwierigkeiten.

Herrn PD Dr. C. Hugenschmidt, Herrn Dipl.-Phys. M. Reiner und Herrn Dipl.-Phys T. Gigl von der Technischen Universität München möchte ich für die Unterstützung bei den Positron-Annihilationsmessungen danken.

Diese Arbeit wäre ohne die Hilfe der Mitarbeiter der Max-Planck Institute in Stuttgart nicht möglich gewesen. Ihre angagierte Mitarbeit trug maßgeblich zu einem angenehmen und produktiven Arbeitsklima bei. Besonders möchte ich mich bei Herrn Prof. Dr. S. Hofmann, Herrn Dipl.-Ing. B. Siegle, Herrn Dipl.-Ing. P. Schützendübe, Frau M. Wieland, Herrn G. Hörner, Herrn Dipl.-Ing. F. Thiele, Herrn R. Völker, Herrn Dipl.-Ing. G. Maier, Herrn Dipl.-Ing. P. Kopold, Herrn W.-D. Lang und Herrn Dr. E. Bischoff bedanken.

Meinen Kollegen und Freunden, Katharina und Bastian, möchte ich ganz besonders für ihre große Hilfsbereitschaft und Unterstützung danken.

Zu guter Letzt möchte ich mich bei meiner Familie für ihren Rückhalt bedanken.

Erklärung über die Eigenständigkeit der Dissertation

Ich versichere, dass ich die vorliegende Arbeit mit dem Titel „Interrelationship of interdiffusion and microstructure in thin film systems“ selbstständig vefasst und keine anderen als die angegebenen Quellen und Hilfsmittel benutzt habe; aus fremden Quellen entnommene Passagen und Gedanken sind als solche kenntlich gemacht.

Declaration of Authorship

I hereby certify that the dissertation entitled “Interrelationship of interdiffusion and microstructure in thin film systems” is entirely my own work except where otherwise indicated. Passages and ideas from other sources have been clearly indicated.

Stuttgart, den 31. März 2016

____

(Martin A. Noah)